Computational design of Co- and Fe-based CO_2 to jet fuel catalysts

Catarina Regra da Silva

Thesis to obtain the Master of Science Degree in

Chemical Engineering

Supervisors: Prof. Mark Saeys

Prof. Carlos Manuel Faria de Barros Henriques

Coach: Konstantijn Rommens

Examination Committee

Chairperson: Prof. Francisco Manuel Da Silva Lemos

Supervisor: Prof. Mark Saeys

Member of the Committee: Prof. Alexander Kirillov

25 of November 2022

Acknowledgments

I would like to express my deep gratitude to my supervisors Prof. Mark Saeys and Prof. Carlos Henriques, for sharing knowledge and for allowing me to work with them. My special thanks to Konstantijn Rommens for constantly helping me during my thesis at Ghent University. Also, the assistance provided by Sara Santos was greatly appreciated. Thank you very much for the constant challenge given and for giving me the ability to set my goals high.

I also would like to thank my colleagues from my home university who helped me a lot in the transition to living in another country. I would like to thank my family for their support. I am grateful for the support and understanding of my friends in my home town and university. My special thanks to Miguel Reis for always being present and for his patience throughout this journey.

All of you played a crucial role in my success. I share this success with you all. I am forever grateful.

Resumo

A síntese Fischer-Tropsch é normalmente utilizada para a produção de hidrocarbonetos a partir de misturas CO/H_2 (syngas), sendo igualmente possível utilizar misturas CO_2/H_2. Neste trabalho, catalisadores à base de cobalto e ferro são estudados, através de cálculos DFT. Para o catalisador de cobalto foi desenvolvido um modelo microcinético, tendo em vista o estudo do mecanismo reaccional FT.

Na superfície Co(111), a adsorção de CO foi mais estável no topo com uma energia de adsorpção igual a -135kJ/mol. A ativação de CO_2 com OH* e com H* foi investigada igualmente na superfície Co(111). As reacções de hidrogenação de HCOO* e dissociação de CO_2, HCOO e COOH foram também consideradas. As respectivas energias de reacção e de activação foram calculadas tendo sido construídos os perfis de energia.

Um modelo microcinético foi desenvolvido e aplicado para dois cenários diferentes (single-site e dual-site) e para dois tipos diferentes de alimentação, H_2/CO e H_2/CO_2, para 1 e 20 bar. Verificou-se que, em geral, o metano foi o produto obtido com maior seletividade.

Foram analisadas diversas estruturas de carboneto de ferro: χ-Fe_5C_2, ϵ-Fe_3C, η-Fe_2C e θ-Fe_3C. As energias coesiva e de formação foram calculadas e a estrutura de carboneto de ferro que apresenta as menores energias é η-Fe_2C.

As superfícies foram analisadas para todas as estruturas e o impacto da razão Fe/C na estabilidade da superfície foi investigado. As energias de adsorção foram calculadas na superfície χ-Fe_5C_2(510) onde a energia de adsorção de CO é igual a -1.97eV no centro ativo [Fe 3-fold].

Palavras-chave: Hidrogenação de CO_2, Combustível de aviação, Cobalto, Carbonetos de Ferro, Cálculos DFT, Modelação Microcinética

Abstract

The Fischer-Tropsch Synthesis is used to form hydrocarbons with a syngas mixture (CO and H_2), but a CO_2 and H_2 feed can be used as well. In this work, Co- and Fe-based catalysts are studied with DFT calculations, and for Co-based catalysts, a microkinetic model is used to study the FT mechanism.

Cobalt bulk structures were analysed, FCC and HCP. On the Co(111) surface, CO adsorption was most stable at the top site with a value of -135kJ/mol. Furthermore, CO_2 activation with OH* and with H* was investigated on Co(111). HCOO* hydrogenation and dissociation reactions of CO_2, HCOO and COOH were also considered. Activation barriers and reaction energies were calculated for these reactions, and energy profiles were constructed. The path of CO_2 hydrogenation with OH* to form COOH* and subsequent dissociation to CO* and OH* is the least energy required. A dual-site microkinetic model was used for two scenarios (single-site and dual-site) and two different feed types, i.e., H_2/CO and H_2/CO_2, for 1bar and 20bar. Overall, methane was the product with the highest selectivity.

The iron carbide bulk structures analysed were χ-Fe_5C_2, ϵ-Fe_3C, η-Fe_2C and θ-Fe_3C. Cohesive and formation energies were calculated, and the iron carbide with the lowest energies is η-Fe_2C. Surfaces were analysed for all bulk structures, and the impact of the Fe/C ratio on surface stability was investigated via the carbon chemical potential. Adsorption energies were calculated on the χ-Fe_5C_2(510) surface where CO adsorption energy is -1.97eV on Fe 3-fold site.

Keywords: CO_2 Hydrogenation, Jet Fuel, Cobalt, Iron Carbides, DFT calculations, Microkinetic Modelling

Contents

Acknowledgments . . . iii

Resumo . . . v

Abstract . . . vii

List of Tables . . . xi

List of Figures . . . xiii

Nomenclature . . . xvii

Glossary . . . xxi

1 Introduction 1

1.1 Thesis Outline . . . 2

2 State of the art 3

2.1 Jet Fuel . . . 3

2.2 Bio-Processes . . . 5

2.3 CO_2 Hydrogenation . . . 7

2.4 Catalysts for CO_2 conversion . . . 10

2.5 Commercial SAFs . . . 19

3 Methods 21

3.1 Density Functional Theory . . . 21

3.2 Catalyst Modelling . . . 23

3.2.1 Cobalt . . . 23

3.2.2 Iron Carbides . . . 23

3.3 VASP simulations . . . 24

3.3.1 Convergence Tests . . . 25

3.3.2 Geometry Optimisation . . . 26

3.3.3 Vibrational Frequencies . . . 27

3.3.4 Transition State . . . 28

3.3.5 Result Analysis methods . . . 30

3.4 Microkinetic Modelling . . . 34

3.4.1 Transition state theory . . . 35

3.4.2 Chemkin Simulations . . . 35

3.4.3 Result Analysis . . . 36

4 Cobalt-based Catalyst 37

4.1 Bulk Structures . . . 37

4.2 Surface Co(111) . . . 38

4.2.1 Adsorption of Molecules on Co(111) . . . 39

4.2.2 Transition States . . . 42

4.3 Microkinetic Modelling . . . 44

4.3.1 CO feed . . . 44

4.3.2 CO_2 feed . . . 46

5 Iron-based Catalyst 48

5.1 Bulk Structures . . . 48

5.2 Surfaces . . . 51

5.2.1 ϵ-Fe_3C . . . 52

5.2.2 η-Fe_2C . . . 54

5.2.3 χ-Fe_5C_2 . . . 55

5.2.4 θ-Fe_3C . . . 57

5.3 SCAN-rVV10 Performance . . . 59

5.4 Adsorption of molecules on χ-Fe_5C_2(510) . . . 59

6 Conclusions 63

6.1 Future Work . . . 64

Bibliography 65

A Methods 73

B Results 77

List of Tables

2.1 Chemical composition for various Jet-A/JP8 fuels.[9] 4

2.2 Catalysts performance in CO_2 hydrogenation to hydrocarbons. 16

3.1 Parameters used for cobalt structures VASP calculations. 26

3.2 Parameters and characteristics of iron carbide slab surfaces for each bulk structure. 27

4.1 Optimised bulk structures with VdW-DF functional and Murnaghan equation-of-state results. 37

4.2 Average formation energy (J/m^2) of the bottom (unrelaxed) and top layers (relaxed) for each slab. 39

4.3 Adsorption energy of CO on top site for different slabs. 39

4.4 Adsorption energies (E_{ads} values including ZPE in parentheses) of CO adsorption on top, fcc, hcp and bridge sites of Co(111). 40

4.5 Adsorption Energies of molecules adsorbed on Co(111) with a coverage of 1/9 ML calculated with VdW-DF functional. 41

4.6 Activation energies from DFT (VdW-DF), Gibbs free energy barriers and Gibbs free energies of reaction for studied reactions and their transition states. 42

4.7 Results from the low coverage model in Chemkin with a CO feed at the specified pressure. 44

4.8 Results from the low coverage model in Chemkin with a CO_2 feed at the specified pressure. 46

5.1 Settings of input files for VASP calculations of geometry optimisation and amount of atoms in each unit cell. 48

5.2 Iron carbide bulk structures lattice constants, optimal volume, bulk modulus and cohesive energy from this work, DFT reference and experimental values. 49

5.3 Formation energies for each iron carbide bulk structure with two different chemical potentials of carbon. PBE functional was used for calculations and also for Liu et al. values.[79] 50

5.4 First SCH loop real time for 4 structure simulations with SCAN-rVV10, VdW-DF and PBE functionals. 59

5.5 Calculated adsorption energies (E_{ads}, eV) of molecules on $\chi(510)_{0.0}$ surface with a coverage of 1/40 ML. Calculated with PBE functional. 60

5.6 Adsorption energies and structural parameters of CO on Fe 3-fold site, of this work and Pham et al.[81]. 61

A.1 Electronic energies of some species in gas phase and calculated from a dissociation. Values obtained with PBE functional. 75
A.2 Electronic energies calculated from VASP of Fe and C atom in gas phase, and all bulk structures studied. 76
A.3 Carbon chemical potential values for several CO partial pressures. At 0.1 MPa total pressure and 523 K. 76

B.1 Gas phase molecules $E0$ values from VASP calculations with VdW-DF and PBE functionals. 77
B.2 Cohesive energies calculated for all iron carbides studied with PBE, VdW-DF and SCAN-rVV10 functionals. 81
B.3 Formation energies (μ_C=-6.65 eV) calculated for all iron carbides studied with PBE, VdW-DF and SCAN-rVV10 functionals. 81
B.4 Surface energies of $\epsilon - Fe_3C$ surfaces for PBE, VdW-DF and SCAN-rVV10 functionals and atoms ratio Fe/C. 81
B.5 Surface energies of $\eta - Fe_2C$ surfaces for PBE, VdW-DF and SCAN-rVV10 functionals and atoms ratio Fe/C. 82
B.6 Surface energies of $\chi - Fe_5C_2$ surfaces for PBE, VdW-DF and SCAN-rVV10 functionals and atoms ratio Fe/C. 82
B.7 Surface energies of $\theta - Fe_3C$ symmetric and stoichiometric surfaces for PBE, VdW-DF and SCAN-rVV10 functionals and atoms ratio Fe/C. 82

List of Figures

1.1 Jet fuel production in a circular economy point of view. Adapted from [6]. 2

2.1 Conversion pathways to bio-jet fuel production. Adapted from [15]. 5
2.2 Pathways of CO_2 conversion to hydrocarbons. Adapted from [20], [21] and [22]. 7
2.3 Auto-catalytic dual cycle mechanism (alkene and arene cycles) representation. Image of [14]. 9
2.4 Representation of a CO_2 FT reaction mechanism over a catalyst. Image of [26]. 9
2.5 ASF Distribution weight fraction (w_i) vs chain growth probability. The graph was constructed using $w_i = \alpha^{i-1}(1-\alpha)^2 * i$, being i the number of carbons. Formula and principle of construction of [30], [29] and [31]. 10
2.6 CO_2 conversion and CH_4 yield with temperatures ranging from 150° C to 450° C during CO_2 methanation on supported Ni catalysts. Image from [41]. 12
2.7 Diagram showing all potential CO_2 activation reaction pathways over Ni in the colours pink (carboxylate pathway), blue (carbide pathway), and yellow (formate pathway). Grey dots represent all intermediates. Other lines show possible connections between the main paths. Adapted from [42]. 13
2.8 Product selectivity of Fe_3O_4-based catalysts. Image from [47]. 15
2.9 Hydrogenation of CO_2 to gasoline range hydrocarbons: reaction scheme. Adapted from [37]. 17
2.10 Hydrocarbon product distribution on c) Na-Fe_3O_4 and d) Na-Fe_3O_4/HZSM-5. Image from [37]. 17
2.11 Hydrocarbon product distribution on b) $ZnFeO_x$-4.25Na and c) $ZnFeO_x$-4.25Na/S-HZSM-5. Image from [49]. 18

3.1 Cobalt structures studied: (a), (b) and (c) bulk structures and (d) surface (111) from FCC bulk structure. 23
3.2 Unit cell representation with surface notation. Image from [67]. 24
3.3 Different slab surfaces: (a) $\chi(010)_{0.25}$ symmetric and stoichiometric, $\chi(100)_{0.287}$: (b) symmetric and non-stoichiometric, and (c) asymmetric and stoichiometric. 24
3.4 Test convergence of FCC cubic cobalt bulk structure. 25
3.5 Vibrational modes of a gas phase molecule. Adapted from [34]. 28
3.6 Vibrational modes of an adsorbed molecule on a surface. Adapted from [34]. 28
3.7 Representation of the differences of NEB and cNEB methods. Image from [73]. 29

3.8 Co(111) χ-Fe_5C_2(510) and active sites used for molecules adsorption. 30
3.9 Carbon chemical potential relation with CO partial pressure, at 523K and 0.1 MPa. . . . 34
3.10 Elementary reaction step diagram with the reaction energy and activation energy. Image from [82]. 35

4.1 FCC bulk structures optimised with Murnaghan equation-of-state 38
4.2 HCP-O bulk structure optimised with Murnaghan equation-of-state. 38
4.3 Representation of slab structures of Cobalt with (a) 3, (b) 4 and (c) 5 layers. 39
4.4 VESTA representation of adsorbed CO on Co(111) on several active sites. 40
4.5 VESTA representation of adsorbed HCOH and H_2CO on Co(111) from this work (a and c) and Gunasooriya[34] (b and d). 41
4.6 ΔH energy profile of the reactions studied which form a pathway for CO_2 hydrogenation on Co(111). 43
4.7 ΔG energy profile of the reactions studied which form a pathway for CO_2 hydrogenation on Co(111). 44
4.8 CO feed results on surface coverages (S stands for terrace site) of CO, H, rest of the molecules and empty terrace site for scenario **A**, and scenario **B** at 1 bar and 20 bar. . . . 45
4.9 CO_2 feed results on surface coverages (terrace site) of CO, H, rest of the molecules and empty terrace site for scenario **A**, and scenario **B** at 1 bar and 20 bar. 46

5.1 Iron carbides bulk structures studied. The yellow and brown atoms represent the Fe and C atoms, respectively. 49
5.2 Formation energies (μ_C =-6.65 eV) calculated for all iron carbides studied with PBE, VdW-DF and SCAN-rVV10 functionals 50
5.3 Iron carbides bulk structures optimised with Murnaghan equation-of-state. 51
5.4 Top view of slab surfaces of constructed ϵ-Fe_3C. 52
5.5 Surface energy of ϵ-Fe_3C asymmetric surfaces for PBE, VdW-DF and SCAN-rVV10 functionals and reference values. (*) Asymmetric and stoichiometric surfaces.[92] 52
5.6 ϵ-Fe carbides bulk structures with two additional non-symmetry conforming carbon layers at c = 0 and c = 0.25 (ϵ-Fe_2-0.25C), and at c = 0 and c = 0.75 (ϵ-Fe_2-0.75C). Image from [92]. 53
5.7 Surface energy of non-stoichiometric surfaces of ϵ-Fe_3C with varying chemical potential of carbon. Calculated with PBE functional. 53
5.8 Side view of slab surfaces constructed of η-Fe_2C. 54
5.9 Surface energy of η-Fe_2C surfaces for PBE, VdW-DF and SCAN-rVV10 functionals and reference values. (*) Asymmetric and stoichiometric surfaces.[93] 55
5.10 Surface energy of non-stoichiometric surfaces of η-Fe_2C with varying chemical potential of carbon. Calculated with PBE functional. 55
5.11 Surface energy of χ-Fe_5C_2 surfaces for PBE, VdW-DF and SCAN-rVV10 functionals and reference values. (*) Asymmetric and stoichiometric surfaces.[67][79] 56

5.12 Surface energy of non-stoichiometric surfaces of χ-Fe_5C_2 with varying chemical potential of carbon. Calculated with PBE functional. 56

5.13 Wulff particles constructed with values from Broos et al.[67] and Liu et al.[79]. (a) Wulff particle with values from Broos et al.[67], (b) Wulff particle with values from (a) and the addition of $(510)_{0.0}$ surface from Liu et al.[79]. Values from PBE functional. 57

5.14 χ-Fe_5C_2 Wulff Particle, (a) calculated from VASP and (b) made with [67] and [79] values. Values from PBE functional. 57

5.15 Surface energy of θ-Fe_3C surfaces for PBE, VdW-DF and SCAN-rVV10 functionals and reference values.[92][95] 58

5.16 θ-Fe_3C Wulff Particle, (a) calculated from VASP, and (b) made with Broos et al.[92] values. Values from PBE functional. 58

5.17 Most stable adsorbed molecules on $\chi(510)_{0.0}$, calculated with PBE. (b) The adsorbed carbon is a light brown colour to distinguish it from other carbon atoms from the slab. . . 60

A.1 Top view of slab surfaces of Hägg Carbide (χ-Fe_5C_2). 73

A.2 Side view of slab surfaces of Hägg Carbide (χ-Fe_5C_2). 74

A.3 Side view of slab surfaces of constructed ϵ-Fe_3C. 74

A.4 Top view of slab surfaces constructed of η-Fe_2C. 75

A.5 Top view of slab surfaces constructed of θ-Fe_3C. 75

B.1 VESTA representation of adsorbed CO over Co(111) on several active sites. 78

B.2 Initial Sate, Transition State and Final State, respectively, of low coverage CO_2 reactions over Co(111). 79

Nomenclature

Constants

$\hbar$	Reduced Planck constant	$1.054 \times 10^{-34}\,\mathrm{J\,s}$
h	Planck constant	$6.626 \times 10^{-34}\,\mathrm{J\,Hz^{-1}}$
k_B	Boltzmann constant.	$1.381 \times 10^{-23}\,\mathrm{J\,K^{-1}}$
N_A	Avogadro constant	$6.022 \times 10^{23}\,\mathrm{mol^{-1}}$
R	Ideal Gas constant	$8.314\,\mathrm{J\,mol^{-1}\,K^{-1}}$

Greek Symbols

α	Chain growth probability.
γ	Unit cell angle between a and b axis.
μ_i	Chemical potential of species i.
π	Pi number, 3.14159.
ψ	Wave function.
σ	Symmetry number.
θ_i	Surface coverage of species i.

Other Symbols

ΔG_f	Gibbs free energy of formation at specific conditions.
ΔH_{exp}	Experimental enthalpy of formation at specific conditions.
ΔH_f	Formation enthalpy at specific conditions.
ΔS_f	Formation entropy at specific conditions.
$\Delta \mathrm{G}_f{}^\circ$	Gibbs free energy of formation of specie at its thermodynamic standard states.
$\Delta \mathrm{G}_r^{673K}$	Gibbs free energy of reaction at 673K.
A	Area.

ABC	products of inertial moments ($gm \times cm^2$).
$E_{adsorbate}$	Adsorbate electronic energy.
$E_{adsorption}$	Adsorption energy.
E_b	Bulk electronic energy.
E_{coh}	Cohesive energy.
E_C^{gas}	Electronic energy of one C atom in gas phase.
E_{Fe}^{gas}	Electronic energy of one Fe atom in gas phase.
E_{Fe}^{gs}	Electronic energy of one Fe atom in the ground state (BCC).
E_{form}	Cohesive energy.
E_{slab}	Slab electronic energy.
$E_{surf.}$	Surface energy.
$E_{surf.}^{non-stoich.}$	Surface energy of a non-stoichiometric surface.
$E_{surf.}^{stoich.}$	Surface energy of a stoichiometric surface.
E_{system}	Electronic energy of the system slab/adsorbate from VASP.
F_i	Outlet molar flow rate of species i, in mol/s
$F_{r,0}$	Inlet molar flow rate of reactant r, in mol/s
F_r	Outlet molar flow rate of reactant r, in mol/s
H_{ads}	Enthalpy of adsorption.
H_{corr}	Corrected enthalpy.
H_{linear}	Enthalpy of linear gas phase molecules.
$H_{non-linear}$	Enthalpy of non-linear gas phase molecules.
m	Molar mass.
n	Amount of bulk unit cells that occupy the slab unit cell.
$n_{C,i}$	Number of carbon atoms in species i.
N_C	Amount of C atoms.
N_{Fe}	Amount of Fe atoms.
P	Pressure.
p_0	Pressure of reference.

p_i	Partial pressure of species i.
r	Rate of reaction.
S_{ads}	Entropy of adsorption.
S_{exp}	Entropy of experimental results.
S_{linear}	Entropy of linear gas phase molecules.
$S_{non-linear}$	Entropy of non-linear gas phase molecules.
T	Temperature.
v_i	Vibrational frequency of species i.
X_r	Conversion of reactant r.
B_0'	Isothermal bulk modulus first derivative with respect to pressure.
B_0	Isothermal bulk modulus.
V	Volume.
V_0	Theoretical equilibrium unit cell volume.
E0	VASP energy obtained in OSZICAR or OUTCAR.

(a, b, c)	VESTA coordinates.
(h, k, l)	Miller indexes.
(x, y, z)	Cartesian coordinates.

Glossary

ASE Atomic Simulation Environment. 23

ASF Anderson–Schulz–Flory is a probability distribution of hydrocarbon products.. 6, 10, 15

ASTM American Society for Testing and Materials. 3

AtJ Alcohol to Jet. 3

BTL Biomass-to-Liquid. 6

CCS Carbon Capture and Storage. 1

CCU Carbon Capture and Utilisation. 1, 4

CHJ Catalytic Hydrothermolysis. 3

cNEB climbing-image Nudge Elastic Band. 28

CTL Coal-to-Liquid. 6

DFT Density Functional Theory. 21

DSHC Direct Sugar to Hydrocarbon. 6

FCC Face Centered Cubic. 23

FS Final State. 35

FT Fischer-Tropsch process. 3

GGA Generalised Gradient Approximation. 22

GHG Greenhouse Gas. 1

GTL Gas-to-Liquid. 6

HC-HEFA Hydroprocessed Hydrocarbons, Esters and Fatty Acids. 3

HCP Hexagonal Close Packed. 23

HEFA Hydrotreated Esters and Fatty Acids. 3

HPC High Performance Computer. 22

IS Initial State. 35

LDA Localised Density Approximation. 22

MEP Minimum Energy Path. 28

MKM Micro-kinetic Modelling. 2, 21

ML Monolayer. 40

MTH Methanol to Hydrocarbons. 8

NEB Nudge Elastic Band. 28

PBE Perdew-Burke-Ernzerhof functional. 24

PTG Power-to-Gas. 12

rVV10 revised Vydrov–van Voorhis nonlocal correlation functional. 24

RWGS Reverse Water Gas Shift. 7

SAF Sustainable Aviation Fuel. 19

SCAN Strongly Constrained and Appropriately Normed meta-generalised gradient approximation. 24

SCF Self-consistence field calculation.. 59

SIP Synthesised Iso-Paraffins. 3

SPK Synthetic Paraffinic Kerosene. 4

Syngas Synthetic Gas ($CO+H_2$). 6

TOF Turnover Frequency. 36

TS Transition State. 28, 35

VASP Vienna Ab initio Simulation Package. 22

VdW-DF Van der Waals - Density Functional. 24

VESTA Visualisation for Electronic Structural Analysis. xiv, xv, 40, 41, 78

VHO Venezuelan Heavy Oils. 3

ZPE Zero-point Energy. 31

Chapter 1

Introduction

Ever since the Industrial Revolution in the past centuries, fossil fuels utilisation (natural gas, oil and coal) has increased enormously. And with it, the concentration of carbon dioxide (CO_2) in the atmosphere, about 50% increase. Before the industrial revolution (1750 to 1800) the CO_2 concentration in the atmosphere was about 278 ppm and in 2021 is about 417 ppm, and constantly increasing.[1] This increase has caused an increase in global temperature and climate change since CO_2 is considered a greenhouse gas (GHG), due to its 'greenhouse effect' on the planet.

For years scientists are working to reduce CO_2 emissions. There are several strategies to address the issue, reduce CO_2 quantity produced, Carbon Capture and Storage (CCS) and Carbon Capture and Utilisation (CCU) processes.[2] The first mentioned necessitates better energy efficiency and turning to other energy sources, like hydrogen and renewable energy. CCS is based on the capture and purification technologies of CO_2 and storage for later use. For the third approach, the CO_2 is captured and converted into value-added products. The hydrogenation reaction is a chemical conversion of CO_2 considered to be very important. Since it reduces the CO_2 amount in the atmosphere and produces chemicals and fuels.

The main sources of CO_2 emissions from human sources are in the industry (chemical, metallurgical, and mineral transformation processes), land use, forestry and agriculture and the burning of fossil fuels (oil, natural gas and coal). The burning of fossil fuels is mainly to produce electricity and heat in industries (on-site burning in energy facilities) and transportation.[3]

For the past 10 years, ground transportation has become less dependent on fossil fuels, since the rise of batteries and the electrification of railways. For aviation, this approach is unsuitable. So for this sector, there is a pressing need to produce sustainable jet fuel to reduce CO_2 emissions. The volatile price of crude oil is an additional incentive to different jet fuel sources.[4]

CO_2 hydrogenation converts CO_2 and H_2 into hydrocarbons. Since the objective is to produce sustainable jet fuel, the hydrogen (H_2) must come from a sustainable source as well (green hydrogen). Water electrolysis is a solution, knowing the energy applied in the electrolysis is from renewable sources (e.g. solar, wind). A lot of researchers are focusing on the development of electrolytic hydrogen systems as this review presents [5].

As the figure 1.1 shows the objective is to have a circular supply of jet fuel. Capture and purification of CO_2 to further react with green H_2 in the presence of a catalyst producing jet fuel. This sustainable jet fuel is distributed to commercial and military airlines suffering engine combustion, releasing CO_2 going back in the cycle.

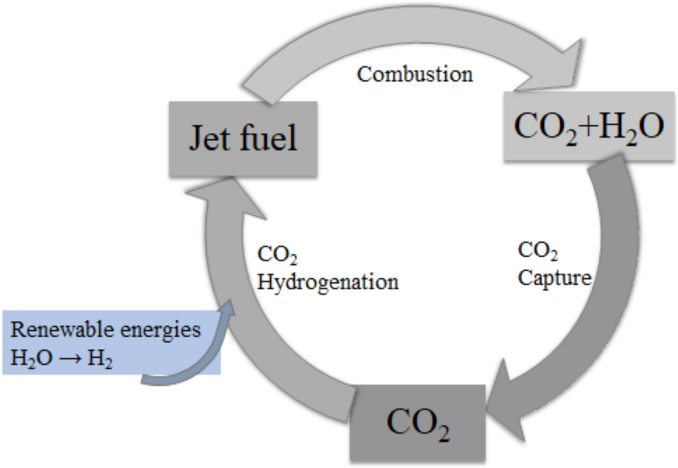

Figure 1.1: Jet fuel production in a circular economy point of view. Adapted from [6].

1.1 Thesis Outline

The general goal is to understand the CO_2 activation and reaction pathway in cobalt and understand iron carbide structures. In Chapter 2 we discuss related work that is relevant to a better understanding of the subject. Chapter 3 explains the methodology applied in the calculations. Chapter 4 describes and discusses the Density Functional Theory (DFT) calculations and microkinetic modelling (MKM) to construct and understand cobalt catalyst active sites and reaction pathways. Chapter 5 demonstrates results and discusses the DFT calculations made on iron carbide structures. Finally, Chapter 6 briefly concludes this thesis and proposes future work.

Chapter 2

State of the art

A viable method of converting trash into riches and energy storage that simultaneously addresses the environmental and energy problems brought on by CO_2 emissions is CO_2 hydrogenation to hydrocarbons. The hydrogenation of CO_2 to various value-added hydrocarbons is the subject of much study and development. This chapter presents an overview of current development on the topic of CO_2 reuse as feedstock. Section 2.1 introduces jet fuel production processes and composition. Section 2.2 presents several renewable processes, such as HEFA, FT, AtJ, SIP, CHJ, HC-HEFA. In Section 2.3 we discuss CO_2 hydrogenation pathways and reactions. In Section 2.4 we introduce catalyst types to obtain hydrocarbons. Mainly Co-based and Fe-based catalysts are the most used to obtain hydrocarbons. Finally, from a commercial point of view, it is discussed processes and companies implementing Sustainable Aviation Fuels (SAF), in Section 2.5.

2.1 Jet Fuel

Jet fuel is a mixture of hydrocarbons, paraffin, olefins, naphthenes, and aromatics with carbon chain lengths ranging from C_8 to C_{16} that are used in gas turbine-powered aircraft. Their composition can vary depending on the source of crude oil, refinery processes, and product specifications.[4] The fuel must be in accordance with standard aviation turbine fuel specifications given by several entities. The ASTM D1655 (United States) and DEF STAN 91/91 (United Kingdom Ministry of Defense) are the most extensively used quality standards.[7][8] Table 2.1 gives several compositions of jet fuels experimentally available in the references cited, being at least 50% paraffins and the rest mainly naphthenes, aromatics, and olefins.

Traditionally, jet fuel has been produced through the conventional crude oil process. Some unconventional crude oil processes (sand oils, Venezuelan Heavy Oils (VHOs), and oil shale) have been developed. Several commercial processes have been devised to effectively and sustainably address the problem of manufacturing jet fuel. Such as renewable processes (using bio-renewable feedstocks such as vegetable oils, animal fats, greases, jatropha plant, algal, and wastes), Fischer-Tropsh (FT) Synthesis process, and more recently CO_2 based processes.[7][13]

Table 2.1: Chemical composition for various Jet-A/JP8 fuels.[9]

	Freeman&Lefebvre[10]	Spadaccini&TeVelde[11]	Vasu et al.[12]	Gokulakrishnan et al.[9]
Paraffins	63.75	63.75	60	51.26
Naphthenes	23.94	23.94	20	31.44
Aromatics	11.26	11.26	18	17.30
Olefins	1.05	1.05	2	0.00

The traditional method (i.e. conventional crude oil process) extracts components by refining crude oil (petroleum), which atmospheric and vacuum fractional distillation are commonly used. The different components have different boiling temperatures, allowing extraction of naphtha, kerosene, gas oil, heavy oil, and residuals from top to bottom in the column. Kerosene is used in the manufacturing of jet fuel and is further treated in a hydrotreater. Jet fuel derived from crude oil typically contains 40% isoparaffins, 20% n-paraffins, 20% naphthenes, and 20% aromatics.

Oil sands, Venezuela's VHOs, and shale oil are among the unconventional oil sources. Although the manufacturing of jet fuel with these oils is feasible and meets the standards, the use of these jet fuels does not reduce GHG emissions. Several types of feedstocks are converted into jet fuel using greener jet fuel manufacturing processes. Commercially available technologies, such as Bio-Synfining^{TM} SPK, which makes synthetic paraffinic kerosene (SPK) from animal fats, greases, vegetables, and algal oils, are already approved. The Ecofining^{TM} SPK method, for example, uses a deoxygenating process to transform vegetable oils and wastes into green jet fuels.[7]

The FT process efficiently converts syngas (CO and H_2) into higher hydrocarbons. FT fuels would further extend the life of turbines and engines because they do not emit sulphur dioxide or sulphuric acid. The FT process creates jet fuel that meets all of the standards and uses a variety of feedstocks, including natural gas, coal, and biomass.

CO_2 hydrogenation can be performed by two mechanisms, chemical or biological, using CO_2 as feedstock to make hydrocarbons. The biological pathway uses microorganisms to convert biomass to methane. The chemical path involves a reaction between CO_2 and H_2 at temperatures between 200 and 500° C, and it can take one of two paths: direct or indirect. [14] FT may be involved in one of the processes that occur as a result of the CO_2 hydrogenation pathway; a more thorough explanation follows. CO_2 hydrogenation has the potential to make jet fuel production carbon-neutral (figure 1.1).

Hydrogen plays an important role in CO_2 hydrogenation and FT processes. Its source can vary from water, methane, butane or other hydrocarbons since it is not found in a gas form naturally, but in other compounds. Depending on the source and production of hydrogen it can be classified as green, grey or blue. The grey hydrogen is synthesised through the steam methane reforming method, and the blue hydrogen is the grey hydrogen that goes through the CCU process. Both these types come from fossil fuels thus releasing greenhouse gases in the process. In the meantime, green hydrogen is produced from renewable sources, e.g. water splitting (electrolysis process) forming pure oxygen and hydrogen.[5]

Renewable jet fuel processes supply alternative fuels which have a potential environmental benefit and reduce life cycle greenhouse gas (GHG) emissions. Economic benefits include increased fuel availability and lower fuel costs. However, for CO_2 hydrogenation and FT processes, H_2 production itself accounts for more than half the capital investment. The availability of FT jet fuels within the next decade depends on feedstock, the world price of oil, resolving uncertainties in production costs, and regulatory and technical issues, such as capturing and storing large quantities of CO_2, more precisely in CO_2 hydrogenation.

2.2 Bio-Processes

Several sustainable conversion pathways have been studied and reviewed in [15][16]. Among the bio-jet fuel production pathways are HEFA, AtJ and FT. The production pathway is dependent on the feedstock and this can vary from triglyceride, lignocellulosic, starchy and sugar biomasses. Feedstock cost accounts for 60-75% of total production costs, so this constitutes a barrier to the economic production of sustainable bio-jet fuel.[15] In figure 2.1 the processes are shown.

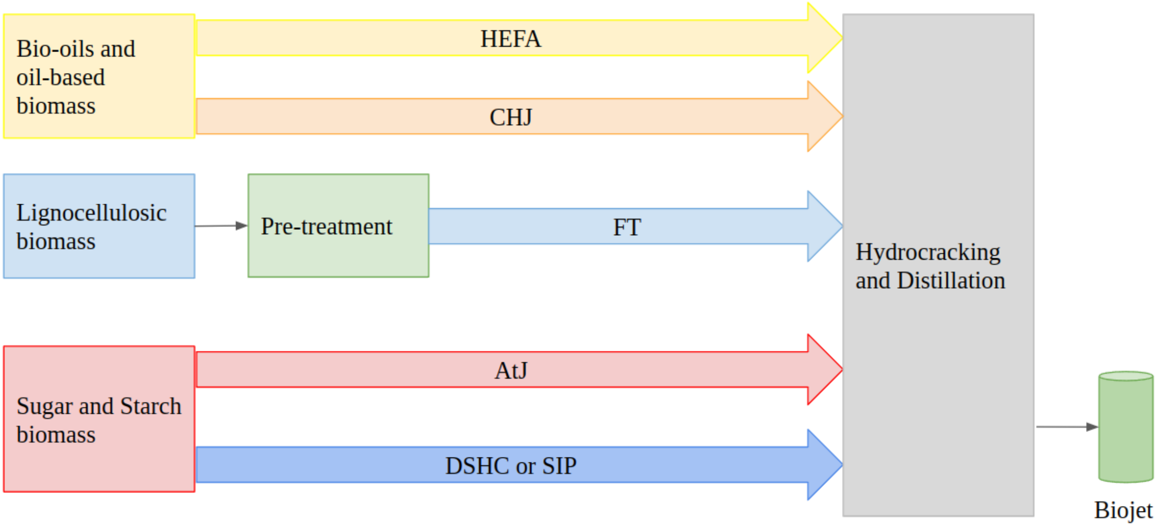

Figure 2.1: Conversion pathways to bio-jet fuel production. Adapted from [15].

HEFA is a catalytic hydro process of biomass to biofuel. The production process consists of oil extraction and hydroprocessing.[15] Many different types of vegetable oils and fats can be used to make HEFA oil. This includes animal fats as well as triglycerides and fatty acids from vegetable oils (such as rapeseed, soybean, and corn oil), tall oil (a byproduct of the pulp and paper industry), and other sources.[17] The hydroprocessing chemical process involves the removal of the oxygen from the ester and fatty acid by a series of hydrodeoxygenation, decarboxylation, and decarbonylation processes. The shorter chain alkanes in most cases have to be cracked multiple times and isomerized to produce bio-jet fuel range fuels. The reaction temperature and pressure influence the cracking and isomerization process, as well as the catalyst. Pt, Ni, or other precious metals supported by activated carbon, Al_2O_3, and zeolite molecular sieves are examples of commonly used catalysts for the isomerization and cracking processes.

AtJ is an alternative pathway for biomass conversion to hydrocarbons. The feedstock includes bio-alcohols produced from sugars, starch and lignocellulosic biomass. The process consists of 3 reactions, dehydration of alcohol, oligomerisation and hydrogenation, followed by a purification stage to obtain green diesel, bio-jet fuel and naphtha.[15]

Synthesised iso-paraffins (SIP) are produced from hydroprocessed fermented sugars. The process has two stages, first, the sugar is converted into an unsaturated hydrocarbon molecule, farnesene ($C_{15}H_{32}$) (DSHC). In the second stage, the farnesene is converted into jet fuel via a hydrotreatment process, giving SIP fuel. SIP fuels mainly hydrocarbons in the upper range of the molecular size distribution of Jet A-1 fuel (C_{15}-C_{16}).[15][18]

The FT method was developed by German researchers Franz Fischer and Hans Tropsch (giving Fischer-Tropsch, FT) to produce liquid fuels from coal. The main reaction of this chemical process is represented in the equation 2.4, occurring over a solid catalyst to produce liquid hydrocarbons.[19] During the FT process many different hydrocarbons are produced. To produce synthetic fuels (from coal, natural gas or biomass) usually, the catalyst and process conditions are chosen to favour long-chain hydrocarbon production and minimise methanation and the production of light olefins, oxygenated species and branched alkanes.[19] However, due to ASF curve, even if α is high the light olefins and paraffin are always present.

To produce renewable fuels from FT, first, the feedstock must be gasified producing Syngas ($CO+H_2$) followed by the FT reaction to produce liquid fuels. Depending on the feedstock, the process can have different names, such as Biomass-to-Liquid (BTL), Gas-to-Liquid (GTL) and Coal-to-Liquid (CTL).[15] The gasification process utilises a variety of feedstocks, including waste-derived materials, making it a highly sustainable process. The gasification is ruled by the following reactions happening all at once.

$$Water-gas\ shift:\ CO+H_2O \rightleftharpoons CO_2+H_2 \tag{2.1}$$

$$Steam\ reforming:\ CH_4+H_2O \rightleftharpoons CO+H_2 \tag{2.2}$$

$$Dry\ reforming:\ CH_4+CO_2 \rightleftharpoons 2CO+2H_2 \tag{2.3}$$

$$FT\ paraffins\ synthesis:\ nCO+(2n+1)H_2 \rightleftharpoons C_nH_{2n+2}+nH_2O;\ (n=1,2,3...) \tag{2.4}$$

FT is typically catalysed by cobalt or iron catalysts at high temperatures (300-350° C) or low temperatures (200-240° C). Cobalt is often utilised at low temperatures, whereas iron may be used in both types of FT processes. The product composition can range from gasoline (C_5-C_{20}) and low molecular mass linear olefins (C_2-C_4) to high molecular mass linear waxes ($>C_{20}$), depending on the reaction conditions and the catalyst.[15] Therefore, the FT reaction's ability to regulate product composition makes it possible to refine synthetic oils into bio-jet fuel range values.[7]

2.3 CO_2 Hydrogenation

Carbon dioxide hydrogenation to long-chain hydrocarbons can be direct or indirect, being the overall reaction presented in equation 2.5.

$$nCO_2 + 3nH_2 \rightleftharpoons C_nH_{2n} + 2nH_2O;\ (n = 1, 2, 3...) \tag{2.5}$$

CO_2 hydrogenation can create a variety of compounds, including C_1 products, olefins, C_{5+} hydrocarbons, and higher alcohols. CH_4, CO, and CH_3OH are C1 intermediates produced by CO_2 hydrogenation.

Figure 2.2 illustrates the different possible pathways of CO_2 hydrogenation and its intermediates to produce liquid hydrocarbons. The hydrogen is produced through water electrolysis using renewable energies (e.g., solar), and the CO_2 would be captured using CCS technologies from high-emission industries.

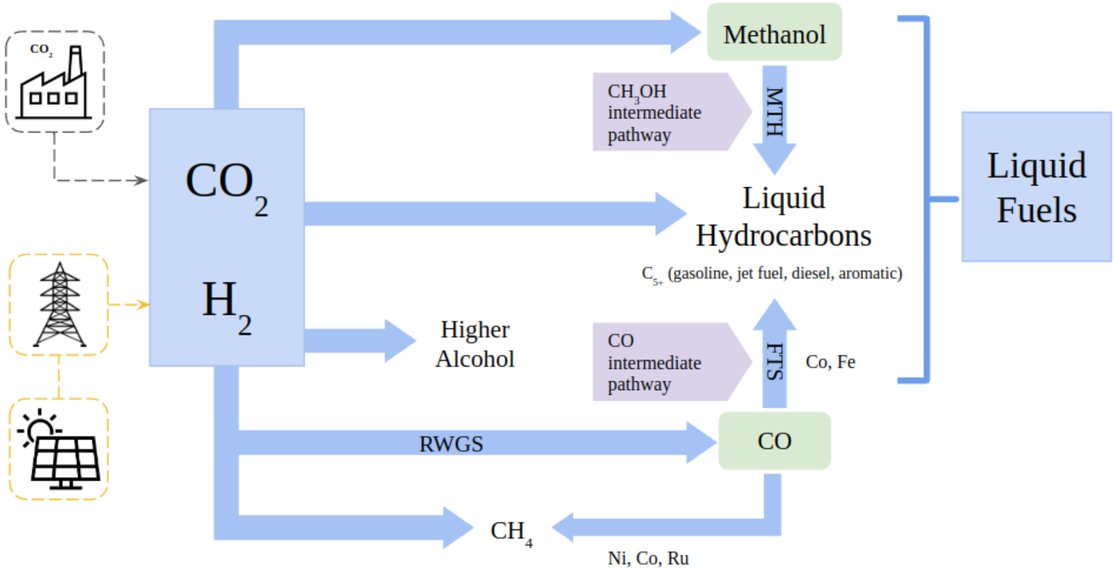

Figure 2.2: Pathways of CO_2 conversion to hydrocarbons. Adapted from [20], [21] and [22].

Methanation is the most favourable process among the other processes for CO_2 utilisation, with a ΔG_r^{673K} of -40kJ/mol; CO is generated by reverse water gas shift, RWGS, with a ΔG_r^{673K} of 14kJ/mol. The methanol synthesis has the least favourable ΔG_r^{673K} of 75kJ/mol. As a result, methanol synthesis is the most expensive since it consumes more energy.[23] RWGS is the better option when the target is C_{5+} products. Although, chain termination is favoured to produce CH_4 and C1 products.

Carbon dioxide is a thermodynamically stable molecule, thus it can be hard to react for C-C coupling reactions in hydrogenation. As a result, CO_2 hydrogenation often produces products with high H/C ratios due to quick methane production.[24][21] Which is mostly due to the low heat of CO_2 adsorption on active catalyst surfaces where higher amounts of dissociated H* lead to a high H/C ratio on the catalyst surface. This promotes early hydrogenation of intermediates that are adsorbed on the surface, finishing the reaction by desorbing products like methane and others.[21][24] CO_2 presents a high kinetic barrier of formation and intrinsic inertness ($\Delta G_f{}^\circ = 396$ kJ/mol) which makes it difficult for C-C coupling processes, potentially lowering the C_{5+} hydrocarbons selectivity.[24]

A measure for the chain growth is the chain-growth probability, which is the probability of C-C coupling occurring (i.e., the probability one monomer unit is added to the growing chain). Naturally, α is related to the C-C coupling barrier. To enhance α and inhibit chain termination, the H/C ratio on the catalyst surface needs to be adjusted.[21] However, there is little understanding of the catalyst's active sites for CO_2 hydrogenation and its mechanism, especially CO_2 activation.

Indirect Route

The indirect route converts CO_2 into methanol, which is then converted to liquid hydrocarbons via the methanol-to-hydrocarbons process (MTH).[25][26][27] The production of hydrocarbons with MTH usually is made with a zeolitic catalyst (e.g. HZSM-5, SAPO-34).[14] A zeolite can help to provide the appropriate product distribution and selectivity. Cu-based catalysts (bifunctional or supported catalysts) are mainly used in this route, where CO_2 hydrogenation occurs on Cu.[14]

However, the RWGS reaction is competitive with methanol formation and converts CO_2 into unwanted CO. Lowering the reaction temperature helps methanol formation but it also results in low CO_2 conversion. Obtaining high CO_2 conversion and high methanol selectivity at the same time remains a significant challenge.[20][14]

Usually, the reaction 2.6 is considered the rate-limiting step for most catalysts. Furthermore, it has been demonstrated that oxygen vacancies on metal oxide surfaces facilitate CO_2 activation.[20] Supposedly, methanol is generated after CO_2 activation via a formate intermediate pathway, as shown in 2.6. The formate species usually formed are HCOO*, but also the formation of hydrocarboxyl specie COOH* has been observed.[14][2]

$$CO_2 + 3H_2 \longrightarrow CH_3OH + H_2O \tag{2.6}$$

The mechanism of methanol to hydrocarbons occurs via two steps:[27][14]

- Short induction-period - two methanol molecules couple through surface methoxy species forming a C-C bond

- Auto-catalytic dual cycle mechanism (alkene and arene cycles) - includes methylation, olefin cracking, aromatic methylation and de-alkylation, H_2 transfer, and cyclization. Figure 2.3 shows the representation of the dual cycle.

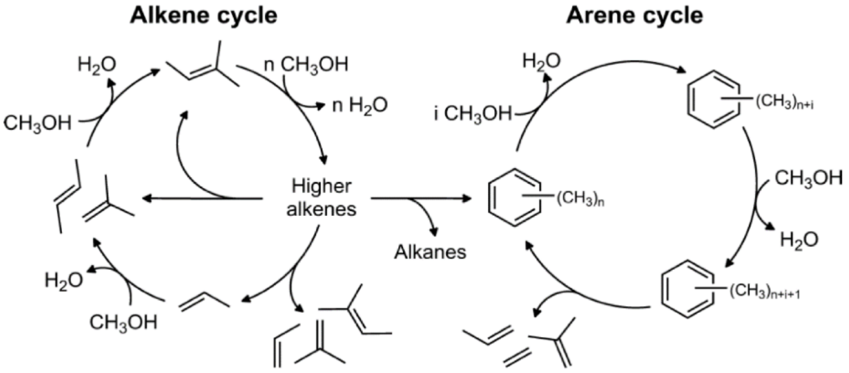
Alkene cycle
Arene cycle
H₂O
n CH₃OH
n H₂O
CH₃OH
Higher alkenes
Alkanes
H₂O
CH₃OH
H₂O
i CH₃OH
(CH₃)n+i
(CH₃)n
CH₃OH
H₂O
(CH₃)n+i+1

Figure 2.3: Auto-catalytic dual cycle mechanism (alkene and arene cycles) representation. Image of [14].

Methanol synthesis is an energy-intensive process even though MTH is an effective path to higher hydrocarbons is not the desired path in this research.[14]

Direct Route

The direct route combines both the RWGS and FT reactions which are represented by the equations 2.7 and 2.4, respectively.

$$CO_2 + H_2 \rightleftharpoons CO + H_2O \tag{2.7}$$

The carbon dioxide is reduced to carbon monoxide via RWGS reaction through decomposition of *COOH intermediates (giving *CO, *OH) or direct cleavage of C-O bond (of O-C-O molecule), to form *CO. CO will undergo dissociative ($*CO + * \longrightarrow C* + O*$) or H-assisted dissociative on the active metal surface, and *CO hydrogenation forming HCO*.[26] The hydrogen insertion on *CO while dissociation occurs forms $*CH_x$ intermediates. Then, from $*CH_x$ species the chain growth starts and the final step is the termination of chain growth through dehydrogenation, hydrogenation or insertion of *CO all happening consecutively on the catalyst surface.[26][28]

Because RWGS is an endothermic reaction, high temperatures are necessary to obtain acceptable conversions. CO_2 conversion up to 50% can be achieved at 200-600° C (e.g. at 350° C was achieved) with one metal catalyst (Cu and noble metals, Pt, Pd, Rh based catalysts). However, FT reaction prefers to operate at lower temperatures (exothermic) and for both reactions to be effective, they must be efficiently catalysed under the same conditions. The catalyst must be active in both RWGS and FT reactions.[26]

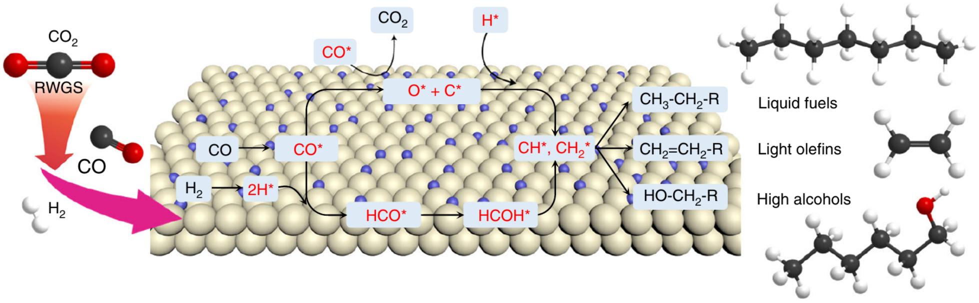
CO₂
RWGS
CO
H₂
CO*
CO₂
H*
O* + C*
CO
CO*
H₂
2H*
HCO*
HCOH*
CH*, CH₂*
CH₃-CH₂-R
CH₂=CH₂-R
HO-CH₂-R
Liquid fuels
Light olefins
High alcohols

Figure 2.4: Representation of a CO_2 FT reaction mechanism over a catalyst. Image of [26].

The second reaction, FTS, will generate hydrocarbons by hydrogenating carbon monoxide, following the Anderson–Schulz–Flory (ASF) distribution (figure 2.5) due to its similarity to the polymerisation mechanism.[28] The ASF is a statistical distribution of hydrocarbon products and is determined by the chain growth probability (α).[21][28][29]

According to figure 2.5, methane is the most abundant product at low α, while at higher α the overall amount of methane created can be reduced. Also, heavier hydrocarbons require a high chain growth probability. Generally, the catalyst and the process conditions have a big impact on α.

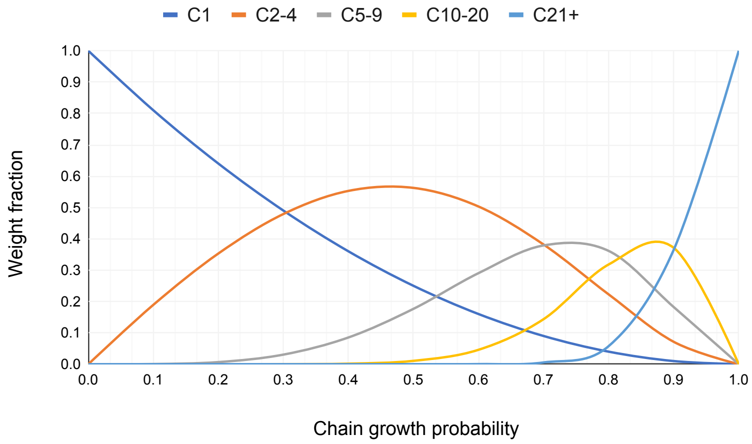

Figure 2.5: ASF Distribution weight fraction (w_i) vs chain growth probability. The graph was constructed using $w_i = \alpha^{i-1}(1-\alpha)^2 * i$, being i the number of carbons. Formula and principle of construction of [30], [29] and [31].

After the RWGS process, C-C coupling occurs to yield C_{5+} hydrocarbons, such as jet fuel. There is a vast range of products produced depending on the structure and content of the catalysts. Iron, cobalt, and ruthenium catalysts are the most frequently used catalysts in this process. They can be promoted by an alkali metal and supported by a metal oxide to achieve the required products.[26]

The direct route will be the primary emphasis of this project. Because it has fewer chemical process steps and consumes less overall energy, it is usually viewed as being more cost-effective and environmentally friendly.[32]

2.4 Catalysts for CO_2 conversion

There have been numerous attempts to find the right catalysts for CO_2 conversion to hydrocarbons [6][24][31-35]. So several metals were tested, Co, Cu, Ru, Ni, and Fe. To produce higher hydrocarbons these catalysts must be optimised to minimise methane production and enhance the C-C coupling reaction (increasing α).

Co-based, Fe-based, and Ru-based catalysts are proposed for CO_2 hydrogenation in recent research [33][32][20][14]. Ruthenium is a rare and expensive element that is inappropriate for large-scale uses.[34] Various factors can have an impact on the reaction mechanism, CO_2 conversion, C_{5+} selectivity, and product distribution:

- Structure and composition of the catalyst
- Promoters (K, Na, Cu, Zn, Mn and more alkali metals)
- Support (oxide supports, ZrO_x, AlO_x, TiO_x, MnO_x)
- Active phase and nature of the active sites

There are a lot of studies focusing on FT and the catalysts used in FT. Limited studies explain the CO_2 hydrogenation mechanism and the catalyst effect on higher hydrocarbon production, more precisely jet fuel production.

Compared to Fe-based catalysts, Co-based catalysts have reduced RWGS activity. However, Co catalysts perform better catalytically and are more stable to produce higher alcohols and liquid fuels when compared to Fe catalysts.[22] The best FT catalysts for GTL processes processing syngas (CO/H_2) feedstocks are cobalt-based, however, they exhibit high methanation rates and inferior selectivities to liquid (C_{5+}) hydrocarbons under CO_2 hydrogenation conditions.[31]

Fe-based catalysts can catalyse both RWGS and FTS processes since it presents different sites and phases during the reaction, chain growth sites, and hydrogenation sites.[35][26]

Catalysts can be supported with oxides and promoted by a second metal or alkali metal. Several papers reveal their impact on product distribution improvement and reaction optimisation.[14][20]

Several noble metal and transition metal catalysts were investigated in CO_2 hydrogenation to hydrocarbons. Transition metals (Ru, Rh, Ni, Pd) have strong methanation activity and selectivity.[36][14] Several researchers have experimented with support, such as zeolite-based catalysts and bifunctional catalysts to get a better product distribution.[37][38][25][24][6][39][40]

Methanation catalysts

Transition metals such as Ru, Rh, Ni and Pd show excellent activity and selectivity in CO_2 methanation.[14] Among those metals, Ni is cheaper with a high CO_2 hydrogenation activity, it has been widely employed as a methanation catalyst. CO and CO_2 methanation over Ni catalysts supported on γ-Al_2O_3, SiO_2, TiO_2, CeO_2, and ZrO_2 were examined by Le et al. [41]. The reaction used a feed composition of 50 mol% H_2, 1 mol% of CO_2 or CO and 49 mol% of He, 0.1 g of catalyst, and a temperature range of 100-450° C. For both CO and CO_2 hydrogenation, the catalyst with the support CeO_2 was found to be the most active, with activity proportional to CeO_2 surface area. This can be explained by the high Ni dispersion and intimate contact between Ni and Ce. As seen in figure 2.6, the Ni/CeO_2 catalyst achieved a CO_2 conversion of 100% at 230° C, methane is the predominant product. Different Ni contents were tested, and $Ni_{0.8}Ce_{0.2}O_x$, which has a high Ni content and small Ni particles (crystallite size of Ni 12 nm), was shown to be the best catalyst for methanation.

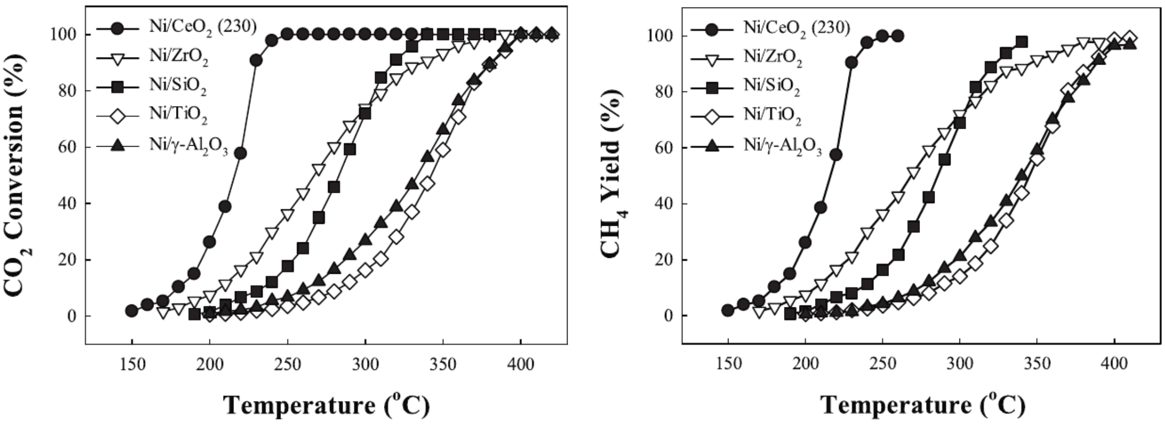

Figure 2.6: CO_2 conversion and CH_4 yield with temperatures ranging from 150° C to 450° C during CO_2 methanation on supported Ni catalysts. Image from [41].

Vogt et al. [42] investigated Ni methanation in the PTG concept, assessing structural sensitivity and different supports (Al_2O_3, CeO_2, ZrO_3 and TiO_2) under various reaction conditions (temperature from 200 to 500° C and pressures from 5 to 20 bar). Because there is a competition between the coupling of C fragments on Ni surfaces and the hydrogenation of C fragments to generate methane, methane formation is preferred over the C-C coupling reaction on Ni catalysts. Catalyst testing revealed that the type of support does not affect the apparent activation energy, implying that the reaction takes place primarily on Ni nanoparticles and that the support effect only influences Ni particle size and shape. Small Ni particles produce more CO, which can be associated with the inability of CO dissociation on small Ni particles, while CO_2 formed CO on small Ni particles.

Figure 2.7 shows the three possible pathways to form CH_4 over Ni catalysts. Experimentally it has been proven that CO_2 activation occurs through two parallel particle size-dependent mechanisms over Ni. First CO_2 dissociation to CO occurs via a formate intermediate (formate pathway) or directly through adsorbed CO_2. CO can then be hydrogenated to CH_4 or further dissociated to CH (carbide pathway). These two pathways have been considered active, but the carboxyl or alcohol pathway has not been shown to exist over Ni.[42] Partly because the formation of COOH* is thermodynamically unfavourable and the following intermediates have higher energy of formation. The carbide pathway has the lowest energy when comparing all pathways potential energy diagrams.[42]

C-C coupling on Ni catalysts is favoured in some cases and it seems not to prefer either terrace or facet sites. Therefore, a very high relative hydrogenation rate should be the only explanation for the consistently observed high methane selectivity for Ni catalysts. To create even more C-C linked products, it may be desirable to partially cover the Ni nanoparticles while ensuring that there is enough CO present to start the carbide pathway.[42]

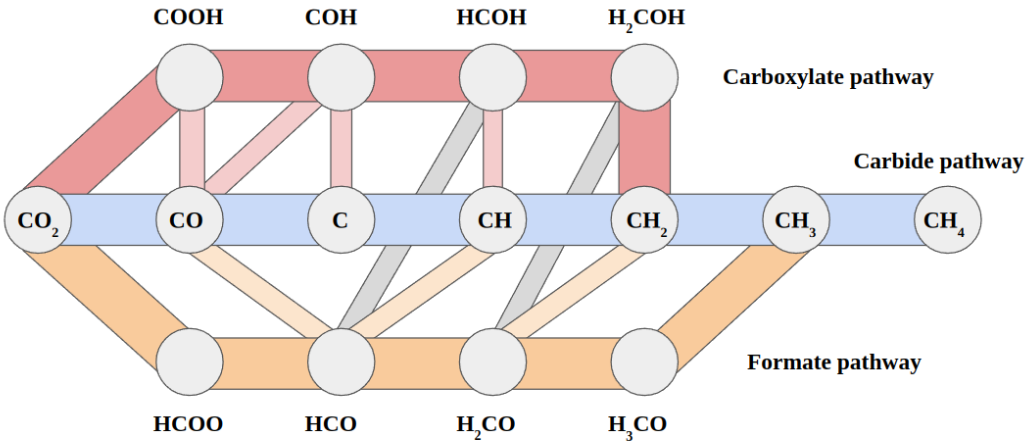

Figure 2.7: Diagram showing all potential CO_2 activation reaction pathways over Ni in the colours pink (carboxylate pathway), blue (carbide pathway), and yellow (formate pathway). Grey dots represent all intermediates. Other lines show possible connections between the main paths. Adapted from [42].

Co based Catalysts

Fe and Co-based catalysts are found to be very active in hydrocarbon production. Though Co has little activity for RWGS, to form high hydrocarbons usually a support is added. The introduction of a promoter such as alkali metals or support (metal oxides or zeolites) helps to enhance α and decrease methane formation. Phathutshedzo [25] studied the effect of potassium on Co/ZrO_2 catalysts during CO_2 hydrogenation to hydrocarbons. For the catalyst with no potassium, methane was the main product with 99.4% selectivity. Evaluating 1 wt.%, 3 wt.%, and 5 wt.% of potassium loading on the catalyst, the 1 wt.% showed the highest α and the highest yield of 13.1% for C_{2+} (20.9% yield for CH_4) at 41% CO_2 conversion. The C_{5+} selectivity obtained was 18.2% and 31.9% of C_{2+} selectivity on the catalyst with 1 wt.% of K. The addition of potassium showed increased CO_2 adsorption resulting in a lower surface H/C ratio which decreases CO_2 conversion. Additionally, it suppressed methane formation and increased C_{5+} selectivity.

Similarly, Zhenhong He et al., [38] tested CO_2 hydrogenation on Co_6/MnO_x catalyst at 200° C, 8 MPa and CO_2/H_2 ratio of 1. The Co_6/MnO_x constitutes Co^0 and MnO crystallites, with Co-Mn bimetallic atom ratio of 6 Co to 1 Mn. At a CO_2 conversion of 15.3% the C_{5+} selectivity obtained was 53.2 C-mol% (C_5 to C_{26}, mostly n-paraffin), and C_1-C_4 selectivity of 46.4 C-mol%. Only 0.4 C-mol% selectivity of CO was observed. It was observed that the major catalyst was Co and Mn was the promoter. When using the same method for pure Co^0, the C_{5+} selectivity observed was 18.7% and 80.7% of C_1-C_4. So, the presence of Mn enhanced CO_2 conversion and weakened H_2 adsorption on the catalyst, facilitating chain growth.

Pure Co-based catalyst without promoters (Co/MIL-53(Al)[1]) was also investigated by Tarasov et al. [43] and Isaeva et al. [44] to show high performance for both CO-FT and CO_2-FT. Tarasov et al. tested a 10%Co/MIL-53(Al) sample in a fixed bed reactor with a feed ratio of $H_2/CO_2 = 2.7$ at 30 atm (3MPa) and different temperatures (260° C, 300° C and 340° C). At 260° C the C_{5+} selectivity obtained was 35% at a CO_2 conversion of 25.3%. The CH_4 and C_2-C_4 selectivities were 35.2% and 29.8%, respectively.

---

[1] MIL-53(Al) is a microporous metal-organic framework (MOF).

It was observed that with increasing temperature of reaction the selectivity of C_{5+} decreased, and of CH_4 increased. Isaeva et al. tested Co@MIL-53(Al) with different Co compositions (5%Co, 10%Co and 15%Co) for CO-FT. At 20bar (2MPa), 240° C and a feed ratio of $H_2/CO=2$ the highest selectivity of C_{5+} was 73.1% with the 15%Co@MIL-53(Al) catalyst. And, the CH_4 and C_2-C_4 selectivities were 14.2% and 10.7%, respectively.

Some have tested bimetallic catalysts. Shi et al., [45] tested $CoCu/TiO_2$ pure catalysts for different K loading (1.5 to 3.5 wt.%). Under the reaction conditions of 5 MPa, 250° C and H_2/CO_2 ratio of approximately 3:1. The unpromoted catalyst produced mainly methane (89.5 C-mol%), while upon addition of 2.5wt.% of potassium the methane formation was reduced to 35 C-mol% and the C_{5+} formation 35.1 C-mol% at 13% of CO_2 conversion.

In a fixed bed reactor, the Na-Co-Mo/SiO_2-TiO_2 catalyst was tested at 200° C, 0.1 MPa, and a feed with a H_2/CO_2 ratio of 3:1.[39] A C_{5+} selectivity of 27.3% was obtained at a CO_2 conversion of 26.9%, and the methane selectivity is 40%. Finally, increasing the TiO_2 concentration on the mixed support improved the C_{2+} selectivity while decreasing the CH_4 selectivity.

Fe based Catalysts

Fe-based catalysts are more RWGS active and hence may be utilised in both RWGS and FTS processes. They are also less expensive. Nonetheless, promoters and supports are utilised to enhance α and diminish CH_4 selectivity. Choi et al. [40], who produced a Cu-Fe catalyst from delafossite-$CuFeO_2$, demonstrated the impact of Cu promoter in Fe catalysts. Under reaction conditions of 300° C, 10 bar, a 3:1 H_2/CO_2 ratio and for 6-24h, the $CuFeO_2$-6[2] catalyst attained a C_{5+} selectivity of 65% and reduced CH_4 production to 2-3%. The copper metal acted as a reduction promoter, allowing the Fe catalyst to reduce more easily, resulting in the formation of Hägg carbide (χ-Fe_5C_2), which is proposed to be active in FT reaction.

Albrecht et al. [46] tested a Fe_2O_3 catalyst prepared following the cellulose-template synthesis method. The CO_2 hydrogenation was performed at 15 bar, 623 K and a H_2/CO_2 ratio of 3. Obtaining a C_{5+} selectivity of 36% and a C_2-C_4 selectivity of 37% at a CO_2 conversion of 40%. While the CH_4 and CO selectivities were 12 and 15%, respectively. The introduction of promoters like K, Na, Cu, Zn, Mn, and/or Ce to Fe catalysts helps decrease CH_4 selectivity and increase chain growth capability. Albrecht et al. [47], tested the effect of sodium on Fe_3O_4-based nanocatalysts for CO_2 hydrogenation. Under reaction conditions of 320° C, 3 MPa and H_2/CO_2 ratio of 3, a maximum C_{5+} selectivity of 30.1% was obtained for FeNa(0.16) catalyst with a Na/Fe weight ratio of 0.16 at a CO_2 conversion of 38.4%. However, the catalyst FeNa(1.18) with a Na/Fe weight ratio of 1.18, produced more C_2-C_4 olefins and C_{5+} hydrocarbons with a yield of 15.7% and 10.1%, respectively. With, C_2-C_4 olefins and C_{5+} selectivities of 46.6% and 30.1%, respectively at a CO_2 conversion of 40.5%. The CH_4 selectivity was 15.8% and to CO was 13.5%. Figure 2.8 shows Na addition significantly reduced the CH_4 production and increase the C_2-C_4 olefins and C_{5+} hydrocarbons.

---

[2] Synthesis time of 6h.

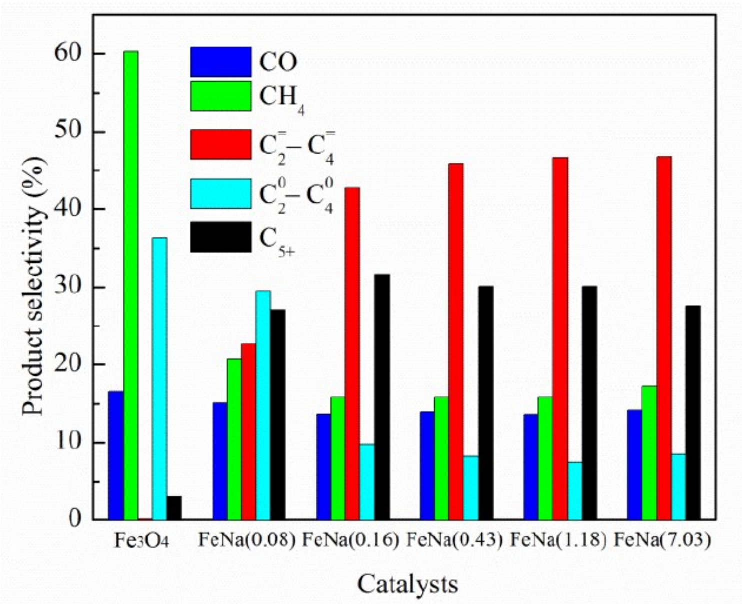

Figure 2.8: Product selectivity of Fe_3O_4-based catalysts. Image from [47].

The results indicate that modified Fe catalysts may achieve excellent C_{5+} selectivity (up to 65%) while yet allowing for wide product distribution. According to ASF distribution, the selectivity of jet fuel (C_8-C_{16}) cannot exceed 41%.[32][30]

Despite this, several authors have been able to break the ASF distribution for jet fuel selectivity. Yao et al. [6], used the Organic Combustion Method to synthesise the Fe-Mn-K catalyst. The conversion of CO_2 into hydrocarbons was carried out at 300° C, 1 MPa, and a 3:1 ratio of H_2/CO_2. At a CO_2 conversion of 38.2%, C_8-C_{16} selectivity was equal 47.8%, and CH_4 and CO selectivity was 10.4% and 5.6%, respectively.

Zhang et al.[32] produced jet fuel with CO_2 in the range of C_8-C_{16} hydrocarbons using a Na-modified CoFe alloy catalyst with double-hydroxide precursors. The reaction was performed at 240° C, 3 MPa, with a H_2/CO_2 ratio of roughly 3:1. At a CO_2 conversion rate of 10.2%, the C_8-C_{16} hydrocarbons selectivity was 63.5%. The metallic CoFe alloy is the active phase in the production of C_{2+} hydrocarbons from CO intermediate, which combined spectroscopic and computational research confirm. In CO_2 hydrogenation, iron oxide surface sites produce CO. When comparing with the results of unpromoted CoFe catalyst (CH_4 and C_{8+} selectivity of 70.3% and 27.1%, respectively at a CO_2 conversion of 19.6%), the addition of Na reduced methane production and aided chain growth, increasing C-C coupling events. Because the RWGS reaction is preferred at high reaction temperatures (>300° C), most CoFe, Fe, or oxide/zeolite bifunctional catalysts designed for the hydrogenation of CO_2 to higher hydrocarbons tend to yield substantial quantities of CO as a by-product.[32] Since CO is produced in RWGS reaction and with increasing temperature CO_2 conversion is increased and more CO is produced.[48]

Table 2.2: Catalysts performance in CO_2 hydrogenation to hydrocarbons.

Catalyst	Product	Temp (° C)	Feed Ratio	Pressure (MPa)	Selectivity (%)	CO2 conv. (%)	Ref
Co	CH_4	240	$H_2/CO_2 = 3$	3	89.9	49.3	[32]
15%Co/ZrO_2	CH_4	275	$H_2/CO_2 = 3$	1	99.4	49.2	[25]
Fe_3O_4	CH_4	320	$H_2/CO_2 = 3$	3	60.3	29.3	[47]
CoFe	CH_4	240	$H_2/CO_2 = 3$	3	70.3	19.6	[32]
15%Co-1%K/ZrO_2	C_{5+}	275	$H_2/CO_2 = 3$	1	18.2	41.0	[25]
Co^0	C_{5+}	200	$H_2/CO_2 = 1$	8	18.7	-	[38]
Co_6/MnO_x	C_{5+}	200	$H_2/CO_2 = 1$	8	53.6	15.3	[38]
10%Co/MIL-53(Al)	C_{5+}	260	$H_2/CO_2 = 2.7$	3	35	25.3	[43]
CoCu/TiO_2	C_{5+}	250	$H_2/CO_2 = 3$	5	4.9	23.1	[45]
2.5 K-CoCu/TiO_2	C_{5+}	250	$H_2/CO_2 = 3$	5	35.1	13.0	[45]
Na-Co-Mo/CeO_2	C_{5+}	200	$H_2/CO_2 = 3$	0.1	31.2	15.1	[39]
Na-Co-Mo/SiO_2-TiO_2[a]	C_{5+}	200	$H_2/CO_2 = 3$	0.1	27.3	26.9	[39]
$CuFeO_2$-6[b]	C_{5+}	300	$H_2/CO_2 = 3$	1	66.3	17.3	[40]
Fe_2O_3-CT[c]	C_{5+}	300	$H_2/CO_2 = 3$	1.5	36	40	[46]
FeNa(0.16)	C_{5+}	320	$H_2/CO_2 = 3$	3	31.6	38.4	[47]
FeNa(1.18)	C_{5+}	320	$H_2/CO_2 = 3$	3	30.1	40.5	[47]
Fe-Mn-K	C_8-C_{16}	300	$H_2/CO_2 = 3$	1	47.8	38.2	[6]
CoFe-0.81wt.%Na	C_8-C_{16}	240	$H_2/CO_2 = 3$	3	63.5	10.2	[32]

[a] 20 wt.%Co–1 wt.%Na–1 wt.%Mo supported on mixed 50 wt.%SiO_2-50 wt.%TiO_2 oxides.
[b] Synthesis time (h).
[c] Cellulose-template synthesis method.

Zeolite based catalysts

Since the selectivities to C_{5+} are normally low, some researchers focused on the incorporation of a zeolite on a metal oxide forming a composite metal oxide/zeolite composite catalyst. Furthermore, zeolites have also been thoroughly studied, particularly in the CO_2 hydrogenation method of producing gasoline. This is due to the shape-selective properties of zeolites and their production of varied pore structures.[14] This shape's selective properties provide a less broad product distribution and a more specific product distribution depending on the type of zeolite, which acts like a molecular sieve. Zeolites are very active in a wide range of reactions due to their clearly defined pore structure and adjustable acidity.[14]

Because zeolite-based catalysts have been employed in the manufacturing of gasoline, various studies have been published on the synthesis of gasoline by CO_2 hydrogenation utilising zeolite-based catalysts.

Wei et al.[37] developed a Na-Fe_3O_4 nanocatalyst and evaluated many zeolites for CO_2 hydrogenation (HY, HBEA, HMOR, HZSM-23, HMCM-22, and HZSM-5) The Na-Fe_3O_4/HZSM-5 multifunctional catalysts had a C_5-C_{11} products selectivity of 78%, at CO_2 conversion of 22%, under reaction conditions of 320° C, 3 MPa, and a H_2/CO_2 ratio of 1:1. The CH_4 and C_{5+} selectivity was 4% and 79.4%, respectively. The influence of the zeolite is seen in the chain growth probability, and hence results in the production of gasoline range products, as shown in the figure 2.10. RWGS is proposed to occur over Fe_3O_4 sites, olefin synthesis occurs over Fe_5C_2 sites, and oligomerisation, aromatisation, and isomerization occur over zeolite acid sites, as the figure 2.9 shows simplistically.

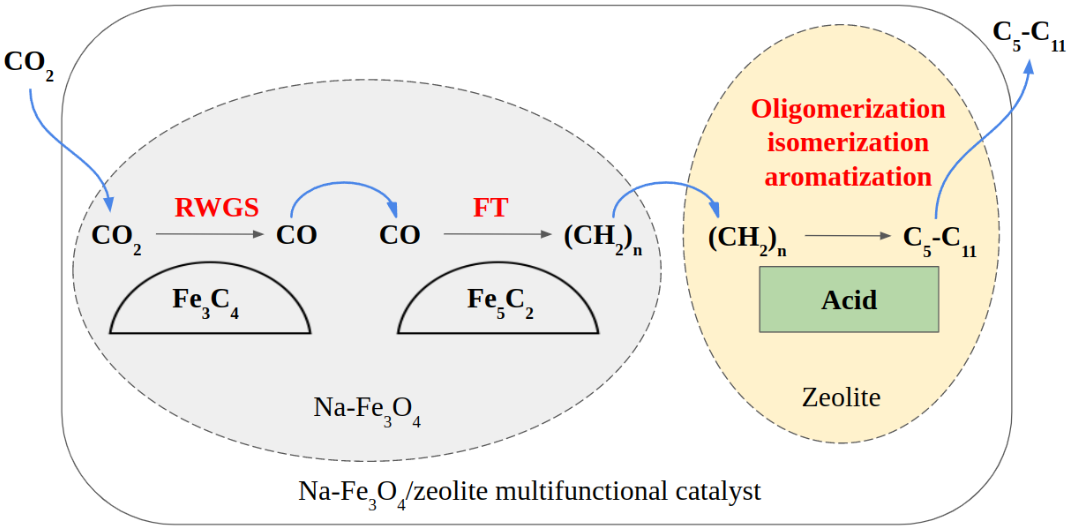
CO2
RWGS
CO2
CO
CO
FT
(CH2)n
Fe3C4
Fe5C2
Na-Fe3O4
Oligomerization
isomerization
aromatization
(CH2)n
C5-C11
Acid
Zeolite
C5-C11
Na-Fe3O4/zeolite multifunctional catalyst

Figure 2.9: Hydrogenation of CO_2 to gasoline range hydrocarbons: reaction scheme. Adapted from [37].

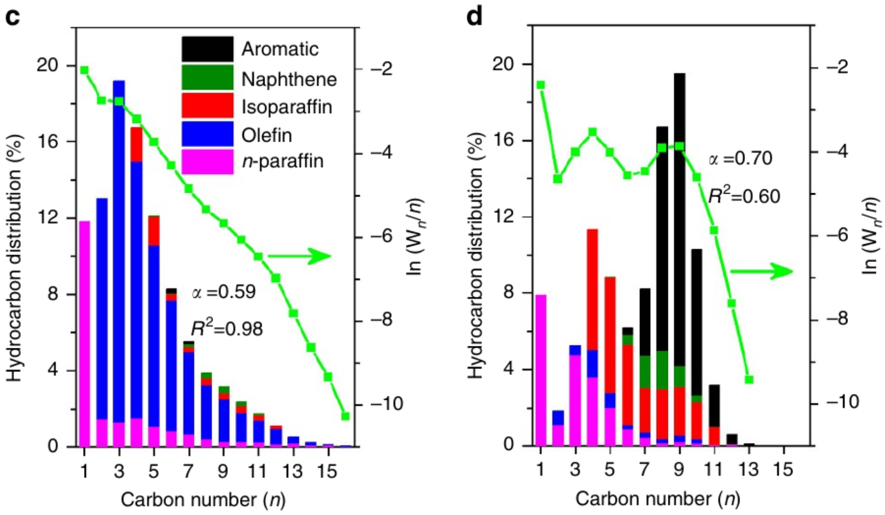

Figure 2.10: Hydrocarbon product distribution on c) Na-Fe_3O_4 and d) Na-Fe_3O_4/HZSM-5. Image from [37].

Following those findings, Cui et al.[49] tested a Na-modified spinel oxide $ZnFeO_x$ catalyst with the addition of a zeolite HZSM-5. They varied the Na content from 0.05 to 20 wt.%, and the $ZnFeO_x$-4.25Na/S-HZSM-5[3] presented the highest aromatics selectivity of 75.6% when compared to all hydrocarbons and a CO_2 conversion of 41.2%. The addition of C-HZSM-5[4] in $ZnFeO_x$-4.25Na the C_{5+} increased from 49.7% to 62.5% and the aromatics selectivity also increased from 1.1% to 29.6%, while C_2-C_4 olefin selectivity decreased from 34.8% to 7.7%. The reaction took place in a fixed-bed reactor with a continuous flow at 320° C, 3 MPa, and a feed ratio of 3:1 (H_2/CO_2). In a similar approach to the Wei et al.[37] work, the figure 2.11 clearly illustrates that zeolite activity has a direct influence on hydrocarbon distribution, especially in aromatics generation.

---

[3] S-HZSM-5 has a cubic shape and is considered the 'standard' nanocrystalline HZSM-5.

[4] C-HZSM-5 is the commercial HZSM-5 and possesses an elongated prismatic shape with smooth surfaces.

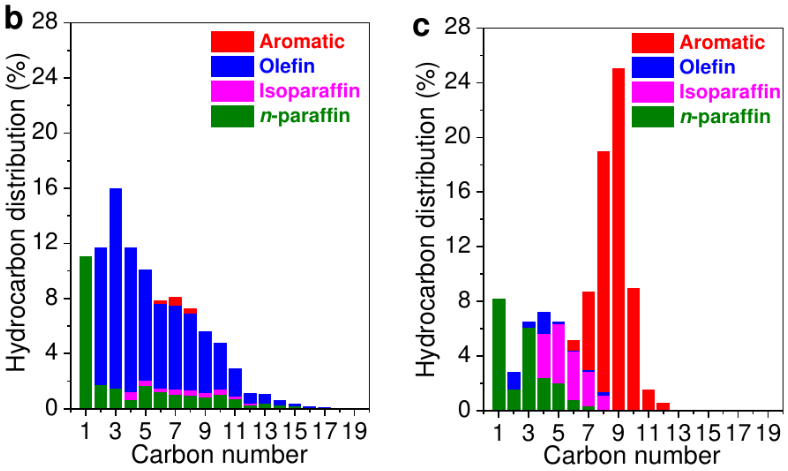

Figure 2.11: Hydrocarbon product distribution on b) $ZnFeO_x$-4.25Na and c) $ZnFeO_x$-4.25Na/S-HZSM-5. Image from [49].

Kahn et al.[24], report a bifunctional $FeAlO_x$ catalyst that directly converts CO_2 into C_{5+} hydrocarbons with an overall selectivity of 77.0% (excluding CO) at a CO_2 conversion of 20.2% (H_2/CO_2=1:1). For a higher ratio of 3:1, 19.7% C_{5+} yield is achieved at 36.8% CO_2 conversion. The presence of surface oxygen vacancies from reduced Fe_3O_4 phase was proposed to enhance the formation of CO via CO_2 through RWGS reaction, C-C coupling is then performed over Hägg iron carbide forming lower olefins. On the surface of the AlO_x phase, lower olefins readsorption was proposed to occur. Also, the AlO_x phase enhances CO_2 and H_2 adsorption which will support the formation of intermediate species more easily and subsequently long-chain linear α-olefins and long-chain hydrocarbons formation via FTS.

Gao et al.[50], achieved a hydrocarbon selectivity of 26.5% and CO selectivity of 73.5% with Fe_2O_3/HZSM-5, where the hydrocarbons distribution is 2% of CH_4, 27.5% of C_2-C_4 and 70.5% of C_{5+} at a CO_2 conversion of 7.1%. The reaction conditions were 340° C, 3MPa and H_2/CO_2 ratio of 3. Gao compared different metal oxide/zeolite composites and the In_2O_3/HZSM-5(2/1) achieved the highest C_{5+} production, with hydrocarbon selectivity of 55.2% where 78.6% are C_{5+} hydrocarbons at a 13.1% conversion of CO_2.

In Kahn's work, the incorporation of a zeolite (HZSM-5) on the catalyst was studied. At a 1:1 H_2/CO_2 ratio, the $FeAlO_x$-5/HZSM-5 composite catalyst presents a conversion of CO_2 and has selectivities for CO, CH_4, and C_{5+} hydrocarbons that are close to those of a single $FeAlO_x$-5[5] catalyst. But with a H_2/CO_2 ratio of 3, the selectivity and yield of C_{5+} increased from 57.8 to 70% and 19.7 to 21.6% when comparing with $FeAlO_x$-5 catalyst. The addition of a zeolite to the $FeAlO_x$-5 catalyst did not considerably boost the C_{5+} yield, in comparison to previously reported catalysts. However, this type of metal oxide/zeolite composite catalyst presented excellent stability and potential for conversion of CO_2 to liquid fuels and chemicals.[24]

Catalyst support modification and the use of promoters, as well as precise mechanistic insights, are popular research topics. Tuning the catalyst (selection of metal, promoter, and support), the used feedstock (available CO_2 and obtaining H_2 from renewable sources), and operating conditions will lead to a more sustainable process and make it more commercially viable.

---

[5] Fe/Al ratio of 5.

2.5 Commercial SAFs

For numerous years, the urgent climate issue has been taken into consideration. Furthermore, air travel is likely to increase. Commercial airlines globally consumed 52 billion gallons of fuel in 2020, and are predicted to consume 60 billion gallons in 2022, representing a 15.4% rise in fuel consumption.[51] Alternative sustainable jet fuels have become both a challenge and a solution. Sustainable Aviation Fuel (SAF) has been utilised in commercial airlines since 2011, but barely amounts to 0.1% of total fuel use (2019[52]). Mainly because it is more expensive than ordinary jet fuel.

KLM was one of the first airlines to adopt SAF, and it has established purchasing agreements with suppliers. As a result, several airlines, including Lufthansa, SAS, Alaska Airlines, and Qantas, have begun to use SAF on commercial flights.[52]

SAF can be made from both biological and non-biological materials. Its feedstock varies, but it mostly comes from cooking oil, plant oils, agricultural residues, and waste (municipal and gases). This fuel may be mixed with ordinary jet fuel, allowing it to be used without requiring any changes to the aircraft's infrastructure. When compared to traditional jet fuel, this fuel emits up to 80% less CO_2 across its entire life cycle.[53] Currently, production of SAFs is less than 150 million litres per year, which compared to jet fuel demand it is less than 0.5%.[18] It is projected that about 450 billion litres of SAF would be required in 2050 to achieve net-zero emissions by 2050, necessitating significant manufacturing of this type of jet fuel.[53]

Neste, World Energy, Alder Fuels, and SkyNRG are just a few of the prominent providers with continuous output. Neste is a worldwide provider with manufacturing plants in North America, Asia, and Europe, and is planning to raise total renewable product production capacity to 5.5 million tons by 2023.

Depending on the feedstock and technological approach employed, biofuels can be produced via oleochemical, thermochemical, biochemical, or hybrid methods. For the time being, the following technologies have been certified to manufacture SAF for commercial use.[54]

- Hydrotreated Esters and Fatty Acids (HEFA)
- Fischer-Tropsch (FT)
- Alcohol to Jet (AtJ)
- synthesised Iso-Paraffins (SIP)
- Catalytic Hydrothermolysis (CHJ)
- Hydroprocessed Hydrocarbons, Esters and Fatty Acids (HC-HEFA)
- Co-processing

Because the HEFA-SPK (hydrotreated esters and fatty acids synthesised paraffinic kerosene) technology is currently fully commercial, biofuel production capacity will be increased by expanding existing facilities and constructing new ones. Neste has HEFA-based plants that produce mostly renewable diesel, with the option of adding bio-jet generation.[18]

By 2025, alcohol-to-jet synthesised paraffinic kerosene (AtJ-SPK), catalytic hydrothermolysis jet (CHJ) and Fischer-Tropsch synthesis of paraffinic kerosene (FT-SPK) (based on gasification), might be one of the potential commercial procedures for bio-jet fuel. Even so, they generate a wide range of fuel products, including bio-jet fuel fraction. The quantity of the bio-jet fraction may be increased by altering the process conditions for each of the technologies, even though the proportion of the jet fraction in the total liquid fuels differs. Thus, at least 15% of the existing low-carbon fuels generated might be bio-jet if HEFA refiners were motivated to manufacture it in addition to renewable diesel. At a reasonable investment cost, this would significantly enhance the quantity of bio-jet fuel that could be made accessible.[18] However, when compared to bio-based fuels, FT-SPK generated using PtL is a technique receiving considerable interest due to its potential to create fuels with extremely low GHG emissions and fewer feedstock restrictions and sustainability difficulties. Since the feedstock consists mostly of power, water, and concentrated CO_2 sources.[55]

The conversion of CO_2 to SAF by SkyNRG in Amsterdam is a real-life example. Construction on the facilities is expected to be completed by 2027, and they will manufacture 50 000 tonnes of SAF every year. It is located near the Port of Amsterdam and will feed the airlines across the airport via an existing pipeline to Schiphol Airport.[56] SkyNRG has KLM Royal Dutch Airlines and SHV Energy has investors for further projects such as SkyNRG Delfzijl (DSL-01), a SAF manufacturing plant that will operate in 2025 and produce 100 000 tonnes of SAF per year.[57] The Boeing Company has also backed a SkyNRG project called SkyNRG Pacific Northwest (PNW), which aims to generate 90,000 tonnes of SAF per year in a US plant by 2027.[58]

Because the goal of bio-jet fuel production and usage is to reduce emissions and mitigate climate change, overall sustainability and lower carbon intensity of the final fuel will be a top concern. As a result, all technologies must be improved, and new ones must be created. As the need for bio-jet fuel grows, so does the demand for facilities to create it.

Chapter 3

Methods

This chapter focuses on the several methods employed in this thesis. Density Functional Theory (DFT) is the main quantum chemical method employed to calculate adsorption energies for gas phase molecules (CO, CO_2, H_2, O_2, etc.) on cobalt and iron carbides surfaces, and is also used to obtain thermodynamic and kinetic parameters for the elementary reaction steps in the RWGS and FT reaction mechanism.

In this chapter, DFT is briefly introduced in Section 3.1. The catalysts models used are presented in Section 3.2. VASP simulations are discussed in Section 3.3, explaining convergence tests, geometry optimisation, molecular vibrations, and transition state calculations. In Section 3.3.5, the methods to obtain adsorption energies, chemical potentials, surface energies, and thermodynamic calculations are explained. Lastly, in Section 3.4, the microkinetic modelling (MKM) calculations are briefly explained.

3.1 Density Functional Theory

Density Functional Theory (DFT) is a computational quantum mechanical modelling tool used to examine the electronic structure of many-body systems. The Schrödinger equation (eq.3.1) considers all the information to predict the behaviour of a system (molecules and atoms).[34][59]

$$\left[\frac{-\hbar^2}{2m}\sum_{i=1}^{N}\nabla_i^2 + \sum_{i=1}^{N}V(r_i) + \sum_{i=1}^{N}\sum_{j<1}U(r_i, r_j)\right]\psi = E\psi \tag{3.1}$$

The equation 3.1 represents the Schrödinger equation time independent for N electron system. The electron mass is m and $\hbar$ is the Planck constant reduced. The first term between brackets is the kinetic energy and the second and third term are potential energies. Where the second term includes interactions between electrons and nuclei and the third term interactions between different electrons. The Hamiltonian operator is defined by all terms in the brackets. The wave function is represented by ψ and E is the ground state energy of the electrons.[34][59]

Schrödinger's wave function contains all of the information available about a system. However, if the number of electrons in the systems is too high the solution of the equation requires a lot of work, limiting this method to a small N, number of electrons. Therefore, a huge and extended solid system cannot be solved using the wave function approach.[59]

Hohenberg and Kohn presented a solution for this problem. Hohenberg and Kohn theorems state:[60]

Theorem 1. *The ground state density $\rho(r)$ determines the external potential energy $v(r)$ to within a trivial additive constant.*

Theorem 2. *The ground state density $\rho(r)$ can be determined from the ground state energy functional $E[\rho]$ via the variational principle by variation only of the density.*

Kohn and Sham developed self-consistent single-particle equations known as KS equations. Which makes a real interacting many-body system of electrons to be calculated as a system of non-interacting electrons with all the interaction related effects present in an exchange-correlation potential.[59][61]

Therefore, DFT is based on various approximations and approaches, such as Hohenberg–Kohn theorems, Kohn–Sham approach, Local Density approximation (LDA) and Generalised Gradient approximation (GGA). However, treating the electron exchange and correlation in the system requires a suitable exchange-correlation functional.[61][62]

Several software packages are available to perform DFT calculations, such as Quantum Espresso, Siesta or VASP, etc. VASP is the package used for the DFT calculations in this thesis. Using plane wave basis sets, VASP solves by iteration the Kohn–Sham equations of local density or spin–density functional theory. The interactions between electrons and ions are described using the projector-augmented wave (PAW) approach. Iterative matrix-diagonalisation techniques like the blocked Davidson scheme, residual minimisation scheme, and direct inversion in the iterative subspace (RMM-DIIS) can be used to calculate the electronic ground-state energy. The charge density is reevaluated after each repetition. An updated Pulay mixing strategy is used to combine the new density with the input charge density from the previous iteration cycle in order to attain numerical stability. Further information can be acquired in VASP manual [63].[34]

To perform DFT calculations with VASP, a High-Performance Computing (HPC) cluster was used from HPC-UGent Tier-2, nicknamed "doduo" and also another nicknamed "victini", in order to submit simulations.[64]

3.2 Catalyst Modelling

3.2.1 Cobalt

The bulk and surface structure of cobalt-based catalyst was made using a python script with the Atomic Simulation Environment (ASE) module, which generates a POSCAR. This input file for VASP simulations contains all geometrical information about the structure.[65] Three cobalt bulk structures were studied (figure 3.1); (a) the FCC cubic with a lattice value of a = 3.5 Å, (b) the FCC orthorhombic with lattice a = b = 2.48 Å, and c = 3.5 Å, and (c) HCP orthorhombic with lattice values a = 3.5 Å, b = 6.06 Å, and c = 5.68 Å. The bulk structures were optimised later (see chapter 4), resulting in slightly different lattice constants depending on the exchange functional. The optimised bulk structure was then used to create a cobalt surface. A 3-layer FCC Co(111) slab was used as the model surface in this study. In Chapter 4 the modelled slab was tested for a different amount of layers and amount of fixed layers. The slab surface has 3 layers and the bottom layer was fixed at the bulk positions with an optimised lattice constant of 3.5618 Å. To prevent erroneous interactions between nearby system projections, a 15 Å vacuum layer was placed perpendicular to the surface.

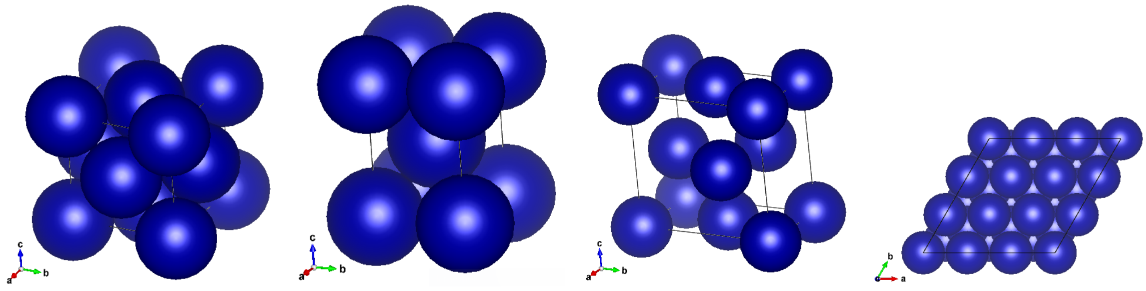

(a) FCC Cubic (b) FCC Orthorhombic (c) HCP Orthorhombic (d) fcc (111) surface

Figure 3.1: Cobalt structures studied: (a), (b) and (c) bulk structures and (d) surface (111) from FCC bulk structure.

3.2.2 Iron Carbides

There are several structures and compositions for iron carbides, in this thesis the iron carbides studied were χ-Fe$_5$C$_2$ monoclinic[1] (C2/c)[2], ϵ-Fe$_3$C hexagonal[1] (P6$_3$22)[2], η-Fe$_2$C orthorhombic[1] (Pnnm)[2] and θ-Fe$_3$C orthorhombic (Pnma)[2] (see figure 5.1).[66]

For each bulk structure, several slab surfaces were made respecting the Miller Index (h k l). Each slab constructed has a vacuum spacing between repeating slabs of 15Å. For the χ-Fe$_5$C$_2$ bulk structure the considered surfaces were $(010)_{0.25}$, $(510)_{0.0}$, $(11\bar{1})_{0.0}$, $(11\bar{1})_{0.5}$, $(100)_{0.0}$ and $(100)_{0.287}$ [3]. The ϵ-Fe$_3$C surfaces studied are $(001)_{0.0}$, $(011)_{0.0}$ and $(101)_{0.0}$. For η-Fe$_2$C, $(001)_{0.0}$, $(011)_{0.0}$, $(100)_{0.0}$, $(101)_{0.0}$ and $(110)_{0.0}$ are considered. And for θ-Fe$_3$C the surfaces are $(010)_{0.0}$, $(101)_{0.0}$, $(110)_{0.0}$, $(111)_{0.0}$ and $(0\bar{1}1)_{0.0}$.

---

[1] Unit cell.

[2] Space group.

[3] The subscript stands for the fractional distance of the bulk unit cell where the surface was cleaved from the origin (see figure 3.2)

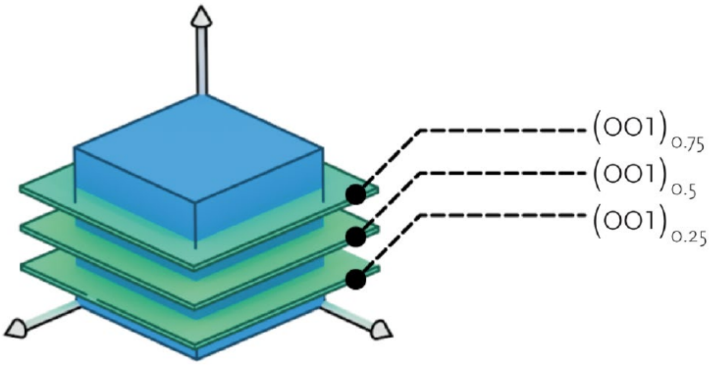

Figure 3.2: Unit cell representation with surface notation. Image from [67].

The surfaces were cut from the bulk structure either from the origin or as the figure 3.2 shows, from a different fraction of the bulk structure unit cell. The surfaces can be either stoichiometric or non-stoichiometric. If a surface is stoichiometric, it has the same Fe/C ratio as the bulk structure. When it is non-stoichiometric, the surface has a different Fe/C ratio than the bulk structure. As figure 3.3 shows, the symmetric slabs have the same surface on the top and the bottom of the slab. The asymmetric surfaces can have more or fewer carbon atoms on one of the surfaces.

Symmetric slab surfaces were intended since it gives a correct surface energy. If a surface is asymmetric the energy will be the average of the top and bottom surface energies. If a surface is non-stoichiometric to the bulk structure the carbon chemical potential needs to be taken into account in the surface energy equation to balance the carbon content. Those scenarios were considered symmetric and stoichiometric, symmetric and non-stoichiometric, and asymmetric and stoichiometric slabs. The method of calculation of surface energies is available in 3.3.5. Table 3.2 has detailed information on each stoichiometric slab. The figures A.1, A.3, A.4 and A.5 help visualise the slab surfaces constructed, in Appendix A.

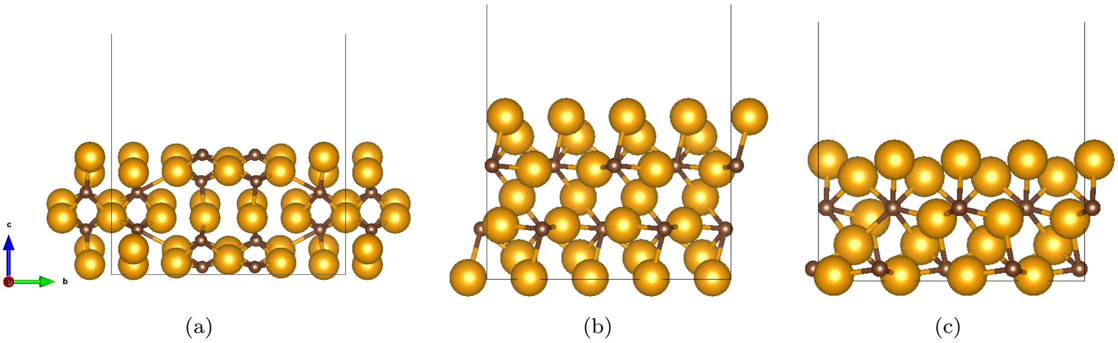

(a) (b) (c)

Figure 3.3: Different slab surfaces: (a) $\chi(010)_{0.25}$ symmetric and stoichiometric, $\chi(100)_{0.287}$: (b) symmetric and non-stoichiometric, and (c) asymmetric and stoichiometric.

3.3 VASP simulations

DFT calculations require an exchange-correlation functional as stated before. In VASP there are several functionals available, among them PBE, VdW-DF and SCAN+rVV10 were used.

- PBE - The PBE functional form was built using a numerical GGA, which satisfied known precise hole restrictions by building a model of the exchange-correlation hole.[68]

- VdW-DF - The semi-local exchange-correlation functional is supplemented by a nonlocal correlation functional that approximately captures dispersion interactions.[69]
- SCAN+rVV10 - is a hybrid functional and the only Van der Waals density functional to date that produces outstanding interlayer binding energies and spacings as well as intralayer lattice constants in 28 layered materials.[70]

In VASP simulations several input files are required, such as POSCAR, POTCAR, INCAR and k-points. A jobscript is used to specify the required nodes, VASP module, name of simulation, wall time and run command which runs the simulations. Also for Van der Waals required calculations, a vdw_kernel file must be added.

3.3.1 Convergence Tests

Convergence tests were performed in bulk structures and slabs. The convergence was tracked using the total energy of the system. To achieve more accurate results, simulation parameters were tested in the first stage. Those parameters are cut-off energy, k-points and smearing. For the cut-off energy, the tag ENCUT was varied, typically ranging from 200-600 eV. Higher values are better but are computationally more expensive. The convergence criterion was set to 2 meV/atom. This was also done for the number of k-points (file KPOINTS), and the smearing width (tag SIGMA). In general, it is preferred to use more k-points along smaller lattice constants, this has to do with reciprocal space. For smearing width, lower values frequently produce superior numerical precision depending on the smearing scheme (ISMEAR) but may come at the price of a more challenging convergence of the self-consistent field. The ISMEAR was set at 2 for Methfessel-Paxton order 2. Figure 3.4 shows the graphs of ENCUT and k-points convergence. In the appendix A more info on the results of convergence tests can be found.

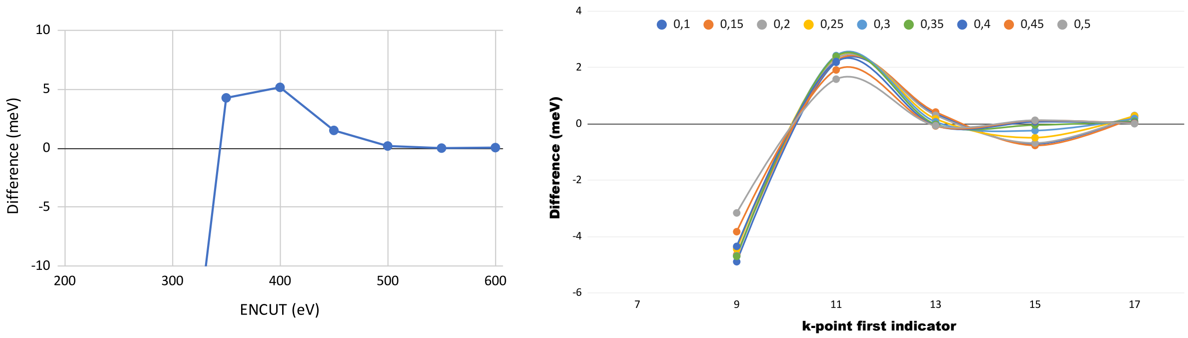

(a) Cut-off energy convergence

(b) k-points convergence for several smearing values

Figure 3.4: Test convergence of FCC cubic cobalt bulk structure.

for the cobalt slab fcc (111), the number of layers and the number of fixed layers were also tested. Using the VdW-DF functional, a 3×3×3 Monkhorst–Pack k-point grid, a plane–wave basis set with a cut–off kinetic energy of 450 eV and a smearing width of 0.2 eV, the number of layers was varied between 3 to 5, and the number of fixed layers between 1 and 3.

3.3.2 Geometry Optimisation

Geometry optimisation was performed for gas phase molecules and bulk structures. For gas phase molecules, by using a cubic unit cell with dimensions of 15Å by 15Å by 15Å, the interactions between repeating unit cells (i.e., neighbouring molecules) were limited to a minimum. A plane–wave basis set was used with a cut–off kinetic energy of 450 eV. The Brillouin zone for the calculation of gas phase molecules was represented by the gamma point. For these calculations, PBE and VdW-DF functionals were used. Geometries were optimised until a change in energy of less than 0.01 eV/Åoccurred between consecutive steps.

Cobalt bulk phases were also optimised and the parameter optimisation can be found in table 3.1. The Brillouin zone was always sampled using a Monkhorst–Pack grid. The iron carbide bulk structures were optimised using three different functionals, PBE, VdW-DF and SCAN-rVV10, and a plane–wave basis set with a cut–off kinetic energy of 500 eV. The smearing width for χ-Fe$_5$C$_2$, ϵ-Fe$_3$C and η-Fe$_2$C structures was 0.05 eV. As for the bulk θ-Fe$_3$C the smearing width used was 0.2 eV. The k-points used for the bulk structures and slab surfaces are in table 3.2. The grids used were Monkhorst–Pack for χ-Fe$_5$C$_2$, η-Fe$_2$C and θ-Fe$_3$C, but for ϵ-Fe$_3$C a gamma centred mesh was used. Iron carbide slabs were optimised using a plane–wave basis set with a cut–off kinetic energy of 450 eV and a smearing width of 0.2 eV. The number of k-points used is in table 3.2 and it used Monkhorst–Pack grids.

Another way to optimise and better visualise the structure and the volume of the unit cell is through the Murnaghan equation-of-state (3.2). Murnaghan's equation-of-state was based on the assumption that the bulk modulus of a solid compressed to a finite strain would behave linearly with respect to pressure.[71]

$$P(V) = \frac{B_0}{B_0'}\left[\left(\frac{V_0}{V}\right)^{B_0'} - 1\right] \tag{3.2}$$

The unit cell multiplier in the POSCAR file varied (expanding and compressing the unit cell) in order to simulate the energies (E0 in eV) for several volumes. Once the output is a file with the unit cell multiplier and energies E0, the volume is calculated knowing the lattice constants. By fitting the volumes and energies to the Murnaghan equation-of-state, the bulk modulus (B_0) and the optimal volume (V_0) can be predicted.

Table 3.1: Parameters used for cobalt structures VASP calculations.

	ENCUT (eV)	k-pointS	SIGMA
FCC-C	450	11×11×11	0.2
FCC-O	500	15×15×15	0.2
HCP-O	500	15×15×15	0.25
fcc (111)	450	3×3×1	0.2

Table 3.2: Parameters and characteristics of iron carbide slab surfaces for each bulk structure.

	Fe	C	a	b	c	γ(°)	k-points	n[†]	Thick.(Å)[‡]
χ-Fe$_5$C$_2$	20	8	11.59	4.49	4.93		6×6×4	1	
$(100)_{0.0}$[*]	40	16	8.99	9.95	19.61	90.00	6×6×1	2	4.61
$(100)_{0.287}$[*]	40	16	8.99	9.95	19.58	90.00	6×6×1	2	4.58
$(010)_{0.25}$	60	24	9.95	11.49	21.16	97.53	6×6×1	3	6.16
$(11\bar{1})_{0.0}$	40	16	13.41	11.72	17.62	77.65	6×6×1	2	2.62
$(11\bar{1})_{0.5}$	40	16	13.41	11.72	18.17	77.65	6×6×1	2	3.17
$(510)_{0.0}$	80	32	9.95	25.28	18.60	93.45	4×2×1	4	3.60
ϵ-Fe$_3$C	6	2	4.66	4.04	4.32		6×6×6	1	
$(001)_{0.0}$[*]	48	16	9.32	8.07	22.56	120.00	4×4×1	8	7.56
$(011)_{0.0}$[*]	48	16	9.32	11.83	20.65	111.51	6×6×1	8	5.65
$(101)_{0.0}$[*]	48	16	12.71	8.67	20.37	111.51	6×6×1	8	5.37
η-Fe$_2$C	4	2	2.82	4.28	4.71		8×6×6	1	
$(001)_{0.0}$[*]	64	32	11.29	8.56	23.70	90.00	4×4×1	16	8.70
$(011)_{0.0}$[*]	64	32	11.29	12.74	21.02	90.00	6×6×1	16	6.02
$(100)_{0.0}$	40	20	8.56	9.43	20.65	90.00	4×4×1	10	5.65
$(101)_{0.0}$[*]	32	16	10.99	8.56	19.01	90.00	4×4×1	8	4.01
$(110)_{0.0}$[*]	32	16	9.43	10.26	19.13	90.00	6×6×1	8	4.13
θ-Fe$_3$C	12	4	4.47	5.02	6.73		6×4×4	1	
$(010)_{0.0}$	36	12	6.79	9.10	22.27	90.00	4×2×1	3	7.27
$(101)_{0.0}$	48	16	8.18	10.17	21.92	90.00	6×4×1	4	6.92
$(110)_{0.0}$	48	16	13.58	13.65	17.51	90.00	4×4×1	4	2.51
$(111)_{0.0}$	48	16	13.65	15.18	17.65	68.20	4×2×1	4	2.65
$(0\bar{1}1)_{0.0}$	48	16	9.10	8.49	22.27	90.00	6×6×1	4	7.27

3.3.3 Vibrational Frequencies

The application of electronic structure calculations for the estimation of harmonic frequencies has been useful for the understanding of complicated experimental spectra. In addition, harmonic frequencies are a key component of statistical thermodynamics, which are used to derive and predict thermochemical and kinetic data.[72]

VASP can predict these harmonic frequencies using vibrational calculations. By changing the IBRION tag value to 5 or 6, the Hessian matrix is calculated using finite differences. The 5 value is used, which means that all non-constrained atoms are displaced. [62] The number of displacements per direction

---

[*] Asymmetric and stoichiometric slab surfaces.

[†] n is a multiplier integer of how much the slab is larger than the conventional cell bulk.

[‡] Slab thickness.

(NFREE) was not specified, the default value is 2. For POTIM was used a value of 0.015 Å, which is the size of displacement.[59]

The Hessian matrix is a $3N \times 3N$ matrix, with N being the number of atoms. The $3N$ eigenvalues of this matrix subsequently provide the $3N$ normal mode frequencies. For gas molecules, the number of vibrational modes is $3N - 5$ for a linear molecule and $3N - 6$ for a non-linear molecule. The total modes are $3N$, so besides the vibrational modes, gas molecules have 3 translational and 3 (for non-linear molecules) or 2 (for linear molecules) rotational modes.[59]

The vibrational frequencies for an adsorbed molecule on a surface are calculated similarly as stated, but all the slab atoms (i.e., cobalt atoms) must be fixed in the POSCAR file.

Figure 3.5 illustrates the possible vibrations in a gas phase molecule. As for adsorbed molecules on a surface, since they lose their rotational and translational modes they gain more vibrational modes. The possible vibrational modes are represented in figure 3.6.

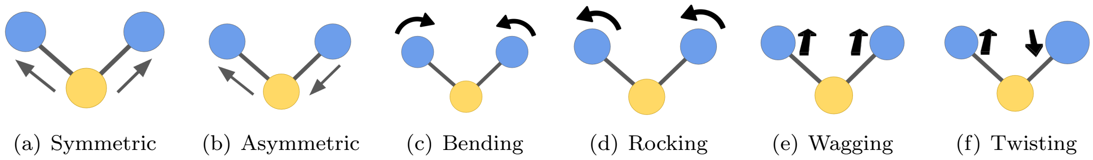
(a) Symmetric (b) Asymmetric (c) Bending (d) Rocking (e) Wagging (f) Twisting

Figure 3.5: Vibrational modes of a gas phase molecule. Adapted from [34].

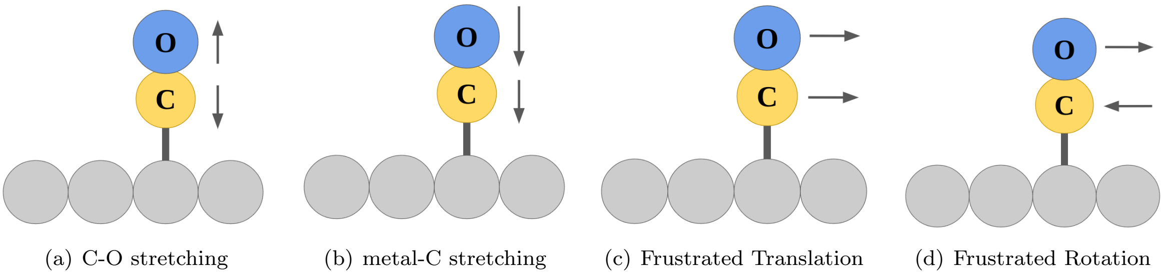

(a) C-O stretching (b) metal-C stretching (c) Frustrated Translation (d) Frustrated Rotation

Figure 3.6: Vibrational modes of an adsorbed molecule on a surface. Adapted from [34].

3.3.4 Transition State

A certain configuration along the reaction coordinate constitutes the transition state (TS) of a chemical reaction. The condition corresponding to the maximum potential energy along this reaction coordinate is what is meant by this term. Understanding the kinetics of a chemical reaction requires the localisation of the transition state. The method used was the Nudge Elastic Band with the climbing image activated and if necessary the dimer method was used after the cNEB calculation.[34]

NEB has the objective of defining the minimum energy path (MEP)between two local minima and finding saddle points. A saddle point is a minimum for all directions except for the reaction pathway. The method requires several intermediate images along the reaction path. It optimises those images finding the lowest energy of every image and the spacing between images remains the same.[73]

As the image shows, there is a difference between the NEB and cNEB methods, where LCLIMB=FALSE and LCLIMB=TRUE (with climbing image method activated) in the INCAR file, respectively. The NEB approach is somewhat modified by the climbing image, which drives the highest energy image up to the saddle point.[73]

The NEB calculations were performed with 5 or 8 intermediate images, depending on the reactions and the difficulty to find the transition state. The nebmake.pl script from [73] was used to generate the POSCARs of the intermediate images. The calculations were performed with the VdW-DF functional, a cut-off energy of 450 eV, a smearing width of 0.2 eV, and the Brillouin zone was sampled with a (3×3×1) Monkhorst-Pack grid. When cNEB was used POTIM[4]=0.015 and IBRION[5]=1 were used. The low POTIM resulted in a slow convergence towards the TS, but it resulted in a higher success rate for finding the TS. When POTIM was increased to 0.5, the TS can be found faster, but calculations often exploded (i.e., abnormal increase in energies).[73]

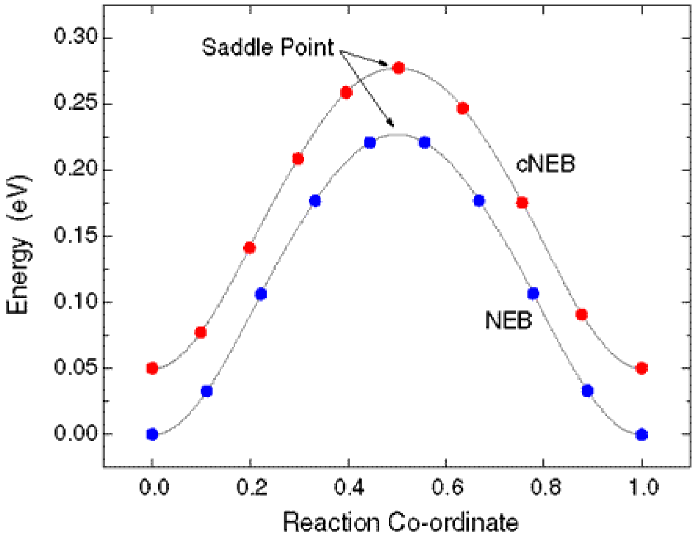

Figure 3.7: Representation of the differences of NEB and cNEB methods. Image from [73].

After the cNEB method, the dimer method can be used to further refine the TS. For example, when the structure found in the NEB calculations is not yet a TS but very close to one the dimer method can be employed to find the exact TS. To start the dimer method calculation, several scripts from VTST were used, to generate automatically initial files, such as a POSCAR file at the interpolated saddle point and a MODECAR file providing the starting direction that passes through the NEB supposed saddle point. For a dimer calculation, some tags should be changed, such as IBRION=3, POTIM=0.0, IOPT=2 and ICHAIN=2.[73]

The vibrational frequencies of the saddle point have one imaginary value, corresponding to the reaction pathway. These frequencies were calculated following the same principle as described in section 3.3.3.

---

[4] Ionic step size scaling.

[5] Defines the method for updating and moving the ions.

3.3.5 Result Analysis methods

Adsorption Energy

The adsorption energy of an adsorbate species, e.g CO, on a metal surface may be estimated using equation 3.3.[34][74][75]

$$E_{adsorption} = E_{system} - E_{slab} - E_{adsorbate} \tag{3.3}$$

Where E_{system} is the energy of the system slab+adsorbate, the E_{slab} is the energy of the slab and the $E_{adsorbate}$ is the energy of the adsorbate in the gas phase. All these energies are obtained from the VASP calculation of the optimised structures. The energy of adsorption is represented with $E_{adsorption}$, and it was converted to kJ/mol because VASP is in eV.

The energy of a single atom adsorbate for the adsorption on $\chi(510)_{0.0}$ was calculated as it was obtained from a reaction, e.g. carbon atom electronic energy is obtained from CO dissociation in C and O, so E_C=E_{CO}-E_O. The oxygen atom's electronic energy was obtained from H_2O dissociation and the hydrogen atom's electronic energy from H_2. The OH energy was calculated from H_2O dissociation in OH and H. Their energy is in table A.1.

The active sites for Co(111) and χ-Fe_5C_2(510) slab surface are represented in figure 3.8.

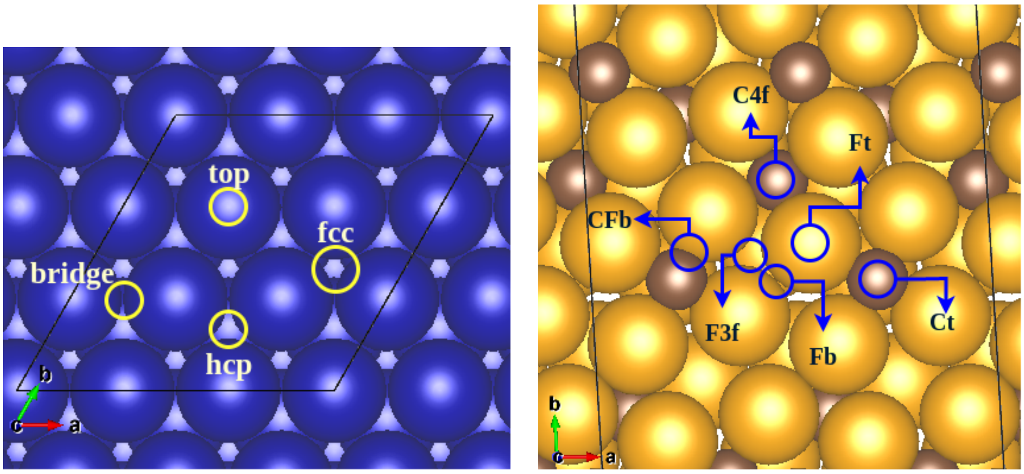

(a) Co(111) sites (b) χ-Fe_5C_2(510) sites

Figure 3.8: Co(111) χ-Fe_5C_2(510) and active sites used for molecules adsorption.

Cohesive and Formation Energy

The cohesive energy (E_{coh}) of an iron carbide bulk structure was calculated with equation 3.4.

$$E_{coh} = \frac{N_{Fe}E_{Fe}^{gas} + N_C E_C^{gas} - E_b}{N_{Fe} + N_C} \tag{3.4}$$

The E_b is the electronic energy of the bulk structure, and the N_{Fe} and N_C are the amount of Fe and C atoms, respectively. The E_{Fe}^{gas} is the electronic energy of a single Fe atom in the gas phase, and E_C^{gas} is the electronic energy of a single carbon atom in the gas phase.

The formation energy (E_{form}) was calculated from the equation 3.5, where the μ_C is the chemical potential of carbon. The E_{Fe}^{gs} is the electronic energy of a single Fe atom in the BCC bulk structure (ground state).

$$E_{form} = \frac{E_{bulk} - N_{Fe}E_{Fe}^{gs} - N_C\mu_C}{N_{Fe} + N_C} \tag{3.5}$$

Surface Energy

The surface energy for the iron carbide surfaces was calculated using one of the two following equations. When a surface is stoichiometric, equation 3.7 is used. When it is non-stoichiometric, equation 3.6 is used, which includes the chemical potential of carbon. Preferably symmetric surfaces are used to accurately represent the surface energy. When asymmetric surfaces are used this is mentioned.

$$E_{surf.}^{non-stoich.} = \frac{E_{slab}(Fe_xC_y) - n \times E_b(Fe_aC_b) - (y - x/(a/b)) \times \mu_C}{2A} \tag{3.6}$$

$$E_{surf.}^{stoich.} = \frac{E_{slab}(Fe_xC_y) - n \times E_b(Fe_aC_b)}{2A} \tag{3.7}$$

The surface energy calculated is $E_{surf.}$ (J/m^2), either $E_{surf.}^{stoich.}$ for stoichiometric surfaces and $E_{surf.}^{non-stoich.}$ for non-stoichiometric surfaces. The $E_{slab}(Fe_xC_y)$, refers to the total slab electronic energy of Fe_xC_y (in eV), where contains n times the amount of bulk unit cells. The bulk electronic energy of Fe_aC_b is $E_b(Fe_aC_b)$, and a/b is the Fe/C ratio of the bulk structure. The area of the surface (A) has units m^2 and the μ_C is the carbon chemical potential (eV). The calculation for the non-stoichiometric surfaces accounts for the carbon contribution in the surface energy, including the difference between carbon atoms on the slab and on the bulk structure multiplying that difference with the carbon chemical potential.

Wulff Particle

The Wulff construction is an estimation of the equilibrium crystal shape of a crystallite. The Wulff construction can be performed via a Python package named WulffPack[76], in which the input needed are surface energies of the different facets which are direction dependent.[77] Using this package various Wulff constructions were made.

Thermodynamic Calculations

The Gibbs free energy (ΔG) of gas phase molecules (e.g. CO, CO_2, H_2O, CH_4, CH_2O, CH_3OH) were calculated from electronic energies, the zero–point energies (ZPE), enthalpy (H) corrections, and entropies (S). The vibrational frequencies and electronic energy are calculated via VASP. The ZPE, enthalpy corrections and entropy are calculated through an excel file with partition functions.

$$ZPE = \frac{1}{2}\sum_{i=1}^{n} hv_i \tag{3.8}$$

For gas phase molecules the enthalpy and entropy were calculated by summing the rotational, translational and vibrational partition functions.

$$H_{linear} = RT + \frac{5}{2}RT + RT\sum_i \left(\frac{hv_i}{kT}\right)\frac{e^{\frac{-hv_i}{kT}}}{1 - e^{\frac{-hv_i}{kT}}} \tag{3.9}$$

$$H_{non-linear} = \frac{3}{2}RT + \frac{5}{2}RT + RT\sum_i \left(\frac{hv_i}{kT}\right)\frac{e^{\frac{-hv_i}{kT}}}{1 - e^{\frac{-hv_i}{kT}}} \tag{3.10}$$

$$\begin{aligned} S_{linear} = \; & R\Big(ln\Big(\tfrac{8\pi^2 ABCkT}{\sigma h^2}\Big) + 1\Big) + \textstyle\sum_i R\Big(\tfrac{3}{2}ln\Big(\tfrac{2\pi m}{h^2}\Big) + \tfrac{5}{2}ln(kT) - ln(p) + \tfrac{5}{2}\Big) + \\ & \textstyle\sum_i Rln(1 - e^{\frac{-hv_i}{kT}}) + \Big(\tfrac{Rhv_i}{kT}\Big) \times \tfrac{e^{\frac{-hv_i}{kT}}}{1 - e^{\frac{-hv_i}{kT}}} \end{aligned} \tag{3.11}$$

$$\begin{aligned} S_{non-linear} = \; & R\Big(ln\Big(\tfrac{8\pi^2}{\sigma}\Big) + \tfrac{3}{2}ln\Big(\tfrac{2\pi kT}{h^2}\Big) + \tfrac{1}{2}ln(ABC) + \tfrac{3}{2}\Big) + \\ & \textstyle\sum_i R\Big(\tfrac{3}{2}ln\Big(\tfrac{2\pi m}{h^2}\Big) + \tfrac{5}{2}ln(kT) - ln(p) + \tfrac{5}{2}\Big) + \\ & \textstyle\sum_i Rln(1 - e^{\frac{-hv_i}{kT}}) + \Big(\tfrac{Rhv_i}{kT}\Big) \times \tfrac{e^{\frac{-hv_i}{kT}}}{1 - e^{\frac{-hv_i}{kT}}} \end{aligned} \tag{3.12}$$

For an adsorbed species the vibrational partition function is considered to calculate the enthalpy and entropy. In order to correct the enthalpy the equation 3.15 is used for all enthalpy calculated.

$$H_{ads} = RT\sum_i \left(\frac{hv_i}{kT}\right)\frac{e^{\frac{-hv_i}{kT}}}{1 - e^{\frac{-hv_i}{kT}}} \tag{3.13}$$

$$S_{ads} = \sum_i Rln(1 - e^{\frac{-hv_i}{kT}}) + \Big(\frac{Rhv_i}{kT}\Big) \times \frac{e^{\frac{-hv_i}{kT}}}{1 - e^{\frac{-hv_i}{kT}}} \tag{3.14}$$

$$H_{corr} = H + E0 + ZPE \tag{3.15}$$

Where σ is the symmetry number, ABC are the products of inertial moments (gm*cm^2), m is the molecular mass (kg/mol), p is the pressure (Pa) and v_i is the vibrational frequency of species in s^{-1}. The $k = 1.381 \times 10^{-23}$ m^{2}kg/(s^{2}K) is the Boltzmann constant, $h = 6.626 \times 10^{-34}$ m^{2}kg/s is Planck's constant and $R = 8.314$ J/(molK) is the gas constant.

The formation enthalpy (ΔH_f), entropy variation (ΔS) and the Gibbs free energy (ΔG_f) were calculated for a gas molecule without carbon atoms as example 1 explains, and for molecules with carbon atom were calculated as example 2.

Example 1. The formation of water (H_2O) follows the reaction 3.16.

$$H_2 + \frac{1}{2}O_2 \longrightarrow H_2O \tag{3.16}$$

The formation enthalpy was calculated from the equation 3.17 and the entropy of reaction from the equation 3.18, where the corrected enthalpy and entropy were calculated as previously stated. The Gibbs free energy was obtained from the equation 3.19.

$$\Delta H_f(H_2O,T) = H_{corr}(H_2,T) + \frac{1}{2}H_{corr}(O_2,T) - H_{corr}(H_2O,T) \tag{3.17}$$

$$\Delta S_f(H_2O,T) = S(H_2,T) + \frac{1}{2}S(O_2,T) - S(H_2O,T) \tag{3.18}$$

$$\Delta G_f(H_2O,T) = \Delta H_f(H_2O,T) - T \times \Delta S_f(H_2O,T) \tag{3.19}$$

Example 2. The carbon monoxide (CO) formation follows the reaction 3.20.

$$C + O \longrightarrow CO \tag{3.20}$$

The formation enthalpy was calculated from the equation 3.21 and the entropy of reaction from the equation 3.22. The Gibbs free energy was obtained from the equation 3.19. Where the ΔH_{exp} and S_{exp} for the species needed are from NIST WebBook[78].

$$\Delta H_f(CO,T) = \Delta H_{exp}(C,T) + \Delta H_{exp}(O,T) - (E0(O) + E0(C) - H_{corr}(CO,T)) \tag{3.21}$$

$$\Delta S_f(CO,T) = S(CO,T) - S_{exp}(C,T) - \frac{1}{2}S_{exp}(O_2,T) \tag{3.22}$$

The **chemical potential** (μ_i) of a species (i) is the energy that may be absorbed or released when the particle number of the given species changes. The chemical potential is the partial molar Gibbs free energy (equation 3.23). Here, $\Delta G(i,T)$ is calculated following the same principle as in the **Examples**. The p_0 is the reference pressure and p_i is the partial pressure of the respective species in the feed. p_i is proportional to N which is the molar amount of the species.

$$\mu_i = \left(\frac{\delta G}{\delta N_i}\right)_{T,P,N_{j\neq i}} = \Delta G(i,T) + RTln\left(\frac{p_i}{p_0}\right) \tag{3.23}$$

The carbon chemical potential varies depending on the atmosphere and with that obtains different values. The C in the catalyst is handled at thermodynamic equilibrium with the mixture of reactant and product (e.g., CO, H_2, C_2H_4, and H_2O) under FTS conditions, from which the μ_C may be deduced. So μ_C can be defined in a range with a maximum value from the reactant-catalyst equilibrium in equation 3.26, and a minimum value from product-catalyst equilibrium in equation 3.27.[79] Where $E0_C$ is the electronic energy for a carbon atom in a large unit cell. The other chemical potentials were calculated from 3.23.

$$CO + H_2 \longrightarrow C + H_2O \tag{3.24}$$

$$\frac{1}{2}C_2H_4 \longrightarrow C + H_2 \tag{3.25}$$

$$\mu_C^{max} = \mu_{CO} + \mu_{H_2} - \mu_{H_2O} - E0_C \tag{3.26}$$

$$\mu_C^{min} = \frac{1}{2}\mu_{C_2H_4} - \mu_{H_2} - E0_C \tag{3.27}$$

For typical FT conditions, the temperature is 523 K and the partial pressure of the gas phase of CO, H_2, H_2O and C_2H_4 are 0.83 MPa, 1.67 MPa, 0.09 MPa and 0.3 MPa, respectively. The p_0 was 0.1 MPa. The respective chemical potential calculated with PBE for the carbon atom is -7.56 eV (following the reaction 3.25) and -6.65 eV (following the reaction 3.24). The DFT values from Liu et al.[79] with PBE were -7.45 to -6.60 eV also from equations 3.25 and 3.24.

The chemical potential has a strong relation with the partial pressure of each specie, total pressure, feed ratio and temperature. Zhao et al. found that CO gas partial pressure and H_2/CO ratio have a higher effect on surface energy (surfaces of $\chi - Fe_5C_2$) than temperature.[80] Typically, the carbon chemical potential decreases slightly with the increase of temperature, and it also decreases with the increase of total pressure.[81][80] In this work, the chemical potential of carbon was calculated with equations 3.26 and 3.27, with makes it dependent on the partial pressures of the species used, the temperature and the total pressure. The relation of carbon chemical potential with the CO partial pressure is visible in figure 3.9, which increases with the increase of CO partial pressure.

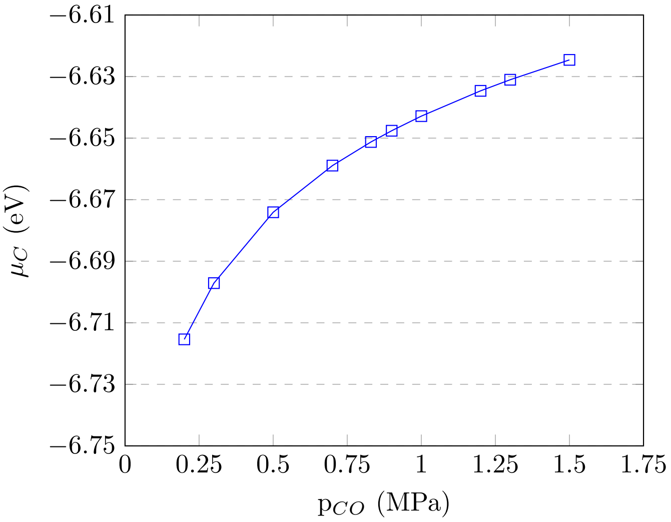

Figure 3.9: Carbon chemical potential relation with CO partial pressure, at 523K and 0.1 MPa.

3.4 Microkinetic Modelling

Microkinetic modelling requires a basic understanding of transition state theory. The surface coverages of all adsorbed species and the forward and reverse rates of all elementary steps may then be calculated using a microkinetic model for a variety of reaction conditions. First, the possible reaction pathways are predicted.

3.4.1 Transition state theory

Transition state theory explains the reaction rates of elementary chemical reactions. As the figure 3.10, along the trajectory of the reaction, coordinate the transition state represents the maximum energy and in all other directions a minimum. This point is called a saddle point on the potential energy surface.

As the figure shows 3.10, the activation energy is the difference between the transition state (TS) and the initial state (IS), which is the energy barrier that has to be surpassed for the reaction to continue. The reaction energy is the difference between the final state (FS) and the initial state, which is the heat released or absorbed by the reaction step.[82]

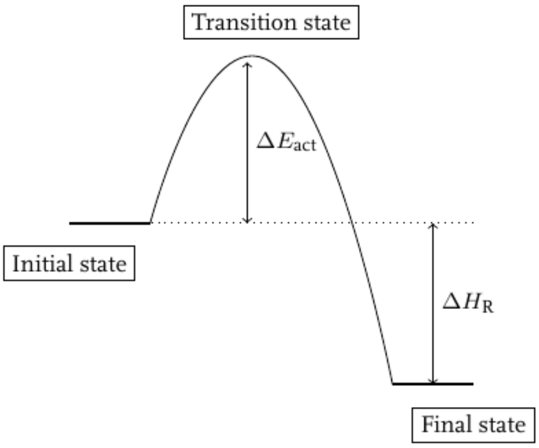

Figure 3.10: Elementary reaction step diagram with the reaction energy and activation energy. Image from [82].

From the VASP electronic energies of TS, IS and FS, the ΔH and ΔG of activation and reaction are calculated as presented before in 3.3.5. The electronic energies used for the calculations were of the adsorbed species alone, so e.g. in reaction 3.28 it would be E(A*) + E(B*), instead of E(A*+B*). With those values, reaction pathways are constructed to visualise the differences between reaction pathways and find the most favoured one.

Elementary surface reactions, like 3.28, define the rate surface reaction like $r = k\theta_A\theta_B$, where θ_A and θ_B are surface coverages of A and B species on the catalyst surface. The transition state was predicted using climbing image NEB calculations and the dimer method was used for further refinement of the transition state. To determine the rate coefficients of elementary surface reactions, the activation energies and reaction energies were calculated, including the entropies.

$$A^* + B^* \rightleftharpoons AB^{TS**} \tag{3.28}$$

3.4.2 Chemkin Simulations

The microkinetic modelling software used was Chemkin®, which is software to solve complex problems of chemical kinetics. The simulations performed in Chemkin were with a plug-flow reactor and 2 different types of feed were tested. One is $H_2/CO=2/1$ and the other is $H_2/CO_2=2/1$. The catalyst used was cobalt pure metal with terrace and edge sites.

The simulations were set to achieve a conversion of 10% of CO or CO_2, depending on the feed. The reactor temperature was set at 500 K. One model type was tested with low coverage. Two scenarios were tested with a dual-site catalyst or single-site catalyst, at 1 bar and 20 bar.

3.4.3 Result Analysis

The results obtained were analysed through conversion, selectivities, turnover frequencies (TOF), chain growth probability and surface coverages.

Both conversion and selectivity were calculated on a carbon basis. The equation 3.29, was used to calculate the conversion of reactant r (X_r), (in this case CO or CO_2, depending on the feed) which is the ratio between the molar amount of reacted r and the molar amount that enters in the reactor of r. The selectivity of a product i (S_i), was calculated with a carbon atom mass balance (equation 3.30).

$$X_r = \frac{F_{r,0} - F_r}{F_{r,0}} \tag{3.29}$$

$$S_i = \frac{n_{C,i} F_i}{F_{r,0} - F_r} \tag{3.30}$$

The turnover frequency (TOF) is the number of moles converted of reactant (CO or CO_2) per mole of active sites per unit time.It measures the efficiency of a catalytic active site.

The surface coverages (θ_i, i specie) of reaction intermediates were obtained from a microkinetic model, which can be simulated using Chemkin. Better knowledge of reaction intermediates and transition states helps construct the microkinetic model and improve the coverage effects.

Chapter 4

Cobalt-based Catalyst

4.1 Bulk Structures

The Co-based catalyst was studied in CO_2 hydrogenation through computational calculations. First, DFT calculations were made to set the right settings for bulk structure optimisation. **Convergence tests** were performed for Co FCC cubic (FCC-C), FCC orthorhombic (FCC-O) and HCP orthorhombic (HCP-O) unit cells to find the right cut-off energy, smearing width and k-points to optimise the structure and perform simulations. Proceeding as in section 3.3.1, the cut-off energy, smearing width and k-points used for each bulk structure is in table 3.1.

The obtained lattice constants for the optimised structures are in table 4.1. The results from the Murnaghan equation-of-state can be seen in figures 4.1 and 4.2, and the optimal volume, energy and bulk modulus are in table 4.1.

Table 4.1: Optimised bulk structures with VdW-DF functional and Murnaghan equation-of-state results.

	a^*(exp.)	b^*	c^*(exp.)	V (Å^3)*	V (Å^3)**	E (eV)**	B (GPa)**(exp.)
FCC-C	3.561 (3.55)[83]	3.561	3.561	45.17	45.77	-14.397	164.95
FCC-O	2.475	2.475	3.5	21.44	22.84	-7.195	164.58
HCP-O	2.524(2.51)[84]	2.524	4.072(4.07)[84]	44.95	45.09	-14.496	178.17(191)[84]

* Optimised values from VASP simulation.
** Optimised values from EOS estimation of Murnaghan.

The results for FCC-C from calculations in Table 4.1 differ from the experimental values ([84][83]) by 0.3%. Earlier reported DFT result for lattice constant is 3.538Å[85] for FCC-C which differs 0.012Å from the experimental value, while our value differs 0.011Å, from the experimental value (3.55Å). For the HCP-O structure the difference between calculated and experimental values of the lattice constant, *a*, is 0.6%. The functional used in the calculations was VdW-DF and the functional used in [85] was PW91. The difference between the experimental lattice constant and our DFT calculated value can be explained by the fact that VdW-DF is less accurate in describing the Metal-Metal bond interactions. The bulk modulus calculated for the HCP structure differs significantly from the experimental value of 191 GPa by 7%.

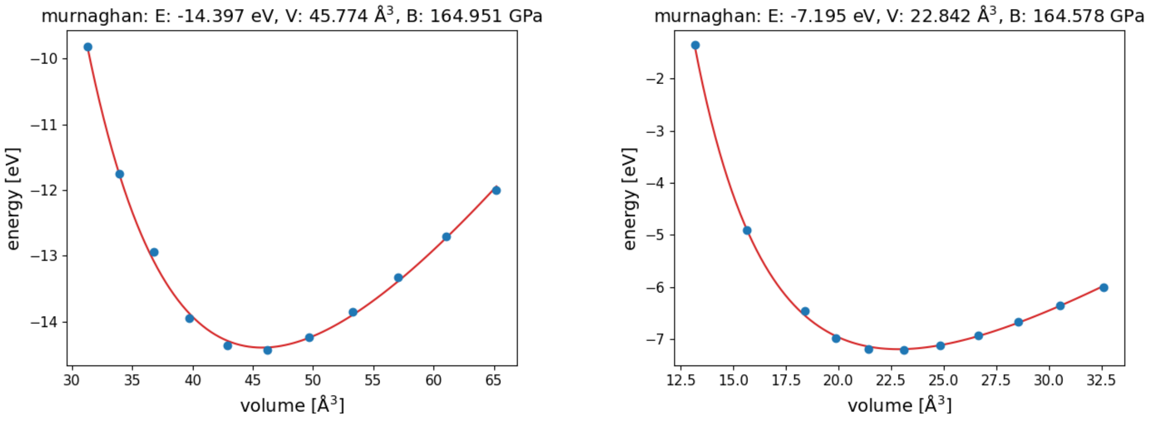

(a) FCC-C

(b) FCC-O

Figure 4.1: FCC bulk structures optimised with Murnaghan equation-of-state

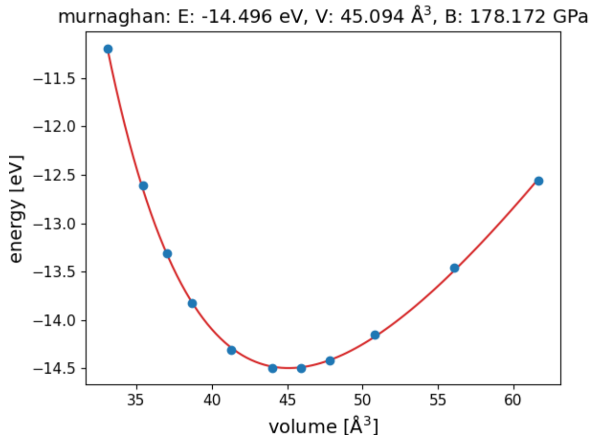

Figure 4.2: HCP-O bulk structure optimised with Murnaghan equation-of-state.

The optimal volume from the Murnaghan equation-of-state estimation deviates up to 6% from the volume calculated with VASP. This deviation can be reduced if more points are added to the estimation of the equation-of-state.

4.2 Surface Co(111)

For investigating CO_2 activation, the Co(111) surface was selected. The Co(111) surface was subjected to convergence tests to know how many layers (3 to 5) and fixed layers (1 to 2) to implement in the slab. A fixed layer means that the Co–Co distances are fixed at a value found from independent optimisation for the bulk structure, and the atoms in the other layers are left to move freely. Figure 4.3 shows the unit cells of the slab structures with 3, 4 and 5 layers. The number of atoms for each slab (a), (b) and (c) are 27, 36 and 45, respectively. The unit cell has a=7.556Å, and b=6.543Å, giving a surface area of 49.44Å^2, which is equal for all slabs in figure 4.3. The slab thickness for (a), (b), and (c) is 4.213Å, 6.269Å, and 8.326Å, respectively.

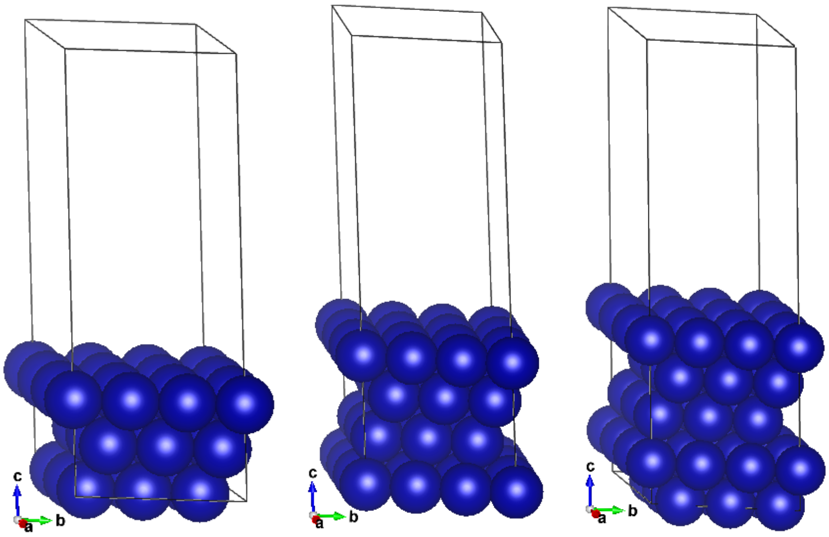

(a) 3 Layers (b) 4 Layers (c) 5 Layers

Figure 4.3: Representation of slab structures of Cobalt with (a) 3, (b) 4 and (c) 5 layers.

The formation energy calculated for slab structures is the average of the bottom and the top surface energies, since the top surface is relaxed and the bottom layer is unrelaxed the surface energies are slightly different. The average formation energies are in table 4.2. It is visible that the energy of the slab with 3 layers presents a higher energy when compared to the other energies, which can mean it is less stable. However, for further calculations, the slab with 3 layers and 1 fixed layer was chosen. Since more atoms in a unit cell make the simulations more computationally expensive.

Table 4.2: Average formation energy (J/m^2) of the bottom (unrelaxed) and top layers (relaxed) for each slab.

		Fixed layers		
		1	2	3
nº of layers	3	1.89	1.89	-
	4	1.80	1.82	1.83
	5	1.83	1.84	1.84

4.2.1 Adsorption of Molecules on Co(111)

Adsorption energies on Co(111) were calculated for all molecules in table 4.5. The stable structures for each molecule are in Appendix B in figure B.1. To better observe the difference between the number of layers and the number of fixed layers, the adsorption of CO on the top site of Co(111) was calculated and is available in table 4.3.

Table 4.3: Adsorption energy of CO on top site for different slabs.

	E$_{ads}$ (kJ/mol) CO top	**Fixed layers**		
		1	2	3
nº of layers	3	-135	-133	-
	4	-126	-128	-128
	5	-136	-136	-135

As discussed, a higher number of layers is an advantage to a more accurate calculation. But since the difference is not significant and the more atoms present in the slab require more computational resources, the 3 layers slab was chosen, since it presents fewer atoms in the unit cell.

In figure 4.4, the CO adsorption on 4 different active sites, top, bridge, fcc and hcp sites are presented. The adsorption energies of CO on the respective active sites are in table 4.4. The energy is corrected by adding the ZPE value of the molecule in the gas phase and the ZPE of the adsorbed molecule, in each case, to the electronic energy obtained in VASP. The most stable structure is CO adsorbed on the top site, with a value of -135 kJ/mol (energy not corrected). From the corrected values the most stable adsorption site is the hcp site in a slab with 3 layers with a corrected value of -130 kJ/mol (and on top adsorption has a value of -129 kJ/mol). Nonetheless, when comparing the sites with a larger slab (4 layers), the stable site is the top site with a corrected energy of -119 kJ/mol. The VdW-DF functional accurately predicts the correct adsorption site from the experiment. Inclusion of the van der Waals contribution weakens the low coverage CO adsorption energies and increases the preference for the top site.[34]

Table 4.4: Adsorption energies (E_{ads} values including ZPE in parentheses) of CO adsorption on top, fcc, hcp and bridge sites of Co(111).

	Calculated (with ZPE) (kJ/mol)	
CO adsorption	3 layers	4 layers
top	-135 (-129)	-126 (-119)
fcc	-131 (-127)	-116 (-113)
hcp	-134 (-130)	-120 (-116)
bridge	-127 (-123)	-120 (-116)*

* CO adsorbed molecule shifted positions from bridge site to hcp site.

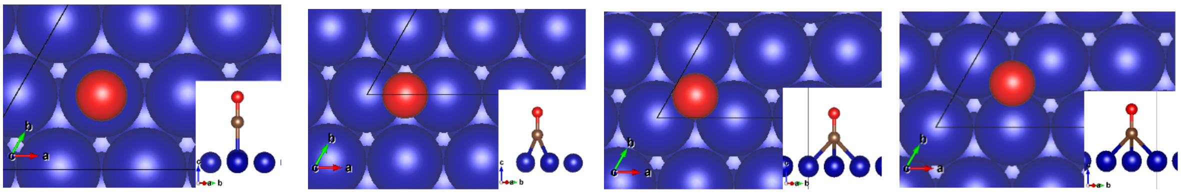

(a) top (b) bridge (c) fcc (d) hcp

Figure 4.4: VESTA representation of adsorbed CO on Co(111) on several active sites.

Table 4.5 shows the adsorption energies for several molecules on Co(111) with 3 layers and one fixed layer at coverage of 1/9 ML. As expected, the adsorption energies of CO_2, H_2O, CH_4, H_2CO and HCOOH are high. Comparing these values to Gunasooriya[34], most values differ less than 15%, except CH_3, HCOH and H_2CO which differ more than 25%. In this case, the structures found are more stable than the ones found by Gunasooriya.

Table 4.5: Adsorption Energies of molecules adsorbed on Co(111) with a coverage of 1/9 ML calculated with VdW-DF functional.

	E_{ads} (kJ/mol)	
Coverage 1/9 ML	Calculated	DFT[34] (exp.)
CO	-135	-130 (-128)[86]
C	-622	-614
H	-270	-270
O	-546	-539
CH	-606	-597
CO_2	-18	-16
H_2O	-26	-30
OH	-313	-327
CH_2	-352	-385
CH_3	-158	-211
CH_4	-14	
HCO	-191	-174
COH	-390	-384
COOH	-205	
HCOH	**-360**	**-276**
H_2CO	**-61**	**-35**
HCOO	-400	
HCOOH	-12	

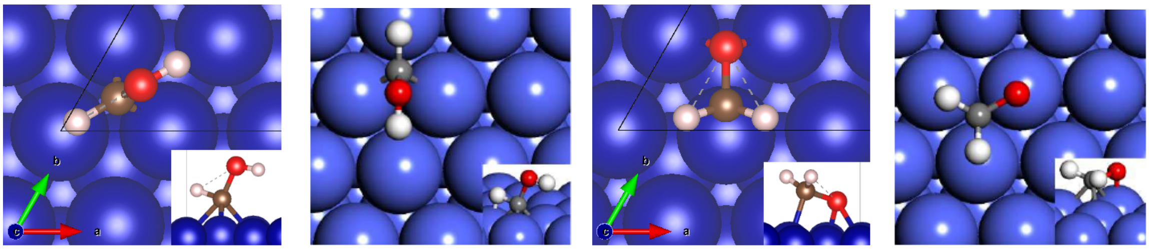

(a) HCOH (b) HCOH[34] (c) H_2CO (d) H_2CO[34]

Figure 4.5: VESTA representation of adsorbed HCOH and H_2CO on Co(111) from this work (a and c) and Gunasooriya[34] (b and d).

The molecules with a higher adsorption energy difference from Gunasooriya, HCOH and H_2CO, can be compared in figure 4.5. The geometry of adsorbed HCOH in this work has the carbon atom on the fcc site, and from Gunasooriya's work, the carbon is between a bridge site and an hcp site. As for the H_2CO, it is visible that the geometry from this work has the oxygen on the bridge site, and the oxygen in figure 4.5(d) is on top and the carbon on the fcc site. The different configuration of the H_2CO molecule on Co(111) is more visible.

4.2.2 Transition States

The CO_2 hydrogenation on a catalyst can be predicted by testing several reaction pathways computationally. The reactions 4.1 to 4.10 were studied on Co(111) using NEB and Dimer methods to find the transition states. From the reactions mentioned, the transition states found were the CO_2 hydrogenation with OH (4.3) and with H (4.4 and 4.5), HCOO hydrogenation (4.6) and dissociation reactions of CO_2, HCOO and COOH (4.1, 4.9 and 4.10). For the other reactions no transition states were found, either the simulation 'exploded' (excess of energy) or the vibrational frequencies were not corresponding to a transition state.

$$CO_2 + 2^* \longrightarrow CO^* + O^* \tag{4.1}$$

$$CO_2 + OH^* +^* \longrightarrow HCOO^* + O^* \tag{4.2}$$

$$CO_2 + OH^* +^* \longrightarrow COOH^* + O^* \tag{4.3}$$

$$CO_2 + H^* \longrightarrow HCOO^* \tag{4.4}$$

$$CO_2 + H^* \longrightarrow COOH^* \tag{4.5}$$

$$HCOO^* + H^* \longrightarrow HCOOH^* +^* \tag{4.6}$$

$$HCOOH^* +^* \longrightarrow HCO^* + OH^* \tag{4.7}$$

$$COOH^* + H^* \longrightarrow HCOOH^* +^* \tag{4.8}$$

$$HCOO^* +^* \longrightarrow HCO^* + O^* \tag{4.9}$$

$$COOH^* +^* \longrightarrow CO^* + OH^* \tag{4.10}$$

The activation and reaction energies were calculated at 0.1 MPa, and 500 K. Table 4.6 summarises calculated activation energies from DFT electronic energies, Gibbs free energies of activation and reaction free energies.

Table 4.6: Activation energies from DFT (VdW-DF), Gibbs free energy barriers and Gibbs free energies of reaction for studied reactions and their transition states.

IS FS	CO_2*+* CO*+O*	CO_2*+OH* COOH*+O*	CO_2*+H* HCOO*+*
TS	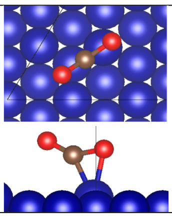	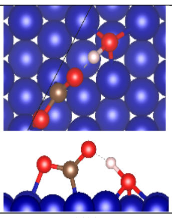	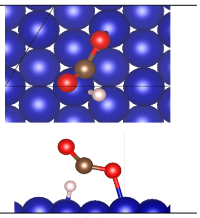
Activation Energy (kJ/mol)	70	55	102
ΔG activation (kJ/mol)	69	57	98
ΔG reaction (kJ/mol)	-80	45	6

IS FS	CO_2*+H* COOH*+*	HCOO*+H* HCOOH*+*	HCOO*+* O*+HCO*	COOH*+* CO*+OH*
TS	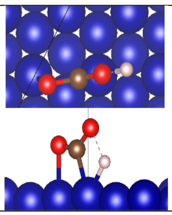	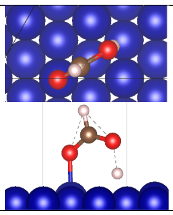	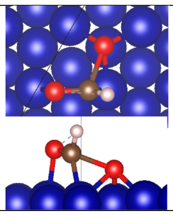	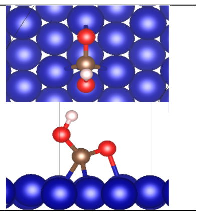
Activation Energy (kJ/mol)	154	108	92	22
ΔG activation (kJ/mol)	150	98	87	6
ΔG reaction (kJ/mol)	62	63	35	-125

Figures 4.6 and 4.7 are energy profiles for the reactions studied. Both enthalpy and Gibbs free energy for TS, IS and FS were calculated as presented in the Section 3.3.5, and the energy barriers and reactions energies as in Section 3.4.1.

In both figures, CO_2+2*+OH*+H* is the reference state (IS, which is the 0 value). Energies for important intermediates and transition states are indicated. The path of CO_2 hydrogenation with OH* to form COOH* is the least energy requiring.

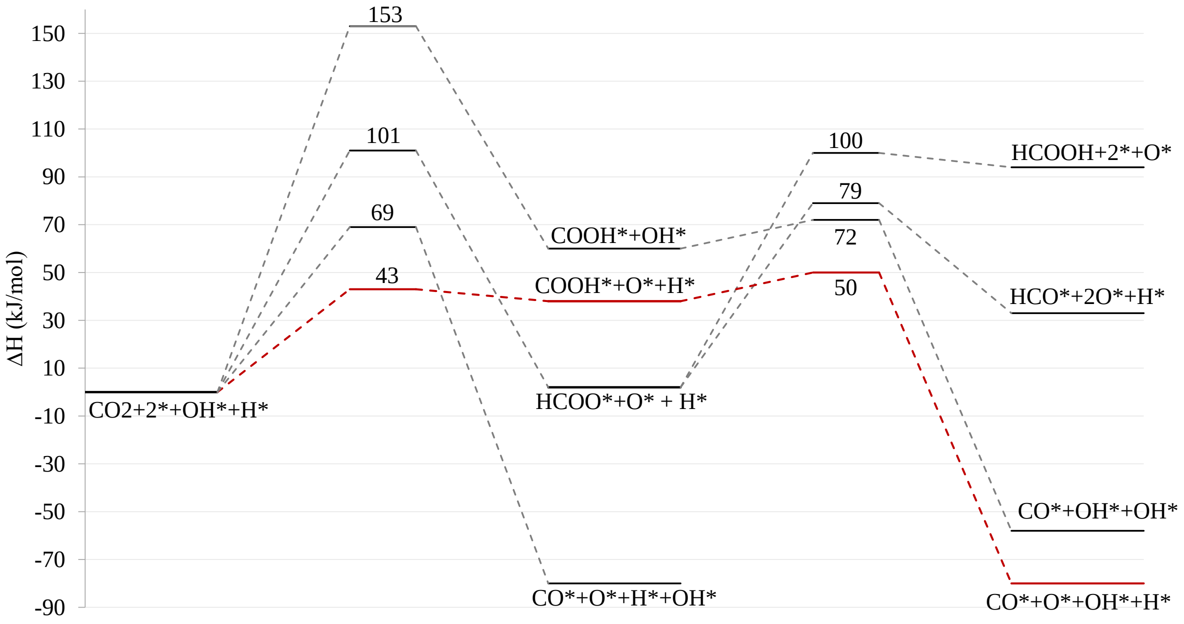

Figure 4.6: ΔH energy profile of the reactions studied which form a pathway for CO_2 hydrogenation on Co(111).

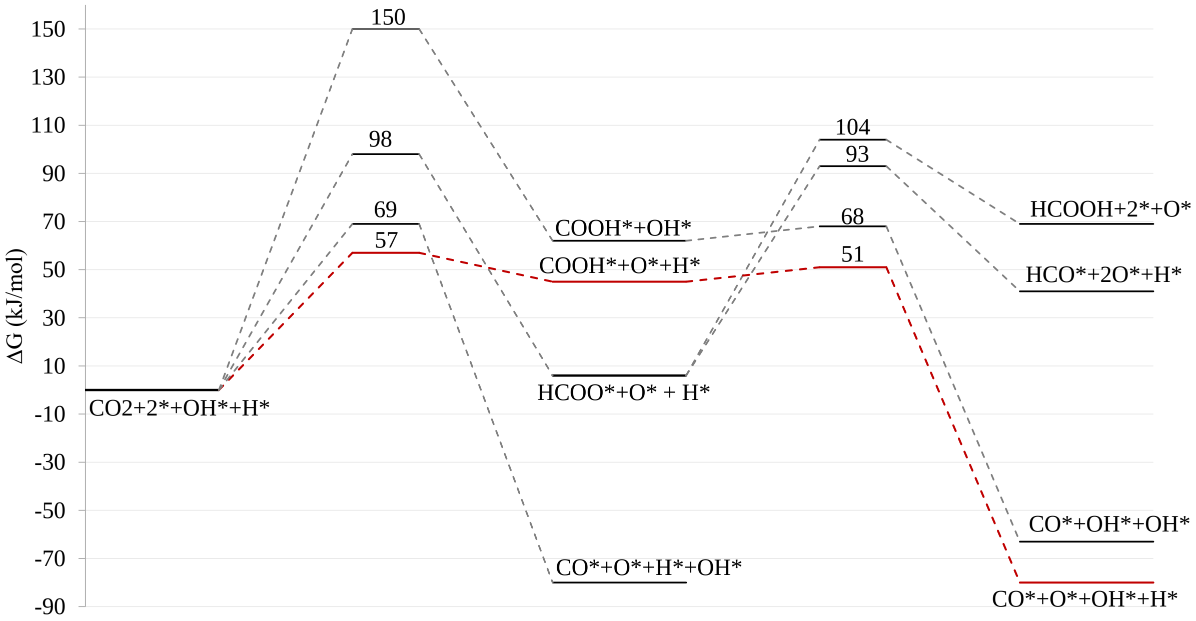

Figure 4.7: ΔG energy profile of the reactions studied which form a pathway for CO_2 hydrogenation on Co(111).

4.3 Microkinetic Modelling

The microkinetic model used in Chemkin was the same as implemented by Gunasooriya [34] (dual-site microkinetic model), where reactions on cobalt terrace sites were at low coverage and the reactions on B_5 step sites (edge sites) are at high coverage, but results should not be affected. In future work, these reactions should also be calculated at low coverages. The microkinetic model was studied with either CO or CO_2 as feeds. With a pressure of 1 or 20 bar for cobalt catalyst pure metal at low coverage, 2 scenarios were analysed:

A. Single site catalyst - Only terrace sites present.

B. Dual site catalyst - Both terrace and edge (10%) sites present.

4.3.1 CO feed

The CO feed ($H_2/CO=2/1$) was analysed for low CO coverage for the 2 scenarios. The results are present in table 4.7. For all cases the main product is methane, at 1 bar the methane selectivity is 87% for scenario **A**, and 99.9% for scenario **B**.

Table 4.7: Results from the low coverage model in Chemkin with a CO feed at the specified pressure.

Scenario	Pressure (bar)	CO conversion (%)	TOF (s^{-1})	CH_4	CO_2	C_1-C_4*
A	1	10.04	1.72E-05	86.75%	13.25%	0.00%
A	20	10.04	4.01E-05	91.51%	8.42%	0.08%
B	1	10.05	0.253	99.85%	0.15%	0.00%
B	20	10.04	2.30	99.96%	0.04%	0.00%

* C_1 molecules with the exception of CO_2 and CH_4.

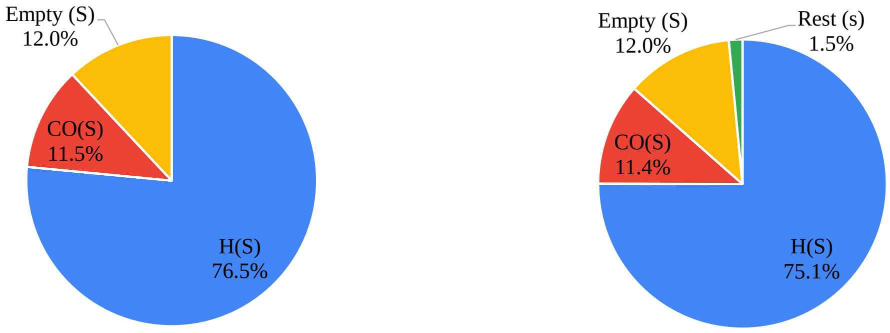

(a) Scenario **A - 1bar** (b) Scenario **B - 1bar**

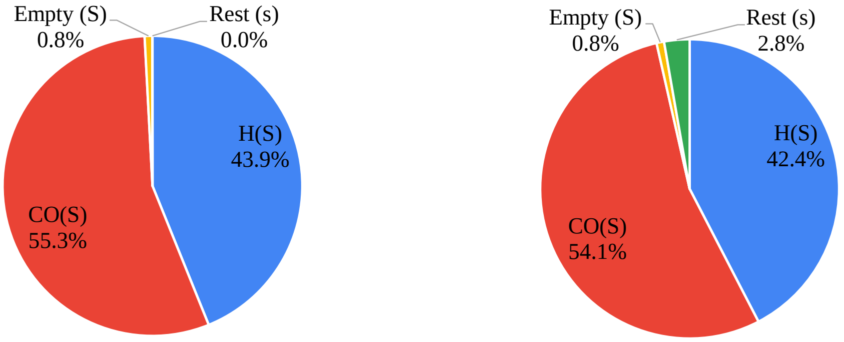

(c) Scenario **A - 20bar** (d) Scenario **B - 20bar**

Figure 4.8: CO feed results on surface coverages (S stands for terrace site) of CO, H, rest of the molecules and empty terrace site for scenario **A**, and scenario **B** at 1 bar and 20 bar.

The scenario **A** at 20 bar presents a 0.08% selectivity for C_1-C_4 molecules. Also, scenario **A** produces a higher CO_2 content than scenario **B**, the increase in pressure seems to reduce CO_2 formation and the addition of edge sites also decreases the CO_2 production.

At both 1 and 20 bar, scenario **B** presents a high TOF, of 0.253 and 2.30 s^{-1}, respectively. The addition of edge sites favours methane formation. At these conditions, this catalyst is suitable for methanation. The surface coverages are presented in figure 4.8, where the terrace site coverages are higher. As for the coverage of the edge site in scenario **B** is 99.9%(1 bar) and 95.5%(20 bar) empty. The terrace coverage of CO and H is quite the same for both scenarios, with the exception of a small percentage of terrace sites that are covered with other intermediates (up to C_3 alkanes, alkenes, alcohols, ketones and aldehydes). The increase in pressure to 20 bar makes the coverage of CO on the terrace site increase (approximately 44% increase), and the coverage of H on the terrace site (approximately 33% decrease) and empty terrace site both decrease. At high pressure, CO coverage is higher than the coverage used in DFT (1/9ML). So the high CO coverage on the terrace site with high pressure (20 bar) is an invalid calculation because DFT calculations would be needed at higher CO coverages. The H coverage obtained in the microkinetic model is higher than the H coverage in DFT calculations. DFT calculations of H at high coverage are needed to better assess the high coverage adsorption energy of H. The overestimated H coverage is partially responsible for high methane selectivity.

4.3.2 CO_2 feed

The CO_2 feed (H_2/CO_2=2/1) was also analysed for both scenarios. Table 4.8 presents the results obtained. As seen the main product formed is CO* for the single-site scenario at 1bar. When increasing the pressure to 20 bar the production of CH_4 increases and CO decreases. The addition of edge sites also increases the production of methane, as predicted with CO feed.

Table 4.8: Results from the low coverage model in Chemkin with a CO_2 feed at the specified pressure.

Scenario	Pressure (bar)	CO_2 conversion (%)	TOF (s^{-1})	CH_4	CO	C_1-C_4
A	1	10.00	1.36E-06	18.31%	81.69%	0.00%
A	20	10.11	1.81E-06	88.28%	11.72%	0.00%
B	1	9.97	1.35E-06	99.99%	0.01%	0.00%
B	20	10.04	1.73E-06	100.00%	0.00%	0.00%

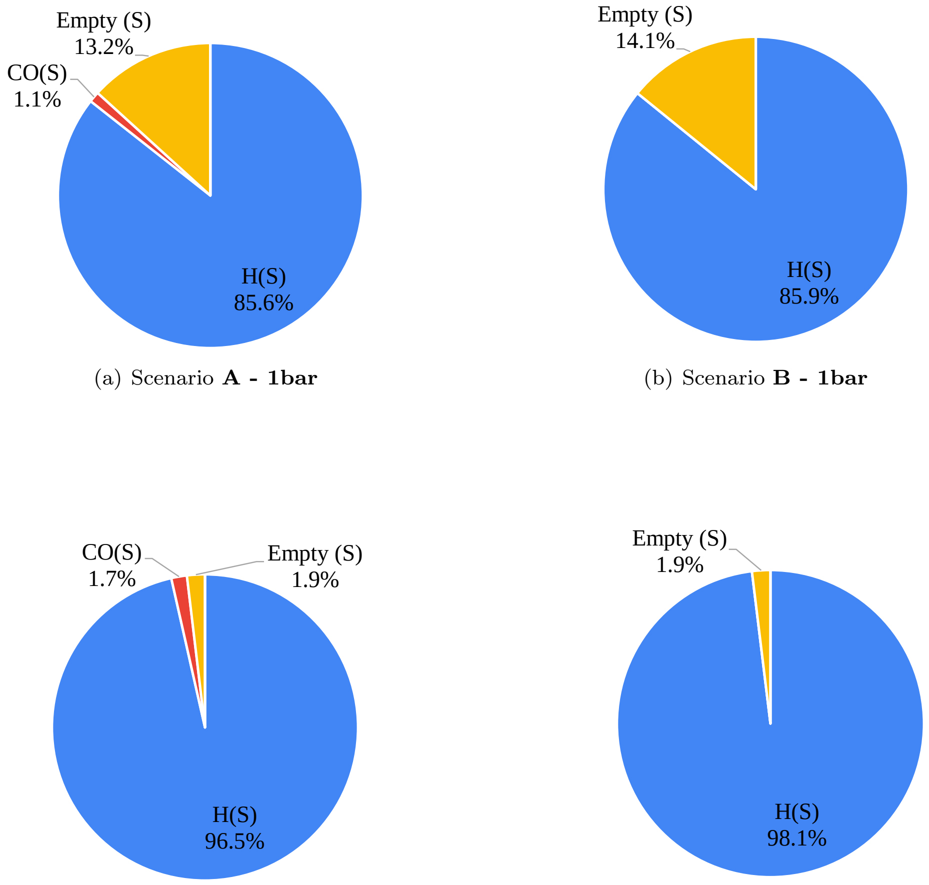

(a) Scenario **A - 1bar**

(b) Scenario **B - 1bar**

(c) Scenario **A - 20bar**

(d) Scenario **B - 20bar**

Figure 4.9: CO_2 feed results on surface coverages (terrace site) of CO, H, rest of the molecules and empty terrace site for scenario **A**, and scenario **B** at 1 bar and 20 bar.

In none of the scenarios presented and pressure tested the C_1-C_4 selectivity goes past 0.00%. However, in scenario **A** at 1 bar the CO selectivity reaches 81.7%, which suggests a possible high CO* formation on the catalyst. The coverages seen show that the increase in pressure increases H coverage on the terrace site. The addition of edge sites decreases CO coverage on the terrace sites. The edge site remains empty at 1 and 20 bar for scenario **B**.

For CO hydrogenation, the TOF is higher compared to the TOF obtained from CO_2 hydrogenation in all scenarios and pressures. But for scenario **B** the TOF is much higher in CO hydrogenation. For both CO and CO_2 hydrogenation, methane is the product with the higher selectivity. However, for CO_2 hydrogenation, in scenario **A** at low pressure the CO presents a high selectivity. The CO_2 hydrogenation presents a low CO coverage compared to CO hydrogenation. The H coverage for both reactions is high, but for CO_2 hydrogenation it is high in both scenarios and pressures. So DFT calculations of H at high coverage would be needed in order to build a more accurate microkinetic model.

Chapter 5

Iron-based Catalyst

5.1 Bulk Structures

The iron carbide bulk structures studied were χ-Fe_5C_2, ϵ-Fe_3C, η-Fe_2C and θ-Fe_3C. Section 3.2.2 is described how the bulk structures were made, and figure 5.1 are shown their geometries. Convergence test results of ENCUT, k-points and smearing width are available in table 5.1. Some settings were chosen according to the Materials Project input settings.[66]

Table 5.1: Settings of input files for VASP calculations of geometry optimisation and amount of atoms in each unit cell.

	ϵ-Fe_3C	η-Fe_2C	χ-Fe_5C_2	θ-Fe_3C
ENCUT (eV)	500	500	500	500
smearing width (eV)	0.05	0.05	0.05	0.20
k-points	6×6×6	8×6×6	6×6×4	6×4×4
Mesh	Gamma	Monkhorst	Monkhorst	Monkhorst
Fe atoms	6	4	20	12
C atoms	2	2	8	4

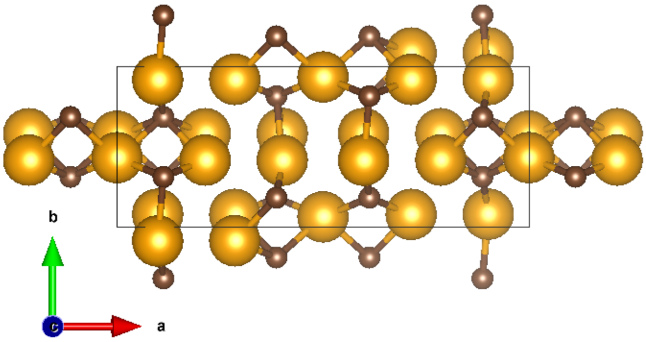

(a) χ-Fe_5C_2

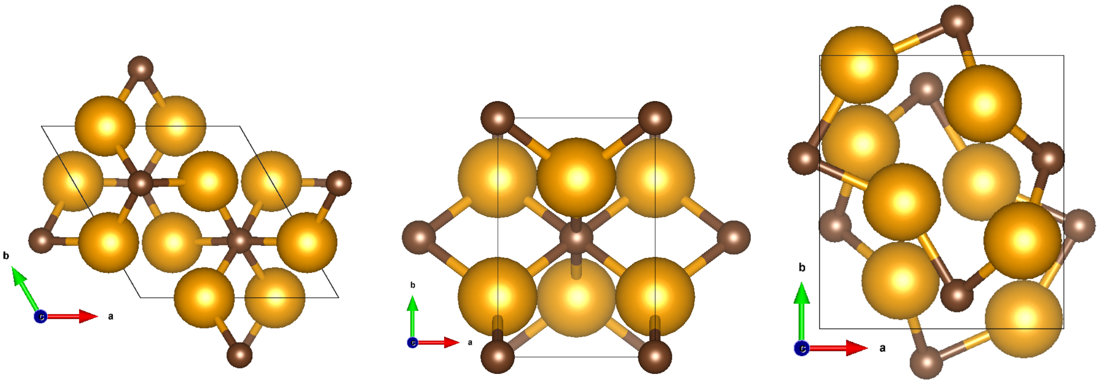

(b) ϵ-Fe_3C (c) η-Fe_2C (d) θ-Fe_3C

Figure 5.1: Iron carbides bulk structures studied. The yellow and brown atoms represent the Fe and C atoms, respectively.

The results of the geometry optimisation for each bulk structure are in table 5.2, including DFT and experimental results from the literature.

Table 5.2: Iron carbide bulk structures lattice constants, optimal volume, bulk modulus and cohesive energy from this work, DFT reference and experimental values.

		a (Å)	b (Å)	c (Å)	V (Å^3)	B (GPa)	E_{coh}(eV/atom)
ϵ-Fe_3C	This work*	4.662	4.662	4.32	80.6	209.27	-5.69
	DFT[87]	4.548	4.548	4.286		175	-5.48
	Exp.[88]	4.767	4.767	4.354	98.9		
η-Fe_2C	This work*	4.714	4.282	2.824	56.6	245.55	-5.93
	DFT[87]	4.496	4.262	2.766		197	-5.72
	Exp.[89]	4.704	4.318	2.830			
χ-Fe_5C_2	This work*	11.593	4.493	4.976	258.0	240.37	-5.79
	DFT[87]	10.679	4.493	4.957		219	-5.60
	Exp.[90]	11.562	4.573	5.0595	265.1		
θ-Fe_3C	This work*	5.016	6.734	4.470	151.3	230.78	-5.69
	DFT[87]	4.979	6.315	4.491		209	-5.45
	Exp.[91]	5.088	6.742	4.526	155.3	175	

As seen in table 5.2, the results are in agreement with DFT values and experimental values. The DFT values in ref. [87] are also obtained with the PBE functional. The calculated cohesive energies compared to Hyodo et al.[87] present a maximum absolute difference of 0.24 eV/atom (which is a 4% difference) in all bulk structures. In this work, the calculated values are higher in all cases, which can be due to different settings used in the simulations.

---

*These results are with PBE functional.

Formation energies of the analysed bulk structures are available in table 5.3 for different carbon chemical potentials, including literature (from Liu et al.[79]) values to compare. It is seen that the formation energy decreases with an increase in carbon chemical potential. The formation energy of $\eta - Fe_2C$ is the lowest which is also confirmed by Liu et al., which can be considered the most stable bulk structure compared to the others. The $\chi - Fe_5C_2$ is the next structure with low formation energy.

Table 5.3: Formation energies for each iron carbide bulk structure with two different chemical potentials of carbon. PBE functional was used for calculations and also for Liu et al. values.[79]

	$\epsilon - Fe_3C$	$\eta - Fe_2C$	$\chi - Fe_5C_2$	$\theta - Fe_3C$
μ_C=-6.65 eV	-0.602	-0.816	-0.696	-0.605
μ_C=-7.56 eV	-0.375	-0.513	-0.436	-0.378
μ_C=-6.60[79] eV		-0.840	-0.81	-0.75

In figure 5.2, it is compared the values of formation energies for each iron carbide calculated with different functionals (PBE and VdW-DF). The carbon chemical potentials used were from PBE, -6.65 eV and from VdW-DF, -5.63 eV. The VdW-DF gives the highest values for formation energies. Nonetheless, the functionals agree that $\eta - Fe_2C$ has the lowest formation energy compared with the other iron carbides.

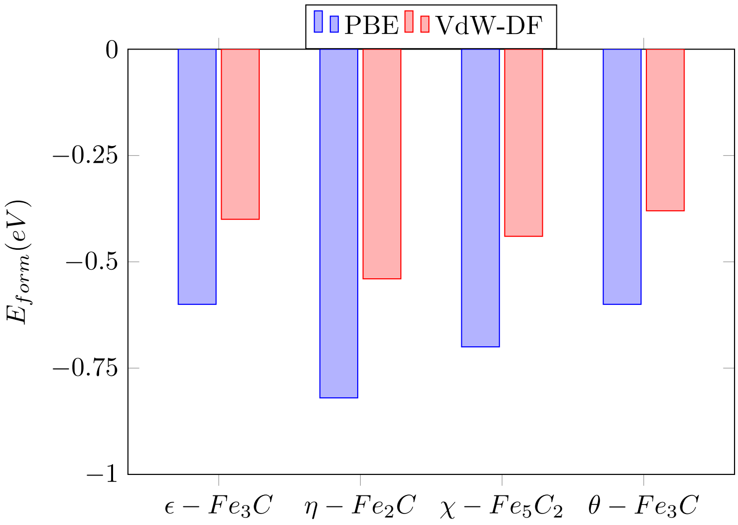

Figure 5.2: Formation energies (μ_C =-6.65 eV) calculated for all iron carbides studied with PBE, VdW-DF and SCAN-rVV10 functionals

The geometry optimisation of each iron carbide, with the Murnaghan equation-of-state, is available in figure 5.3. To find a more accurate optimal volume more points must be added in the minimum region.

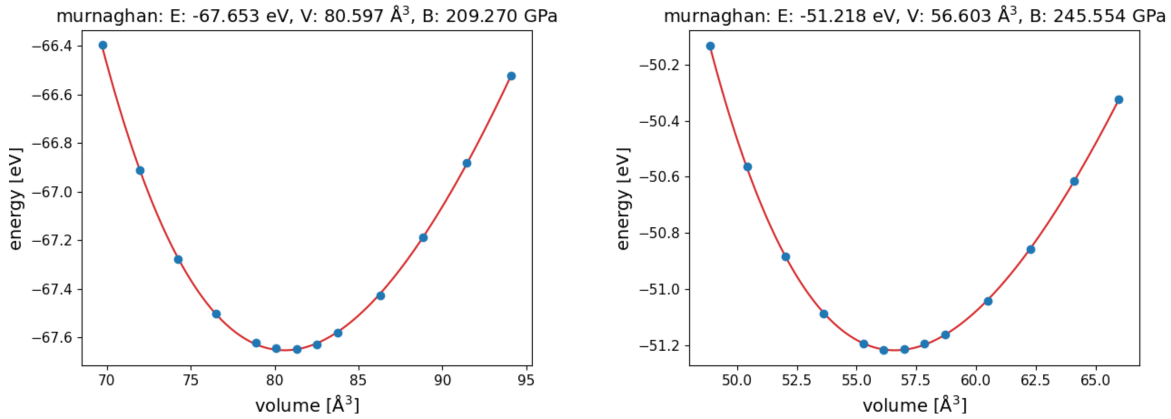

(a) ϵ-Fe$_3$C (b) η-Fe$_2$C

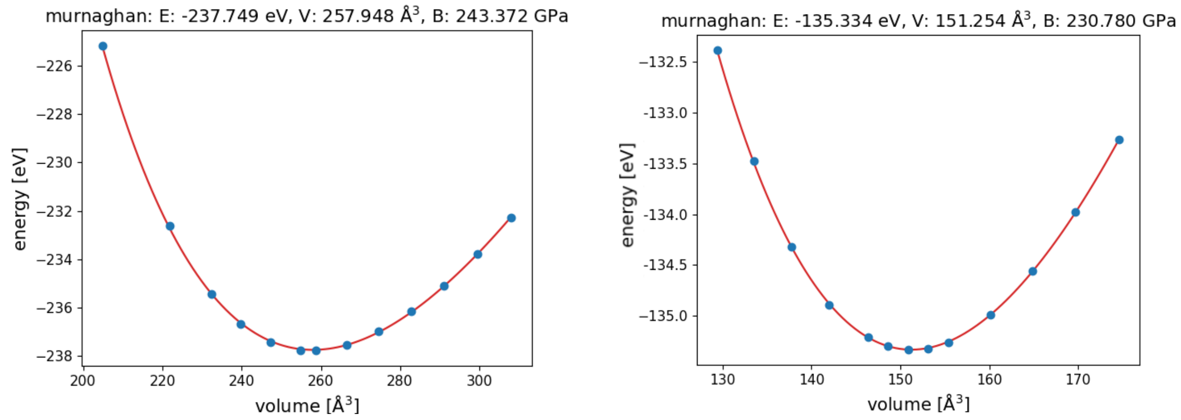

(c) χ-Fe$_5$C$_2$ (d) θ-Fe$_3$C

Figure 5.3: Iron carbides bulk structures optimised with Murnaghan equation-of-state.

5.2 Surfaces

The iron carbide surfaces were studied with 3 different functionals (PBE, VdW-DF and SCAN-rVV10), and convergence tests were performed to start geometry optimisations with the correct settings. The settings used in VASP calculations are summarised in table 3.2. The surfaces studied were low Miller index facets, with the exception of χ-Fe$_5$C$_2$(510) which is a high Miller index facet.

The Fe/C ratio and surface energy were analysed for different carbon chemical potentials. Wulff constructions were made based on these surface energies. Preferably, symmetric and stoichiometric slabs are used, but occasionally non-stoichiometric slabs were also studied. Wulff constructions were only made for χ-Fe$_5$C$_2$ and θ-Fe$_3$C bulk structures. The carbon chemical potential relation with the surface energy was analysed for non-stoichiometric slabs ($\epsilon(001)_{0.0}$, $\epsilon(011)_{0.0}$, $\epsilon(101)_{0.0}$, $\eta(001)_{0.0}$, $\eta(011)_{0.0}$, $\eta(101)_{0.0}$, $\eta(110)_{0.0}$, $\chi(100)_{0.0}$ and $\chi(100)_{0.287}$).

5.2.1 ϵ-Fe$_3$C

The ϵ-Fe$_3$C surfaces studied are $(001)_{0.0}$, $(011)_{0.0}$ and $(101)_{0.0}$. Figures 5.4 and A.3 show the surface geometries. The calculated surface energies are summarised in figure 5.5 and the respective values are in table B.4. The most stable surface according to calculations is the $(101)_{0.0}$ with a surface energy of 2.32 J/m^2 (PBE), however, according to Broos et al.[92] the most stable surface is the $(001)_{0.0}$ with a surface energy of 1.58 J/m^2 (PBE). Broos et al. made the surfaces according to the ϵ-Fe$_2$-0.25C bulk structure (figure 5.6), which presents a higher carbon content. Thus, the surfaces from Broos et al. present a lower Fe/C ratio of 2 compared to a Fe/C ratio of 3 of the surfaces calculated in this work. The presence of higher carbon content on the surface increases surface stability.

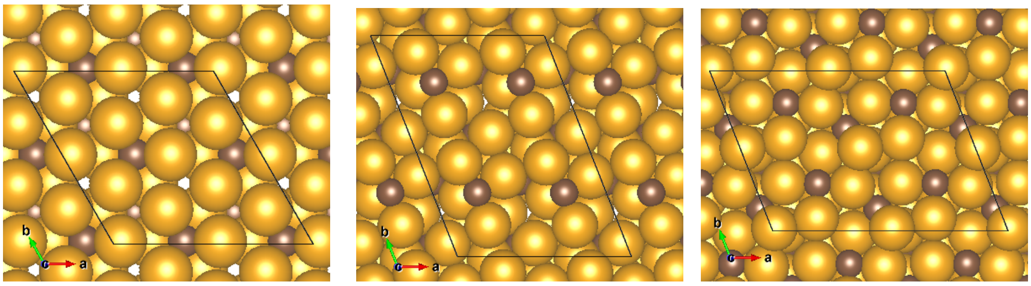

(a) $(001)_{0.0}$ (b) $(011)_{0.0}$ (c) $(101)_{0.0}$

Figure 5.4: Top view of slab surfaces of constructed ϵ-Fe$_3$C.

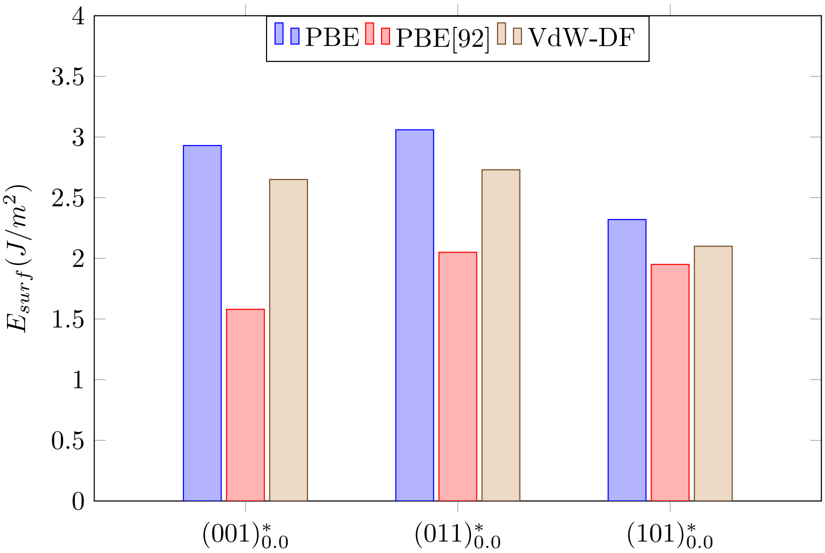

Figure 5.5: Surface energy of ϵ-Fe$_3$C asymmetric surfaces for PBE, VdW-DF and SCAN-rVV10 functionals and reference values. (*) Asymmetric and stoichiometric surfaces.[92]

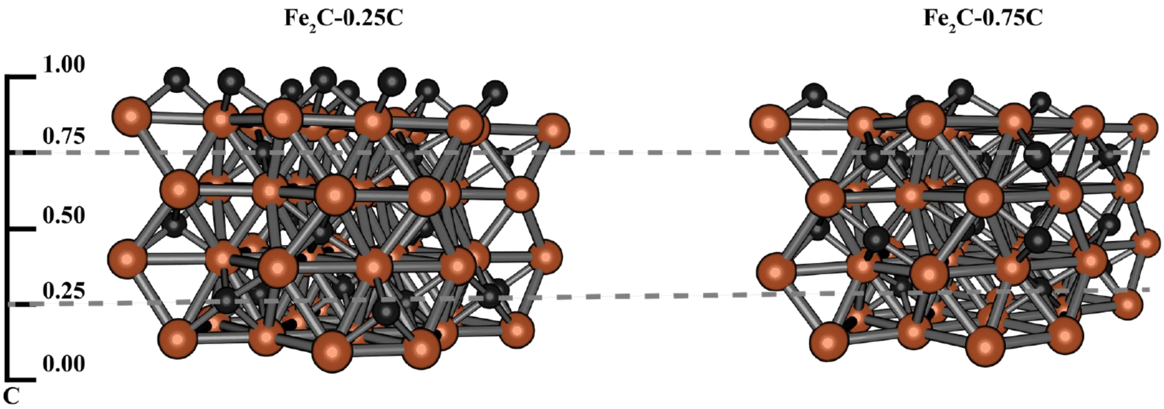

Figure 5.6: ϵ-Fe carbides bulk structures with two additional non-symmetry conforming carbon layers at c = 0 and c = 0.25 (ϵ-Fe_2-0.25C), and at c = 0 and c = 0.75 (ϵ-Fe_2-0.75C). Image from [92].

Since the chemical potential varies for different FT conditions, the surface energies will vary accordingly. Figure 5.7 shows the relation of the surface energy with the chemical potential. As seen, the $\epsilon(001)_{0.0}$ presents a high surface energy compared to $\epsilon(011)_{0.0}$ and $\epsilon(101)_{0.0}$ surfaces. Since these surfaces are non-stoichiometric, the surface $\epsilon(001)_{0.0}$ presents a ratio Fe/C=4.5, while the other two surfaces have a ratio Fe/C=3.25 (see table B.4). This suggests that the higher carbon content on the surface stabilises the surface. The carbon chemical potential is smaller at the higher conversion stage of FTS which indicates FT products are in equilibrium with the C in carbide, corresponding to the typical steady-state condition of FTS.[79] And since it decreases the surface energy the surface becomes more stable. The low conversion stage of FTS is represented by the high carbon chemical potential (μ_C=-6.65 eV), when the C from the reactant CO enters into solid-forming carbide phases.[79] Also, the carbon chemical potential varies with temperature, total pressure and partial pressures of species.

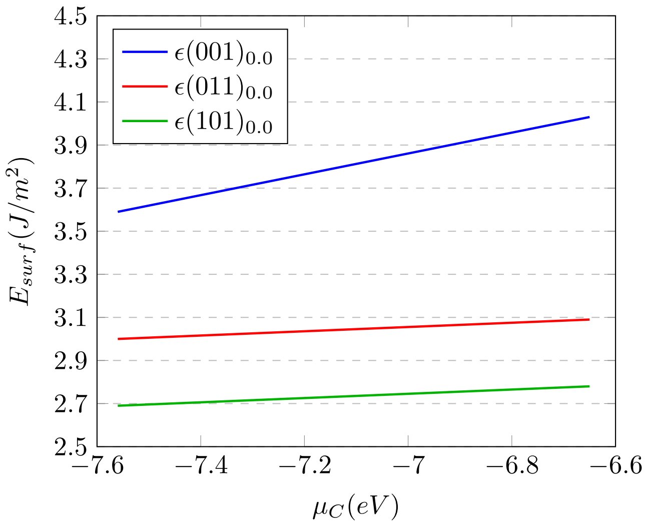

Figure 5.7: Surface energy of non-stoichiometric surfaces of ϵ-Fe_3C with varying chemical potential of carbon. Calculated with PBE functional.

5.2.2 η-Fe$_2$C

The η-Fe$_2$C surfaces studied are $(001)_{0.0}$, $(011)_{0.0}$, $(101)_{0.0}$, $(110)_{0.0}$ and $(100)_{0.0}$, and only the latter is symmetric and stoichiometric, the others are asymmetric and stoichiometric. Figure 5.9 reveals that the most stable surface calculated is the $(100)_{0.0}$ for all functionals used. The $(100)_{0.0}$ has a surface energy of 2.53 J/m^2 (PBE) and according to Bao et.al.[93] the most stable surface is $(011)_{0.0}$ with a surface energy of 2.40 J/m^2. Bao et al. managed to make all slabs symmetric, which makes the surfaces different from the ones calculated in this work. Since the surface energy calculation with equation 3.7 is the average of the top and bottom surface energies on the slab, for asymmetric surfaces the energy will be different from symmetric surfaces. All η-Fe$_2$C surfaces have carbon atoms on top of the surface and for asymmetric slabs, the bottom will have less to no carbon content (see figure 5.8).

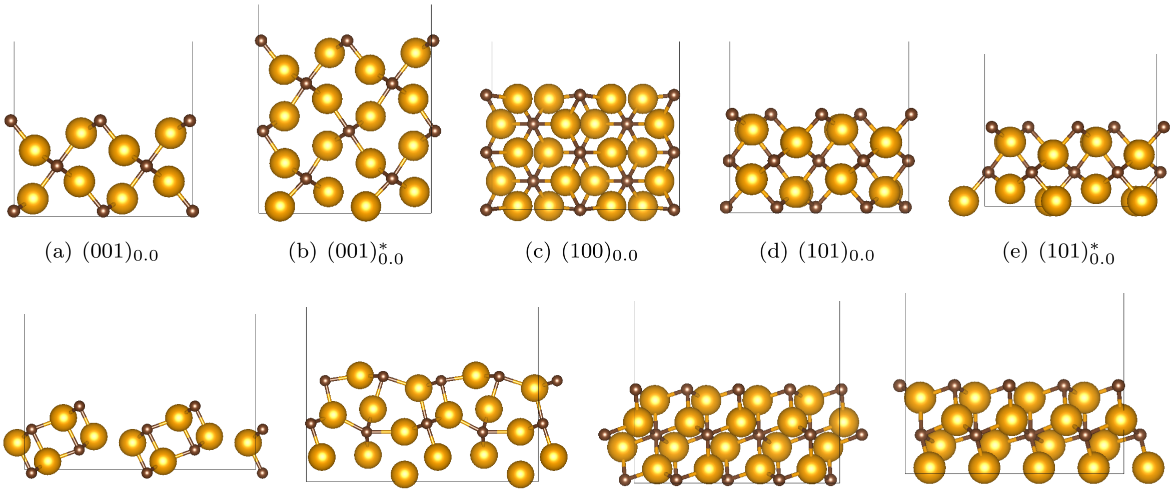

(a) $(001)_{0.0}$ (b) $(001)^*_{0.0}$ (c) $(100)_{0.0}$ (d) $(101)_{0.0}$ (e) $(101)^*_{0.0}$

(f) $(011)_{0.0}$ (g) $(011)^*_{0.0}$ (h) $(110)_{0.0}$ (i) $(110)^*_{0.0}$

Figure 5.8: Side view of slab surfaces constructed of η-Fe$_2$C.

The functionals show agreement for the stability of the surfaces, and their decreasing stability order is $(100)_{0.0} > (101)^*_{0.0} > (001)^*_{0.0} > (110)^*_{0.0} > (011)^*_{0.0}$.

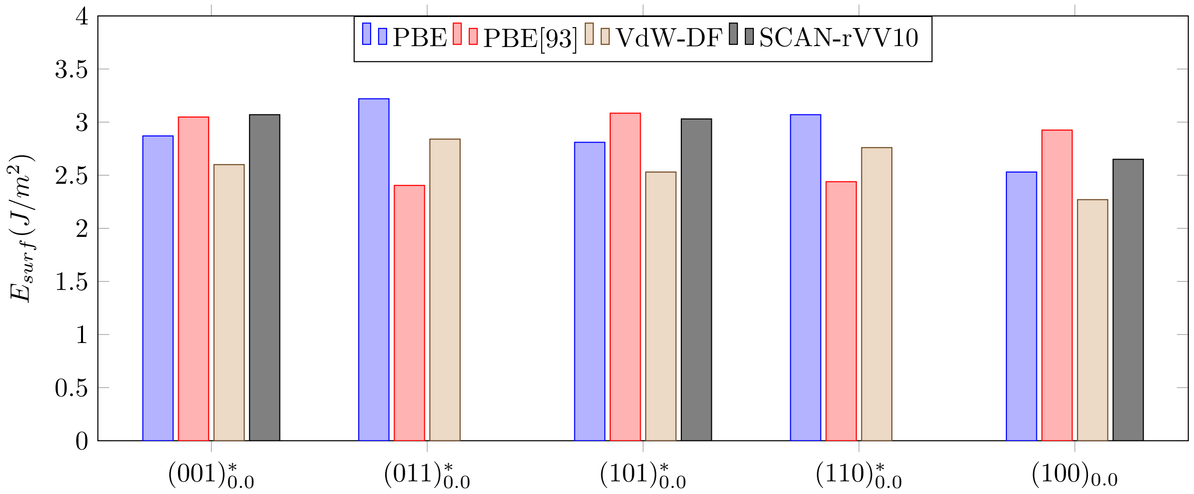

Figure 5.9: Surface energy of η-Fe_2C surfaces for PBE, VdW-DF and SCAN-rVV10 functionals and reference values. (*) Asymmetric and stoichiometric surfaces.[93]

Figure 5.10, shows that the surface $(011)_{0.0}$ is the most stable compared to the other surfaces since it presents a Fe/C ratio of 1, which is lower than the ratio of the other surfaces Fe/C=1.33. With the increase of carbon chemical potential the more stable the surface becomes. These surfaces all have a high carbon content compared to the bulk structure Fe/C=2. The surface energy is linearly dependent on the chemical potential, and the slope of the curve depends on the actual carbon content of the surface slab. When there are more carbons in the slab than in the bulk structure, the carbon contribution is positive which makes the slope negative (see equation 3.6).

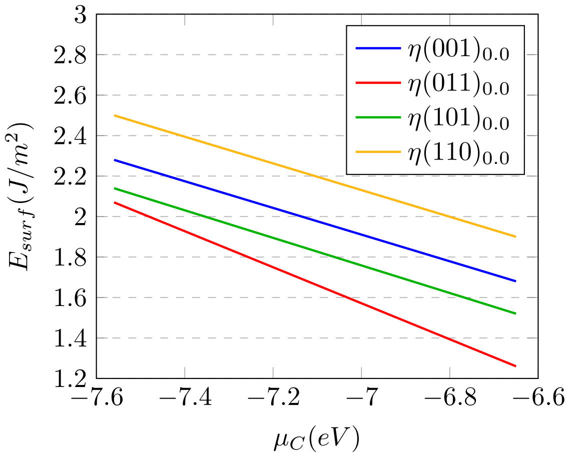

Figure 5.10: Surface energy of non-stoichiometric surfaces of η-Fe_2C with varying chemical potential of carbon. Calculated with PBE functional.

5.2.3 χ-Fe_5C_2

The χ-Fe_5C_2 surfaces are $(100)_{0.0}$, $(100)_{0.287}$, $(010)_{0.25}$, $(11\bar{1})_{0.0}$, $(11\bar{1})_{0.5}$ and $(510)_{0.0}$. Figure 5.11 shows that the most stable surface calculated is the $(510)_{0.0}$ (2.07 J/m^2, PBE) according to all functionals and Liu et al.[79]. The value of surface energy from Liu et al. of $(510)_{0.0}$ is 1.75 J/m^2, and the Fe/C ratio is 2, while for the surface in this work the ratio is 2.5, which could explain why the surface energy from this work is higher. The (510) surface from Liu et al. suffered a reconstruction, extra C atoms arrived to occupy the 4-fold Fe vacant sites. This reconstruction was discovered by the stochastic surface walking (SSW) neural network (NN) potential developed by the group of Liu et al., by iterative self-learning method of SSW-NN data set.

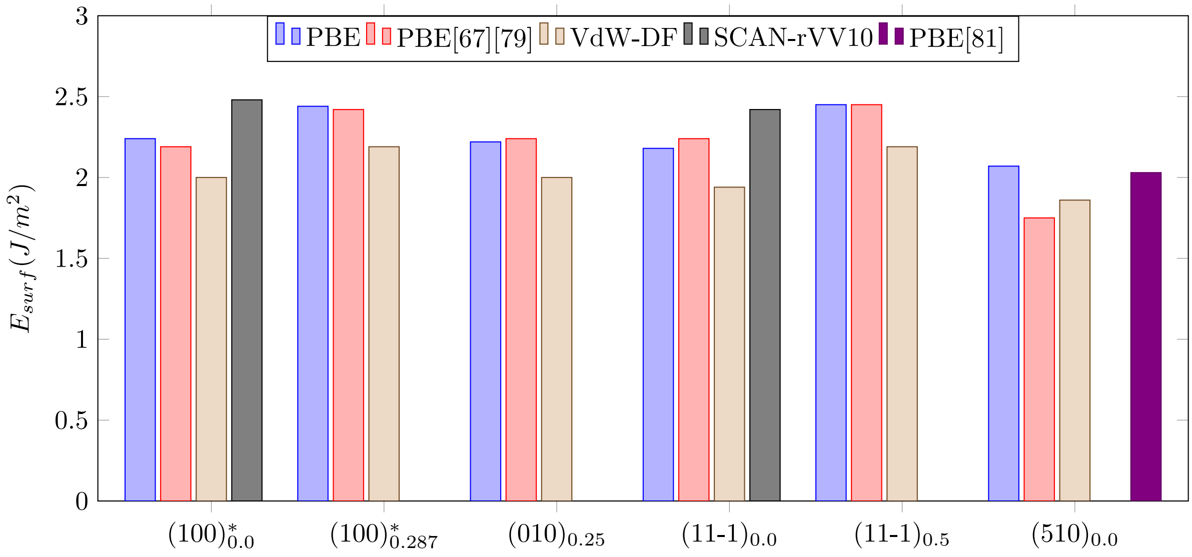

Figure 5.11: Surface energy of χ-Fe_5C_2 surfaces for PBE, VdW-DF and SCAN-rVV10 functionals and reference values. (*) Asymmetric and stoichiometric surfaces.[67][79]

As expected the surface $(100)_{0.0}$ (Fe/C=3) is more stable than $(100)_{0.287}$ (Fe/C=3.5), since it presents a lower Fe/C ratio. The bulk structure presents a Fe/C ratio of 2.5, and the non-stoichiometric surfaces studied present a higher Fe/C ratio, which explains the increase of surface energy with the increase of carbon chemical potential.

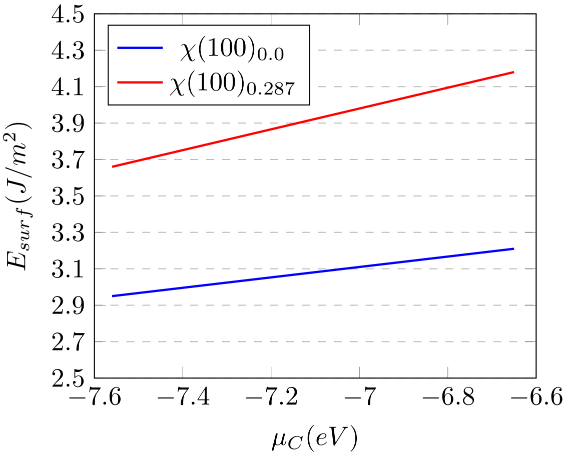

Figure 5.12: Surface energy of non-stoichiometric surfaces of χ-Fe_5C_2 with varying chemical potential of carbon. Calculated with PBE functional.

The Wulff particle was constructed and compared with values from Broos et al.[67] and Liu et al.[79]. First, the Wulff particle from Broos et al.[67] is constructed as explained in 3.3.5, and it is according to the Wulff particle in the paper. Secondly, the surface energy of $(510)_{0.0}$ from Liu et al.[79] was added to the particle, and it can be seen that the $(510)_{0.0}$ surface covers a large area of the particle. The surface $(010)_{0.25}$ intercepts the unit cell in $(0,\frac{1}{4}a,0)$ which makes the $(010)_{0.25}$ plane equal to the (040) facet.[94]

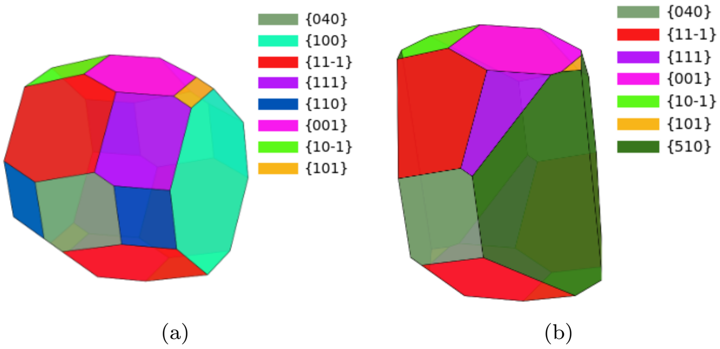

(a) (b)

Figure 5.13: Wulff particles constructed with values from Broos et al.[67] and Liu et al.[79]. (a) Wulff particle with values from Broos et al.[67], (b) Wulff particle with values from (a) and the addition of $(510)_{0.0}$ surface from Liu et al.[79]. Values from PBE functional.

Figure 5.14 represents the Wulff construction for calculated values and the values of Broos et al. and Liu et al. The inserted surfaces to make the Wulff construction were $(010)_{0.25}$, $(100)_{0.0}$, $(11\text{-}1)_{0.0}$ and $(510)_{0.0}$. The surface $(100)_{0.0}$ in figure 5.14(b) does not appear. Regardless, the calculated Wulff particle in this work is similar to the reference expectation. However, it is crucial to add enough low-energy surfaces as they can significantly alter the particle shape (figure 5.13).

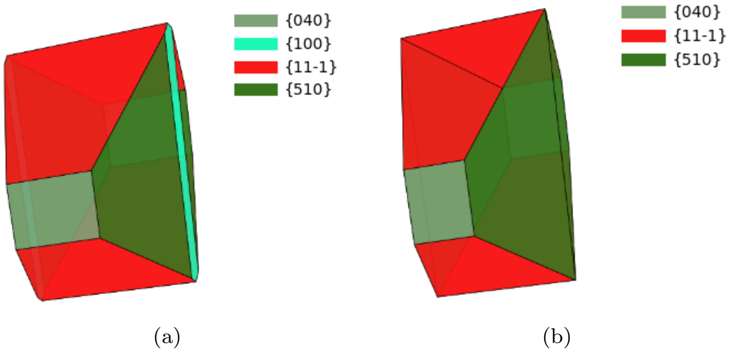

(a) (b)

Figure 5.14: χ-Fe_5C_2 Wulff Particle, (a) calculated from VASP and (b) made with [67] and [79] values. Values from PBE functional.

5.2.4 θ-Fe_3C

The θ-Fe_3C (also known as cementite) surfaces analysed were the $(010)_{0.0}$, $(101)_{0.0}$, $(110)_{0.0}$, $(111)_{0.0}$ and $(0\text{-}11)_{0.0}$, all symmetric and stoichiometric with a Fe/C ratio of 3. The carbon chemical potential analysis was not considered for these surfaces. The most stable surface calculated is the $(111)_{0.0}$ (2.37 J/m^2, PBE) for VdW-DF and PBE functionals. For Broos et al. [92], the most stable surface is the $(0\text{-}11)_{0.0}$ (2.00 J/m^2 with PBE). However, the difference between the calculated surface energy of $(111)_{0.0}$ (2.37 J/m^2, PBE) and $(0\text{-}11)_{0.0}$ (2.40 J/m^2, PBE) is less than 2%. Furthermore, the difference in surface energies between the same surface $(111)_{0.0}$ from this work and from Broos et al (2.39 J/m^2). is less than 1%. But the difference of surface energy of $(0\text{-}11)_{0.0}$ from this work and from Broos et al.[92] is 20%. The slab thickness calculated for surfaces from this work varies from 2.5 to 7.3Å, which can lead to differences in surface energies. The slab thickness of $(0\text{-}11)_{0.0}$ is 7.27Å and for $(111)_{0.0}$ it is 2.65Å, which is a significant difference and can explain why the surface energy of $(0\text{-}11)_{0.0}$ presents a big difference from the value obtained by Broos et al. for the same surface. The results can be more consistent with the literature by maintaining a similar slab thickness for all surfaces.

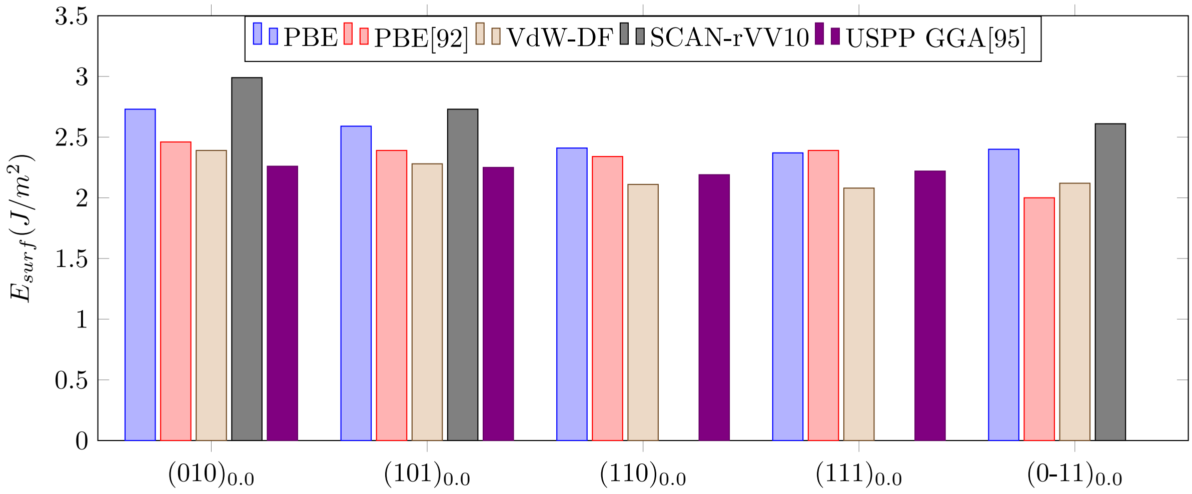

Figure 5.15: Surface energy of θ-Fe_3C surfaces for PBE, VdW-DF and SCAN-rVV10 functionals and reference values.[92][95]

The Wulff particle of θ-Fe_3C is represented in figure 5.16. The calculated Wulff particles present different visible surface areas compared with the expected surfaces from Broos et al.[92]. It is clear that the surface with high stability presents a high area in the Wulff particle.

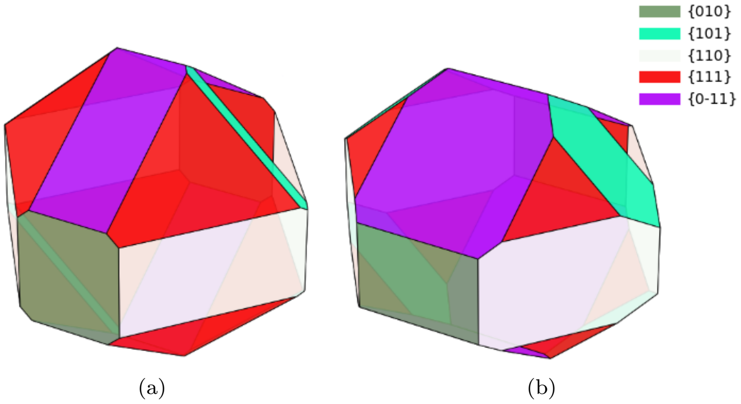

(a) (b)

Figure 5.16: θ-Fe_3C Wulff Particle, (a) calculated from VASP, and (b) made with Broos et al.[92] values. Values from PBE functional.

5.3 SCAN-rVV10 Performance

The functional SCAN-rVV10 was the most computationally expensive compared to PBE and VdW-DF. To better understand this discrepancy, for some simulations the time that one SCF loop (which is a self-consistent field loop) took was summarised in table 5.4.

Table 5.4: First SCH loop real time for 4 structure simulations with SCAN-rVV10, VdW-DF and PBE functionals.

	SCAN-rVV10		VdW-DF		PBE	
	Real time (s)	Time (h)	Real time (s)	Time (h)	Real time (s)	Time (h)
$\chi(100)_{0.287}$	28663.5	8.0	7956.5	2.2	18169.2	5.0
$\eta(001)_{0.0}$	10881.0	3.0	2505.1	0.7	2761.9	0.8
$\eta(011)_{0.0}$	27851.8	7.7	8896.8	2.5	8713.1	2.4
$\theta(101)_{0.0}$	28025.8	7.8	5726.6	1.6	6833.7	1.9

As it is seen, the first SCF loop alone takes 7 hours for most simulations of slab optimisations using the SCAN-rVV10 functional. While, for VdW-DF and PBE the first SCF loop takes no more than 2.5 h, with one exception of 5 h for PBE in $\chi(100)_{0.287}$ calculation. Even though, the first SCF loop is the longest up to 50 SCF loops are needed to achieve structural optimisation, which with SCAN-rVV10 functional can take days. So, it is very computationally expensive to use SCAN-rVV10 functional in this type of simulation.

5.4 Adsorption of molecules on χ-Fe$_5$C$_2$(510)

Adsorption of CO, C, O, H, OH and H_2O was tested on $\chi(510)_{0.0}$ sites, using the PBE functional. A smearing width of 0.2 eV, a Monkhorst-Pack grid of 4×2×1 k-points and a plane wave cut-off energy of 450 eV were used for the simulations. The electronic energies of H (eq. 5.1), O (eq. 5.2), C (eq. 5.3) and OH (eq. 5.4) were calculated following the reactions below, using the electronic energies of the known molecules (H_2, H_2O, CO).

$$\frac{1}{2}H_2 \longrightarrow H \tag{5.1}$$

$$H_2O \longrightarrow H_2 + O \tag{5.2}$$

$$CO + H_2 \longrightarrow C + H_2O \tag{5.3}$$

$$H_2O \longrightarrow \frac{1}{2}H_2 + OH \tag{5.4}$$

Table 5.5: Calculated adsorption energies (E_{ads}, eV) of molecules on $\chi(510)_{0.0}$ surface with a coverage of 1/40 ML[‡]. Calculated with PBE functional.

Sites	CO	H[*]	O[*]	C[*]	OH[*]
C4f	-1.73[†]	-2.30[†]	0.40	-0.94	-0.39[†]
F3f	-1.73[†]	-2.31	0.38	-1.24	-0.19[†]
CFb	-	-1.96[†]	-	-0.69	-
Fb	-1.97[†]	-2.31[†]	-0.10[†]	-1.46[†]	-0.19
Ct	-0.98	-1.96	0.49[†]	-0.76[†]	0.46
Ft	-	-	-	-1.46[†]	-

[*] Electronic energy calculated through the respective formation reaction.

[†] Shifts from the original position.

[‡] The coverage is the number of adsorbed species over the number of exposed layer iron atoms.[77]

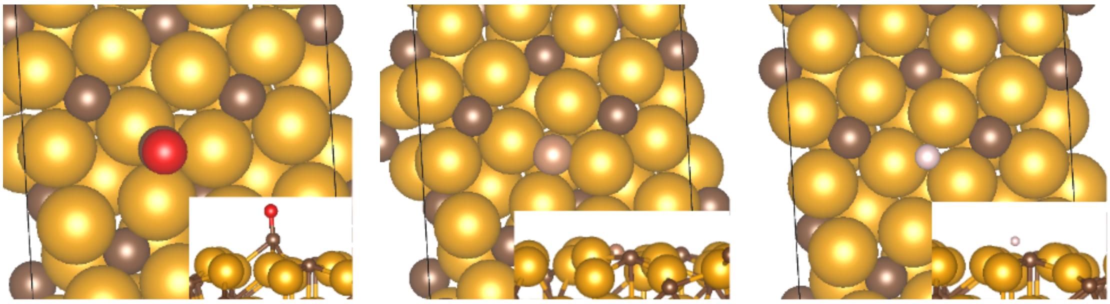

(a) CO (b) C (c) H

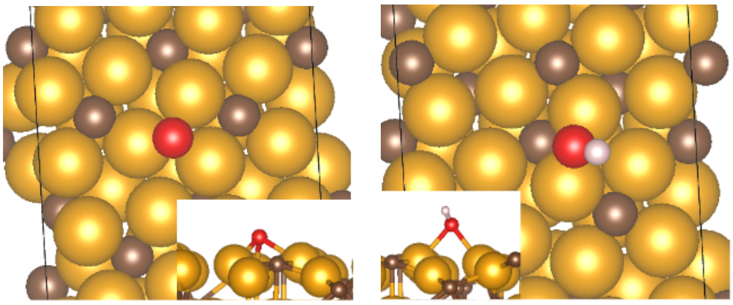

(d) O (e) OH

Figure 5.17: Most stable adsorbed molecules on $\chi(510)_{0.0}$, calculated with PBE. (b) The adsorbed carbon is a light brown colour to distinguish it from other carbon atoms from the slab.

Table 5.5 shows the adsorption energies of some molecules on different sites. Most of the adsorbed structures shifted to more stable geometries. The most stable geometries are represented in figure 5.17. The CO is most stable and adsorbed in a Fe 3-fold site with an adsorption energy of -1.97 eV. Pham et al.[81], reports an adsorption value for the same site (3F-3) of -1.99 eV. The table 5.6 shows values of CO adsorption in the 3F-3 site (notation of [81]), comparing this work's values with Pham et al. values.

Due to the calculated energies being very negative, the coverage of CO and C on this surface ($\chi(510)_{0.0}$) under FTS conditions will be high. Consistent with the high surface energy (2.07 J/m^2, PBE).

Table 5.6: Adsorption energies and structural parameters of CO on Fe 3-fold site, of this work and Pham et al.[81].

		Fe-C (Å)		E_{ads} (eV)	C-O (Å)
CO	2.13	2.104	1.867	-1.97	1.202
CO [81]	2.12	2.101	1.858	-1.99	1.201

The CO adsorption values achieved in this work are agreeable to Pham et al.'s values, with a maximum relative difference of 1.2% (in adsorption energy).

Chapter 6

Conclusions

The DFT analysis of Co- and Fe-based catalysts was the main objective of this work. For the Co-based catalyst, several reaction pathways involved in the FT process were analysed. Further, microkinetic modelling of a Co-based catalyst in a PFR reactor with CO or CO_2 feed was performed. For Fe-based catalysts, several iron carbides were studied with DFT calculations.

First, the Co-based catalyst was studied. The bulk structures analysed were FCC-C, FCC-O and HCP-O. The VdW-DF functional used to perform geometry optimisation seemed to be reliable when compared to experimental values and values from Murnaghan's equation-of-state estimation.(see section 4.1) The adsorption of CO on the top site of a Co(111) surface with 3 layers is more stable compared to the other sites. However, stability on the top site is more reliable on Co(111) slabs with more than 3 layers.

Transition states were found when performing NEB calculations on Co(111) with 3 layers. From these transition states, energy barriers and reaction energies were calculated, and an energy profile was constructed. The reaction of CO_2 hydrogenation with OH* to COOH* followed by its dissociation to CO* and OH*is the most favourable. Direct CO_2 dissociation is the most favoured among the other competing reactions. The lower the energy of the pathway to produce CO* and CH* the better, since these are monomers in FTS.

The microkinetic model for both the CO feed and CO_2 feed, and at 1 and 20 bar, proved to be favourable for methane production. However, the model was not valid anymore for higher pressures in the case of CO feed because of the high CO coverage, so a model including DFT calculations at higher CO coverage is necessary. DFT calculations of H at high coverage are needed as well to better assess the high coverage adsorption energy of H.

The Fe-based catalysts analysed were from the bulk structures χ-Fe_5C_2, ϵ-Fe_3C, η-Fe_2C and θ-Fe_3C. The analysis showed that the bulk structure with the lowest cohesive and formation energies is η-Fe_2C followed by χ-Fe_5C_2. Surfaces were analysed for each bulk structure and surface energies were calculated. The general conclusion from the surface energies analysed is that the Fe/C ratio plays an important role in surface stability, which is related to the carbon content on the surface. The surface with a high carbon content makes the surface energy decrease with an increase of the carbon chemical potential, and the opposite happens for the surfaces with low carbon content. So, carbon chemical potential also affects the surface energy, but this method of calculation, with μ_C, was only used for non-stoichiometric surfaces. When the surface has less carbon content than its bulk structure, the surface energy increases when the chemical potential increases. If the surface has more carbon content than its bulk structure, the increase in chemical potential will decrease the surface energy. Slab thickness affects surface energy as well, in $\theta - Fe_3C$ surfaces the difference in surface stability can be due to slab thickness.

The SCAN-rVV10 was the most computationally expensive functional compared to PBE and VdW-DF in all calculations. This functional is a meta GGA which presents higher chemical accuracy to calculations compared to GGA functionals according to Jacob's ladder of density functional approximations for the exchange-correlation energy. This chemical accuracy requires a higher computational cost.

The surface $(510)_{0.0}$ is the most stable surface of the $\chi - Fe_5C_2$ surfaces studied. And on this surface, the CO adsorption energy is -1.97 eV on Fe 3-fold site, called the 3F-3 site by Pham et al.[81] where the adsorption is -1.99 eV. The adsorption energy achieved has a relative difference of 1.2% compared to the value of Pham et al. From the calculated energies of other molecules (H* and C* adsorption) because they are very negative, the coverage of CO and C on this surface ($\chi(510)_{0.0}$) under FTS conditions will be high. This is to be expected from the high surface energy of this surface (2.07 J/m^2, PBE).

6.1 Future Work

The possible future work from this thesis would be to perform DFT calculations for different coverages of CO and H adsorption on the Co(111) surface and evaluate microkinetic modelling results. DFT calculation of more surfaces on the iron carbide bulk structures to evaluate more accurately the Wulff constructions. Also, to understand better which surfaces are the most stable. Perform microkinetic modelling of the Hägg carbide, to understand how it would behave under FTS conditions.

Bibliography

[1] Richard Betts. Met Office: Atmospheric CO_2 now hitting 50% higher than pre-industrial levels. World Economic Forum, March 2021. `https://www.weforum.org/agenda/2021/03/met-office-atmospheric-co2-industrial-levels-environment-climate-change/`.

[2] Samrand Saeidi, Nor Aishah Saidina Amin, and Mohammad Reza Rahimpour. Hydrogenation of CO_2 to value-added products — a review and potential future developments. *Journal of CO_2 Utilization*, 5:66–81, 2014. `https://doi.org/10.1016/j.jcou.2013.12.005`.

[3] Global greenhouse gas emissions data. US EPA - United States Environmental Protection Agency, 2022. `https://www.epa.gov/ghgemissions/global-greenhouse-gas-emissions-data`.

[4] Pires et al. Alternative jet fuel properties. *BioResources*, 13(2):2632–2657, 2018.

[5] Mohd Fadhzir Ahmad Kamaroddin, Nordin Sabli, Tuan Amran Tuan Abdullah, Shamsul Izhar Siajam, et al. Membrane-based electrolysis for hydrogen production: A review. *Membranes*, 11(11), 2021. `https://www.mdpi.com/2077-0375/11/11/810`.

[6] B. Yao, T. Xiao, O.A. Makgae, et al. Transforming carbon dioxide into jet fuel using an organic combustion-synthesized Fe-Mn-K catalyst. *Nat Commun*, 11(6395), 2020. `https://doi.org/10.1038/s41467-020-20214-z`.

[7] Liu G., Yan B., and Chen G. Technical review on jet fuel production. *Renewable and Sustainable Energy Reviews*, 25:59–70, 2013. `http://dx.doi.org/10.1016/j.rser.2013.03.025`.

[8] Aviation fuels: Technical review. Technical Report IDC 1114-099612, Chevron Products Company, 6001 Bollinger Canyon Road, San Ramon, CA 94583, 2007. `https://www.chevron.com/-/media/chevron/operations/documents/aviation-tech-review.pdf`.

[9] P. Gokulakrishnan et al. Autoignition of aviation fuels: Experimental and modeling study. *AIAA/ASME/SAE/ASEE Joint Propulsion Conference &amp*, 43rd, 2007. DOI: 10.2514/6.2007-5701.

[10] G. Freeman and A.H. Lefebvre. Spontaneous ignition characteristics of gaseous hydrocarbon-air mixtures. *Combustion and Flame*, 58(2):153–162, 1984. `https://doi.org/10.1016/0010-2180(84)90090-7`.

[11] L. J. Spadaccini and J. A. TeVelde. Autoignition characteristics of aircraft-type fuels. Technical Report NASA CR-159886, United Technologies Research Center, East Hartford, CT, 1980.

[12] S. S. Vasu, D. F. Davidson, and R. K. Hanson. Shock tube ignition delay times and modeling of jet fuel mixtures. AIAA-2006-4402, 42nd AIAA/ASME/SAE/ASEE Joint Propulsion Conference and Exhibit, Sacramento, CA, 2006.

[13] A.K. Dalai, V.V. Goud, S. Nanda, and V.B. Borugadda. *Algal Biorefinery: Developments, Challenges and Opportunities*, chapter 8. Routledge Studies in Bioenergy. Taylor & Francis, 2021. ISBN: 978-1-000-41083-9, `https://books.google.be/books?id=lBMtEAAAQBAJ`.

[14] M. Garba, M. Usman, S. Khan, et al. CO_2 towards fuels: A review of catalytic conversion of carbon dioxide to hydrocarbons. *Journal of Environmental Chemical Engineering*, 2020. `http://dx.doi.org/10.1039/C7RA13546G`.

[15] Brandon Han Hoe Goh, Cheng Tung Chong, Hwai Chyuan Ong, Tine Seljak, et al. Recent advancements in catalytic conversion pathways for synthetic jet fuel produced from bioresources. *Energy Conversion and Management*, 251:114974, 2022. `https://doi.org/10.1016/j.enconman.2021.114974`.

[16] C. Gutiérrez-Antonio, F.I. Gómez-Castro, J.A. de Lira-Flores, and S. Hernández. A review on the production processes of renewable jet fuel. *Renewable and Sustainable Energy Reviews*, 79:709–729, 2017. `https://doi.org/10.1016/j.rser.2017.05.108`.

[17] HEFA/HVO, hydroprocessed esters and fatty acids. f3 centre, 2016. `https://f3centre.se/en/fact-sheets/hefa-hvo-hydroprocessed-esters-and-fatty-acids/`.

[18] Susan van Dyk and Jack Saddler. Progress in commercialization of biojet/sustainable aviation fuels (SAF): Technologies, potential and challenges. IEA Bioenergy: Task 39, May 2021. `https://task39.sites.olt.ubc.ca/files/2021/08/Task-39-Progress-in-the-commercialisation-of-biojet-fuels-FINAL-August-2021.pdf`.

[19] José L. C. Fajín, M. Natália D. S. Cordeiro, and José R. B. Gomes. Fischer-tropsch synthesis on multicomponent catalysts: What can we learn from computer simulations? *Catalysts*, 5:3–17, 2015. doi:10.3390/catal5010003.

[20] P. Gao, L. Zhang, S. Li, et al. Novel heterogeneous catalysts for CO_2 hydrogenation to liquid fuels. *ACS Central Science*, 6(10):1657–1670, 2020. `https://doi.org/10.1021/acscentsci.0c00976`.

[21] W. Li, H. Wang, X. Jiang, et al. A short review of recent advances in CO_2 hydrogenation to hydrocarbons over heterogeneous catalysts. *RSC Adv.*, 8:7651–7669, 2018. `http://dx.doi.org/10.1039/C7RA13546G`.

[22] Philipp Kaiser, Rajabhau-Bajirao Unde, Christoph Kern, and Andreas Jess. Production of Liquid Hydrocarbons with CO_2 as Carbon Source based on Reverse Water-Gas Shift and Fischer-Tropsch Synthesis. *Chemie Ingenieur Technik*, 85(4):489–499. `https://doi.org/10.1002/cite.201200179`.

[23] H. Mansour and E. Iglesia. Mechanistic connections between CO_2 and CO hydrogenation on dispersed ruthenium nanoparticles. *Journal of the American Chemical Society*, 143 (30):11582–11594, 2021. DOI: 10.1021/jacs.1c04298.

[24] MK. Khan, P. Butolia, et al. Selective conversion of carbon dioxide into liquid hydrocarbons and long-chain α-olefins over Fe-amorphous AlO_x bifunctional catalysts. *ACS Catalysis*, 10(18):10325–10338, 2020. `https://doi.org/10.1021/acscatal.0c02611`.

[25] Phathutshedzo R. Khangale. Hydrogenation of CO_2 to hydrocarbons over zirconia-supported cobalt catalyst promoted with potassium. *Catalysis Letters*, 2021. `https://doi.org/10.1007/s10562-021-03849-5`.

[26] RP. Ye, J. Ding, W. Gong, et al. CO_2 hydrogenation to high-value products via heterogeneous catalysis. *Nat Commun*, 10(5698), 2019. `https://doi.org/10.1038/s41467-019-13638-9`.

[27] I. Yarulina, A.D. Chowdhury, F. Meirer, et al. Recent trends and fundamental insights in the methanol-to-hydrocarbons process. *Nature Catalysis*, 1:398–411, 2018. `https://doi.org/10.1038/s41929-018-0078-5`.

[28] K. Cheng, J. Kang, L.D. King, et al. Advances in catalysis for syngas conversion to hydrocarbons. *Advances in Catalysis*, 60, 2017. `https://doi.org/10.1016/bs.acat.2017.09.003`.

[29] J.G. Speight. 9 - coal gasification processes for synthetic liquid fuel production. In Rafael Luque and James G. Speight, editors, *Gasification for Synthetic Fuel Production*, Woodhead Publishing Series in Energy, pages 201–220. Woodhead Publishing, 2015. ISBN: 978-0-85709-802-3, `https://doi.org/10.1016/B978-0-85709-802-3.00009-6`.

[30] Kang Cheng, Jincan Kang, David L. King, Vijayanand Subramanian, Cheng Zhou, Qinghong Zhang, and Ye Wang. Chapter Three - Advances in Catalysis for Syngas Conversion to Hydrocarbons. volume 60 of *Advances in Catalysis*, pages 125–208. Academic Press, 2017. `https://doi.org/10.1016/bs.acat.2017.09.003`.

[31] G. Prieto. Carbon dioxide hydrogenation into higher hydrocarbons and oxygenates: Thermodynamic and kinetic bounds and progress with heterogeneous and homogeneous catalysis. *ChemSusChem*, 10(6):1056–1070, 2017. DOI:10.1002/cssc.201601591.

[32] Marlin D.S., Sarron E., and Sigurbjörnsson Ó. Process advantages of direct CO_2 to methanol synthesis. *Front. Chem.*, 6(446), 2018. `https://doi.org/10.3389/fchem.2018.00446`.

[33] R. Satthawong, N. Koizumi, C. Song, and P. Prasassarakich. Bimetallic Fe–Co catalysts for CO_2 hydrogenation to higher hydrocarbons. *Journal of CO_2 Utilization*, 3–4:102–106, 2013. `http://dx.doi.org/10.1016/j.jcou.2013.10.002`.

[34] Kasun Thanthrige. *Theoretical Study of the Mechanism and Microkinetics of Cobalt-Catalyzed Fischer-Tropsch Synthesis*. PhD thesis, Universiteit Gent, Laboratorium voor Chemische Techniek, Technologiepark 914, B-9052 Gent, België, 2018.

[35] C.G. Visconti, M. Martinelli, L. Falbo, L. Fratalocchi, et al. CO_2 hydrogenation to hydrocarbons over Co and Fe-based Fischer-Tropsch catalysts. *Catalysis Today*, 277:161–170, 2016. `http://dx.doi.org/10.1016/j.cattod.2016.04.010`.

[36] C. Vogt, E. Groeneveld, G. Kamsma, et al. Unravelling structure sensitivity in CO_2 hydrogenation over nickel. *Nature Catalysis*, 1:127–134, 2018. `https://doi.org/10.1038/s41929-017-0016-y`.

[37] Jian Wei, Qingjie Ge, Ruwei Yao, et al. Directly converting CO_2 into a gasoline fuel. *Nature Communications*, 8:15174, 2017. `https://doi.org/10.1038/ncomms15174`.

[38] Zhenhong He, Meng Cui, Qingli Qian, Jingjing Zhang, Huizhen Liu, and Buxing Han. Synthesis of liquid fuel via direct hydrogenation of CO_2. *Proceedings of the National Academy of Sciences*, 116(26):12654–12659, 2019. DOI:10.1073/pnas.1821231116.

[39] Rhodri E. Owen, Pawel Plucinski, Davide Mattia, Laura Torrente-Murciano, Valeska P. Ting, and Matthew D. Jones. Effect of support of Co-Na-Mo catalysts on the direct conversion of CO_2 to hydrocarbons. *Journal of CO2 Utilization*, 16:97–103, 2016. `https://doi.org/10.1016/j.jcou.2016.06.009`.

[40] Yo Han Choi, Youn Jeong Jang, Hunmin Park, Won Young Kim, Young Hye Lee, Sun Hee Choi, and Jae Sung Lee. Carbon dioxide Fischer-Tropsch synthesis: A new path to carbon-neutral fuels. *Applied Catalysis B: Environmental*, 202:605–610, 2017. `https://doi.org/10.1016/j.apcatb.2016.09.072`.

[41] T.A. Le, M.S. Kim, S.H. Lee, et al. CO and CO_2 methanation over supported Ni catalysts. *Catalysis Today*, 293-294:89–96, 2017. `https://doi.org/10.1016/j.cattod.2016.12.036`.

[42] C. Vogt, M. Monai, E.B. Sterk, et al. Understanding carbon dioxide activation and carbon–carbon coupling over nickel. *Nature Communications*, 10(5330), 2019. `https://doi.org/10.1038/s41467-019-12858-3`.

[43] A.L. Tarasov, V.I. Isaeva, O.P. Tkachenko, V.V. Chernyshev, and L.M. Kustov. Conversion of CO_2 into liquid hydrocarbons in the presence of a Co-containing catalyst based on the microporous metal-organic framework MIL-53(Al). *Fuel Processing Technology*, 176:101–106, 2018. `https://doi.org/10.1016/j.fuproc.2018.03.016`.

[44] V. I. Isaeva, O. L. Eliseev, R. V. Kazantsev, V. V. Chernyshev, P. E. Davydov, B. R. Saifutdinov, A. L. Lapidus, and L. M. Kustov. Fischer–Tropsch synthesis over MOF-supported cobalt catalysts (Co@MIL-53(Al)). *Dalton Trans.*, 45:12006–12014, 2016. `http://dx.doi.org/10.1039/C6DT01394E`.

[45] Z. Shia, H. Yang, P. Gaoa, X. Lia, et al. Direct conversion of CO_2 to long-chain hydrocarbon fuels over K–promoted CoCu/TiO_2 catalysts. *Catalysis Today*, 311:65–73, 2018. `http://dx.doi.org/10.1016/j.cattod.2017.09.053`.

[46] Matthias Albrecht, Uwe Rodemerck, Matthias Schneider, Martin Bröring, Dirk Baabe, and Evgenii V. Kondratenko. Unexpectedly efficient CO_2 hydrogenation to higher hydrocarbons over non-doped Fe_2O_3. *Applied Catalysis B: Environmental*, 204:119–126, 2017. `https://doi.org/10.1016/j.apcatb.2016.11.017`.

[47] Jian Wei, Jian Sun, Zhiyong Wen, Chuanyan Fang, Qingjie Ge, and Hengyong Xu. New insights into the effect of sodium on Fe_3O_4- based nanocatalysts for CO_2 hydrogenation to light olefins. *Catal. Sci. Technol.*, 6:4786–4793, 2016. DOI: 10.1039/C6CY00160B.

[48] Wei Zhou, Kang Cheng, Jincan Kang, Cheng Zhou, Vijayanand Subramanian, Qinghong Zhang, and Ye Wang. New horizon in C1 chemistry: breaking the selectivity limitation in transformation of syngas and hydrogenation of CO_2 into hydrocarbon chemicals and fuels. *Chem. Soc. Rev.*, 48:3193–3228, 2019. DOI: 10.1039/C8CS00502H.

[49] Xu Cui, Peng Gao, Shenggang Li, Chengguang Yang, Ziyu Liu, Hui Wang, Liangshu Zhong, and Yuhan Sun. Selective Production of Aromatics Directly from Carbon Dioxide Hydrogenation. *ACS Catalysis*, 9(5):3866–3876, 2019. `https://doi.org/10.1021/acscatal.9b00640`.

[50] P. Gao, S. Li, X. Bu, et al. Direct conversion of CO_2 into liquid fuels with high selectivity over a bifunctional catalyst. *Nature Chem*, 9:1019–1024, 2017. `https://doi.org/10.1038/nchem.2794`.

[51] Commercial airlines: worldwide fuel consumption 2005-2022 — statista. Online in Statista, October 2021. `https://www.statista.com/statistics/655057/fuel-consumption-of-airlines-worldwide/`.

[52] Jacopo Prisco. Green jet fuel is here – so why are airlines not using it? CNN, April 2022. `https://edition.cnn.com/travel/article/saf-jet-fuel-green/index.html`.

[53] Martina Igini. 4 sustainable aviation fuel companies leading the way to net-zero flying. Earth.Org, March 2022. `https://earth.org/sustainable-aviation-fuel-companies/`.

[54] Technology – SkyNRG. SkyNRG, 2022. `https://skynrg.com/sustainable-aviation-fuel/technology/`.

[55] Ausilio Bauen, Niccolò Bitossi, Lizzie German, Anisha Harris, and Khangzhen Leow. Sustainable aviation fuels : Status, challenges and prospects of drop-in liquid fuels, hydrogen and electrification in aviation. *Johnson Matthey Technology Review*, 64(3):263–278, 2020. `https://doi.org/10.1595/205651320X15816756012040`.

[56] Synkero (SkyNRG Amsterdam) – SkyNRG. SkyNRG, 2022. `https://skynrg.com/producing-saf/saf-production-plant-in-the-port-of-amsterdam/`.

[57] SkyNRG Delfzijl (DSL-01) – SkyNRG. SkyNRG, 2022. `https://skynrg.com/producing-saf/skynrgs-production-facility-in-the-netherlands/`.

[58] SkyNRG Pacific Northwest – SkyNRG. SkyNRG, 2022. `https://skynrg.com/producing-saf/skynrg-pacific-northwest/`.

[59] John Kitchin. Modeling materials using density functional theory. *Boston, Free Software Foundation*, 2008.

[60] V. Sahni. The hohenberg-kohn theorems and kohn-sham density functional theory. *Quantal Density Functional Theory*, page 99–123, 2004. doi:10.1007/978-3-662-09624-6_4.

[61] Vinod Kumar Jain, Sunita Rattan, and Abhishek Verma, editors. *Recent Trends in Materials and Devices: Proceedings of ICRTMD 2019*, volume 256 of *Springer Proceedings in Physics*. Springer Singapore, 2019. `https://doi.org/10.1007/978-981-15-8625-5`.

[62] Janice A. Steckel David S. Sholl. *Density Functional Theory: A Practical Introduction.* John Wiley & Sons, Inc., March 2009. ISBN:9780470373170, DOI:10.1002/9780470447710.

[63] Georg Kresse, Martijn Marsman, and Jürgen Furthmüller. VASP the GUIDE. Computational Physics, Faculty of Physics, Universität Wien, April 2009. `https://www.smcm.iqfr.csic.es/docs/vasp/`.

[64] New tier-2 cluster doduo. Universiteit Gent, April 2021. `https://www.ugent.be/hpc/en/news-events/news/doduo`.

[65] ASE-developers. About — ASE documentation. Wiki.fysik.dtu.dk, 2022. `https://wiki.fysik.dtu.dk/ase/about.html`.

[66] Maarten de Jong, Wei Chen, Thomas Angsten, Anubhav Jain, Randy Notestine, Anthony Gamst, Marcel Sluiter, Chaitanya Krishna Ande, Sybrand van der Zwaag, Jose J Plata, Cormac Toher, Stefano Curtarolo, Gerbrand Ceder, Kristin A. Persson, and Mark Asta. Charting the complete elastic properties of inorganic crystalline compounds. *Scientific Data*, 2, March 2015. DOI:10.1038/sdata.2015.9, `http://perssongroup.lbl.gov/papers/sdata2015-elasticprops.pdf`.

[67] Robin J. P. Broos, Bart Zijlstra, Ivo A. W. Filot, and Emiel J. M. Hensen. Quantum-chemical DFT study of direct and H- and C-assisted CO dissociation on the χ-Fe_5C_2 Hägg Carbide. *The Journal of Physical Chemistry C*, 122(18):9929–9938, 2018. DOI: 10.1021/acs.jpcc.8b01064.

[68] Georg K. H. Madsen. Functional form of the generalized gradient approximation for exchange: The PBEα functional. *Phys. Rev. B*, 75:195108, May 2007. `https://link.aps.org/doi/10.1103/PhysRevB.75.195108`.

[69] M. Dion, H. Rydberg, E. Schröder, D. C. Langreth, and B. I. Lundqvist. Van der Waals density functional for general geometries. *Phys. Rev. Lett.*, 92:246401, Jun 2004. `https://link.aps.org/doi/10.1103/PhysRevLett.92.246401`.

[70] Haowei Peng, Zeng-Hui Yang, John P. Perdew, and Jianwei Sun. Versatile van der Waals density functional based on a meta-generalized gradient approximation. *Phys. Rev. X*, 6:041005, Oct 2016. `https://link.aps.org/doi/10.1103/PhysRevX.6.041005`.

[71] V.G. Tyuterev and Nathalie Vast. Murnaghan's equation of state for the electronic ground state energy. *Computational Materials Science*, 38(2):350–353, 2006. `https://doi.org/10.1016/j.commatsci.2005.08.012`.

[72] Max C. Holthausen Wolfram Koch. *A Chemist's Guide to Density Functional Theory*, chapter 8. Wiley-VCH Verlag GmbH, second edition, 2001. ISBNs: 3-527-30372-3 (Softcover); 3-527-60004-3 (Electronic).

[73] Transition state tools for VASP-VTST. Theory.cm.utexas.edu. `https://theory.cm.utexas.edu/vtsttools/index.html`.

[74] Lakshmikanth K. G, Ishak Kundappaden, and Raghu Chatanathodi. A DFT study of CO adsorption on pt (111) using van der waals functionals. *Surface Science*, 681:143–148, 2019. `https://doi.org/10.1016/j.susc.2018.12.001`.

[75] W. Gao, Y. Chen, B. Li, et al. Determining the adsorption energies of small molecules with the intrinsic properties of adsorbates and substrates. *Nat Commun*, 11(1196), 2020. `https://doi.org/10.1038/s41467-020-14969-8`.

[76] Rahm et al. WulffPack: A python package for Wulff constructions. *Journal of Open Source Software*, 5(45), 2020. `https://doi.org/10.21105/joss.01944`.

[77] Shu Zhao, Xing-Wu Liu, Chun-Fang Huo, Yong-Wang Li, Jianguo Wang, and Haijun Jiao. Determining surface structure and stability of ϵ-Fe_2C, χ-Fe_5C_2, θ-Fe_3C and Fe_4C phases under carburization environment from combined DFT and atomistic thermodynamic studies. *Catalysis, Structure & Reactivity*, 1(1):44–60, 2015. DOI: 10.1179/2055075814Y.0000000007.

[78] NIST Chemistry WebBook. National Institute of Standards and Technology (NIST); Webbook.nist.gov. `https://doi.org/10.18434/T4D303`.

[79] Qian-Yu Liu, Cheng Shang, and Zhi-Pan Liu. In situ active site for CO activation in Fe-catalyzed fischer–tropsch synthesis from machine learning. *Journal of the American Chemical Society*, 143(29):11109–11120, 2021. DOI: 10.1021/jacs.1c04624.

[80] Shu Zhao, Xing-Wu Liu, Chun-Fang Huo, Yong-Wang Li, Jianguo Wang, and Haijun Jiao. Surface morphology of Hägg iron carbide (χ-Fe_5C_2) from ab initio atomistic thermodynamics. *Journal of Catalysis*, 294:47–53, 2012. `https://doi.org/10.1016/j.jcat.2012.07.003`.

[81] Thanh Hai Pham, Xuezhi Duan, Gang Qian, Xinggui Zhou, and De Chen. CO activation pathways of Fischer–Tropsch synthesis on χ-Fe_5C_2 (510): Direct versus hydrogen-assisted CO dissociation. *The Journal of Physical Chemistry C*, 118(19):10170–10176, 2014. DOI: 10.1021/jp502225r.

[82] I.A.W. Filot. *Introduction to microkinetic modeling.* Technische Universiteit Eindhoven, December 2018.

[83] Neil W Ashcroft and N David Mermin. *Solid state physics.* Saunders College, 1976.

[84] Michael J. Mehl and Dimitrios A. Papaconstantopoulos. Applications of a tight-binding total-energy method for transition and noble metals: Elastic constants, vacancies, and surfaces of monatomic metals. *Physical Review B*, 54(7):4519–4530, 1996. DOI: 10.1103/physrevb.54.4519.

[85] Pieter van Helden, Ionel M. Ciobîcă, and Roelof L.J. Coetzer. The size-dependent site composition of FCC cobalt nanocrystals. *Catalysis Today*, 261:48–59, 2016. `https://doi.org/10.1016/j.cattod.2015.07.052`.

[86] H. Papp. The chemisorption of carbon monoxide on a Co(0001) single crystal surface; studied by LEED, UPS, EELS, AES and work function measurements. *Surface Science*, 129(1):205–218, 1983. `https://doi.org/10.1016/0039-6028(83)90103-6`.

[87] Katsutoshi Hyodo, Shinji Munetoh, and Toshihiro Tsuchiyama. Empirical interatomic potential for Fe-C system using original Finnis-Sinclair potential function. *Computational Materials Science*, 184:109871, 2020. `https://doi.org/10.1016/j.commatsci.2020.109871`.

[88] Sigemaro Nagakura. Study of metallic carbides by electron diffraction part III. iron carbides. *Journal of the Physical Society of Japan*, 14(2):186 – 195, 1959. DOI: 10.1143/JPSJ.14.186.

[89] Y. Hirotsu and S. Nagakura. Crystal structure and morphology of the carbide precipitated from martensitic high carbon steel during the first stage of tempering. *Acta Metallurgica*, 20(4):645–655, 1972. `https://doi.org/10.1016/0001-6160(72)90020-X`.

[90] K. JACK and S. WILD. Nature of χ-carbide and its possible occurrence in steels. *Nature*, 212:248–250, 1966. `https://doi.org/10.1038/212248b0`.

[91] H.P. Scott, Q. Williams, and E. Knittle. Stability and equation of state of Fe_3C to 73 GPa: Implications of carbon in the earth's core. *Geophysical Research Letters*, 28(9):1875 – 1878, 2001. DOI: 10.1029/2000GL012606.

[92] Robin Johannes Petrus Broos. *Computational modelling of the Fischer-Tropsch reaction on iron carbides*. PhD thesis, Chemical Engineering and Chemistry, February 2020. Proefschrift.

[93] Li li BAO, Chun fang HUO, Chun mei DENG, and Yong wang LI. Structure and stability of the crystal Fe_2C and low index surfaces. *Journal of Fuel Chemistry and Technology*, 37(1):104–108, 2009. `https://doi.org/10.1016/S1872-5813(09)60012-8`.

[94] Milton Ohring. 3 - structure of solids. In Milton Ohring, editor, *Engineering Materials Science*, pages 71–IV. Academic Press, San Diego, 1995. `https://doi.org/10.1016/B978-012524995-9/50027-1`.

[95] Wun C Chiou and Emily A Carter. Structure and stability of Fe_3C-cementite surfaces from first principles. *Surface Science*, 530(1):88–100, 2003. `https://doi.org/10.1016/S0039-6028(03)00352-2`.

Appendix A

Methods

Iron Carbides Modelling

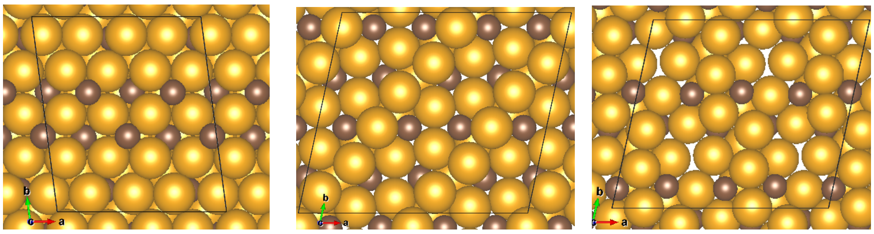

(a) $(010)_{0.25}$ (b) $(11\bar{1})_{0.0}$ (c) $(11\bar{1})_{0.5}$

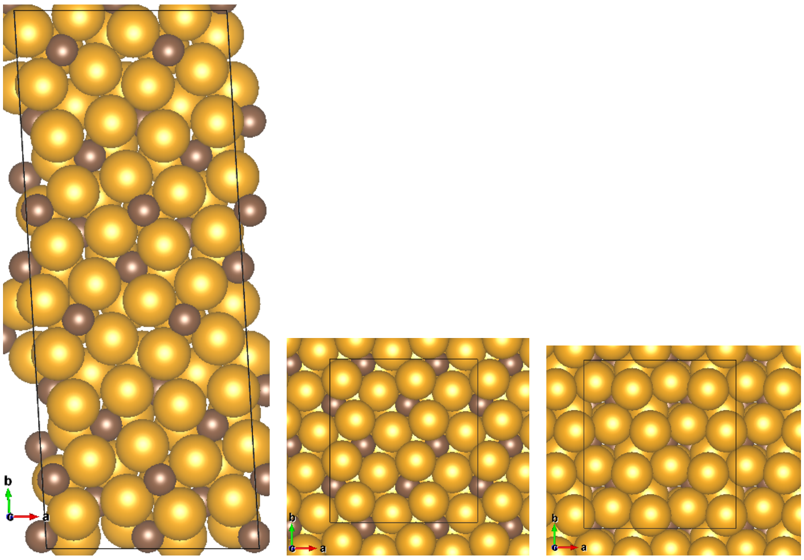

(d) $(510)_{0.0}$ (e) $(100)_{0.0}$ (f) $(100)_{0.287}$

Figure A.1: Top view of slab surfaces of Hägg Carbide (χ-Fe_5C_2).

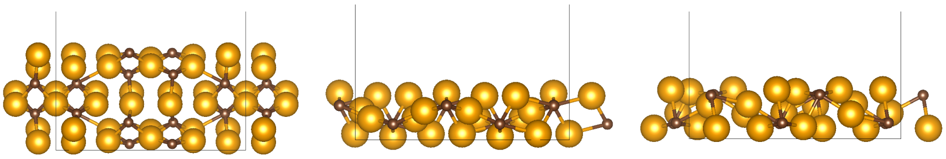

(a) $(010)_{0.25}$ (b) $(11\bar{1})_{0.0}$ (c) $(11\bar{1})_{0.5}$

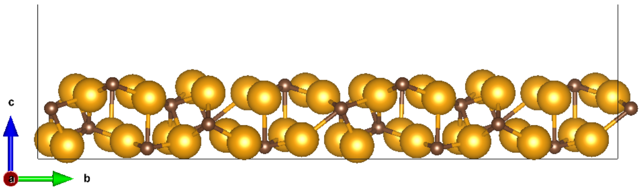

(d) $(510)_{0.0}$

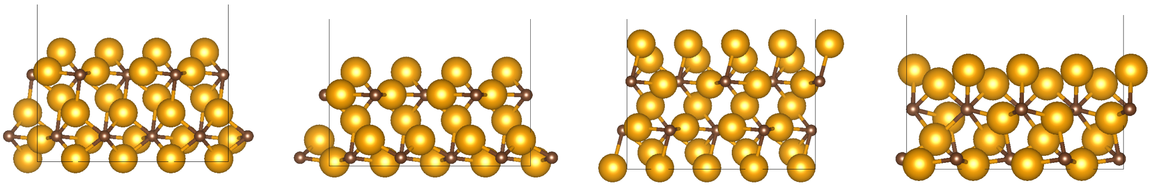

(e) $(100)_{0.0}$ (f) $(100)^*_{0.0}$ (g) $(100)_{0.287}$ (h) $(100)^*_{0.287}$

Figure A.2: Side view of slab surfaces of Hägg Carbide (χ-Fe_5C_2).

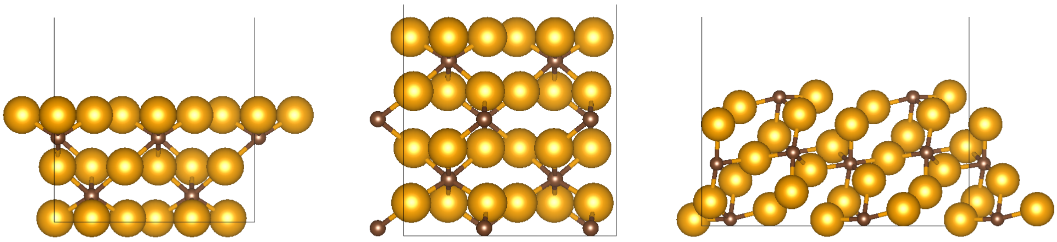

(a) $(001)_{0.0}$ (b) $(001)^*_{0.0}$ (c) $(011)_{0.0}$

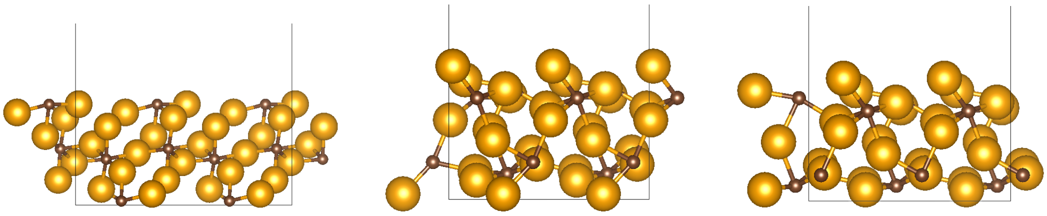

(d) $(011)^*_{0.0}$ (e) $(101)_{0.0}$ (f) $(101)^*_{0.0}$

Figure A.3: Side view of slab surfaces of constructed ϵ-Fe_3C.

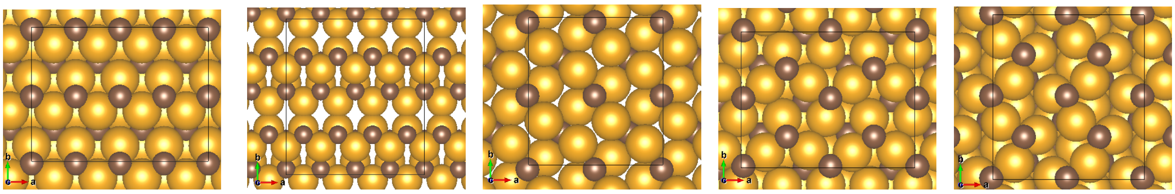

(a) $(001)_{0.0}$ (b) $(011)_{0.0}$ (c) $(100)_{0.0}$ (d) $(101)_{0.0}$ (e) $(110)_{0.0}$

Figure A.4: Top view of slab surfaces constructed of η-Fe_2C.

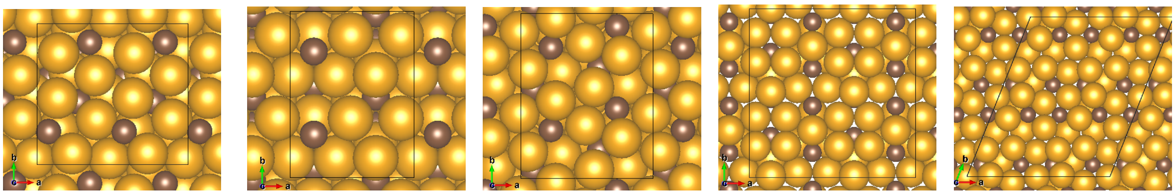

(a) $(0\bar{1}1)_{0.0}$ (b) $(010)_{0.0}$ (c) $(101)_{0.0}$ (d) $(110)_{0.0}$ (e) $(111)_{0.0}$

Figure A.5: Top view of slab surfaces constructed of θ-Fe_3C.

VASP Calculations

Table A.1: Electronic energies of some species in gas phase and calculated from a dissociation. Values obtained with PBE functional.

PBE	E (eV)
H_2	-6.77
H_2O	-14.22
CO	-14.78
C	-1.29
C from CO	-7.33
O	-1.90
O from H_2O	-7.45
O from CO	-7.45
O from CO_2	-8.179
CO_2	-22.958
OH from H_2O	-10.83
OH	-7.73

Table A.2: Electronic energies calculated from VASP of Fe and C atom in gas phase, and all bulk structures studied.

	Electronic energy VASP (eV)						
Functional	E_{Fe}^{gas} (eV)	E_{Fe}^{gs} (eV)	E_{C}^{gas}(eV)	$\epsilon - Fe_3C$	$\eta - Fe_2C$	$\chi - Fe_5C_2$	$\theta - Fe_3C$
PBE	-3.26	-8.26	-1.29	-67.65	-51.22	-237.79	-135.34
VdW-DF	0.38	-3.86	-0.06	-37.58	-29.95	-134.45	-74.86
SCAN-rVV10	-13.11	-17.90	-1.91	-126.84	-90.91	-435.73	-253.65

Table A.3: Carbon chemical potential values for several CO partial pressures. At 0.1 MPa total pressure and 523 K.

p_{CO} (MPa)	μ_C (eV)
0.2	-6.72
0.3	-6.70
0.5	-6.67
0.7	-6.66
0.83	-6.65
0.9	-6.65
1	-6.64
1.2	-6.63
1.3	-6.63
1.5	-6.62

Appendix B

Results

Gas Phase

Table B.1: Gas phase molecules $E0$ values from VASP calculations with VdW-DF and PBE functionals.

Gas Phase	E0 (eV)	
Molecules	VdW-DF	PBE
O_2	-5.72	-9.85
H_2	-7.06	-6.77
H_2O	-12.19	-14.22
CO	-11.35	-14.78
CO_2	-17.14	-22.96
CH_4	-22.59	-24.04
CH_3OH	-26.59	-30.21
CH_2O	-18.61	-22.13
C	-0.06	-1.29
H	-1.01	-1.11
O	0.23	-1.90
OH	-5.87	-7.73
CH	-4.52	-
CH_2	-10.61	-
CH_3	-16.75	-
HCO	-13.50	-
COH	-11.60	-
COOH	-18.61	-
HCOH	-15.08	-
HCOO	-17.16	-
HCOOH	-24.02	-

Cobalt Results

Figure B.1: VESTA representation of adsorbed CO over Co(111) on several active sites.

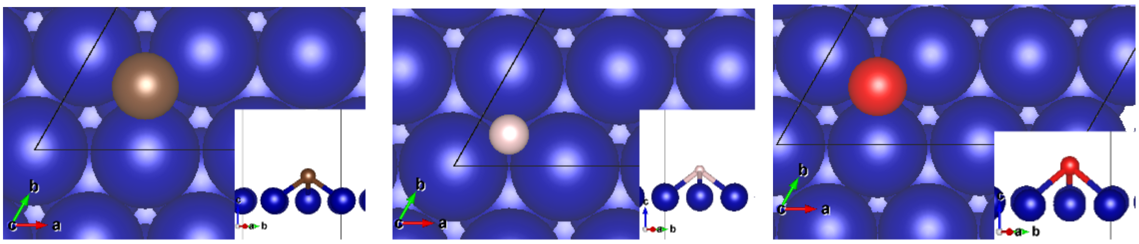

(a) C (hcp)

(b) H (fcc)

(c) O (hcp)

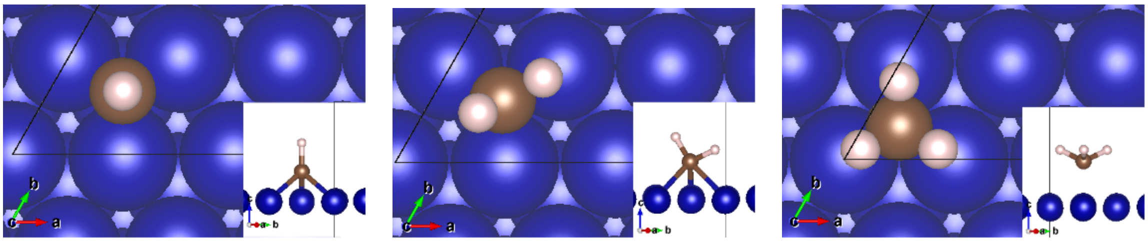

(d) CH (hcp)

(e) CH_2 (hcp)

(f) CH_3 (fcc)

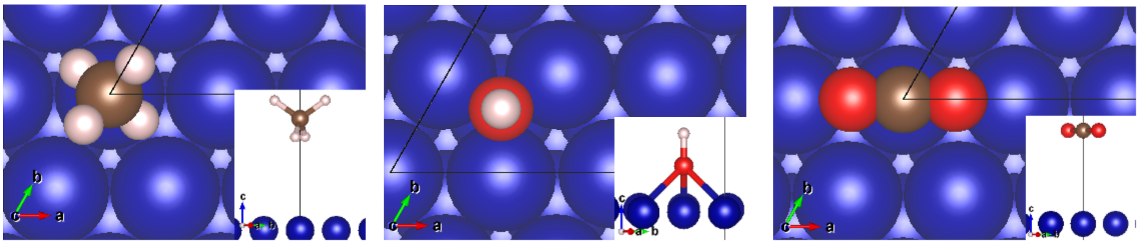

(g) CH_4 (top)

(h) OH (hcp)

(i) CO_2 (top)

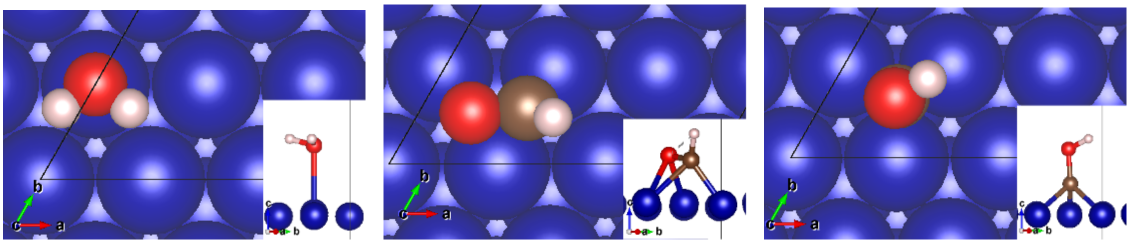

(j) H_2O (fcc)

(k) HCO (hcp)

(l) COH (hcp)

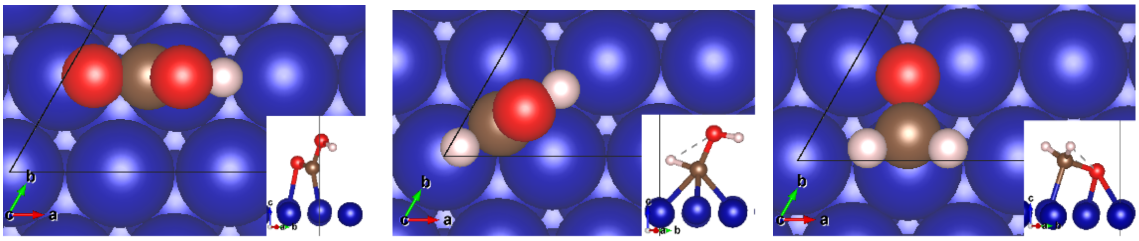

(m) COOH (top)

(n) HCOH (fcc)

(o) H_2CO (hcp)

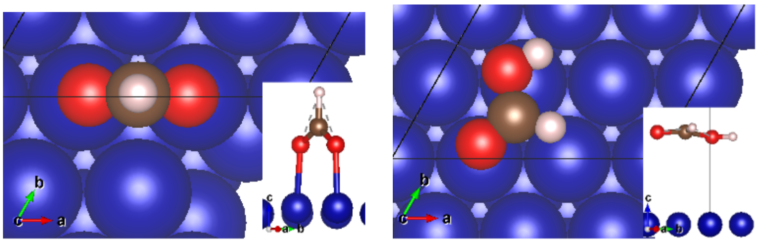

(p) HCOO (top)

(q) HCOOH

Figure B.2: Initial Sate, Transition State and Final State, respectively, of low coverage CO_2 reactions over Co(111).

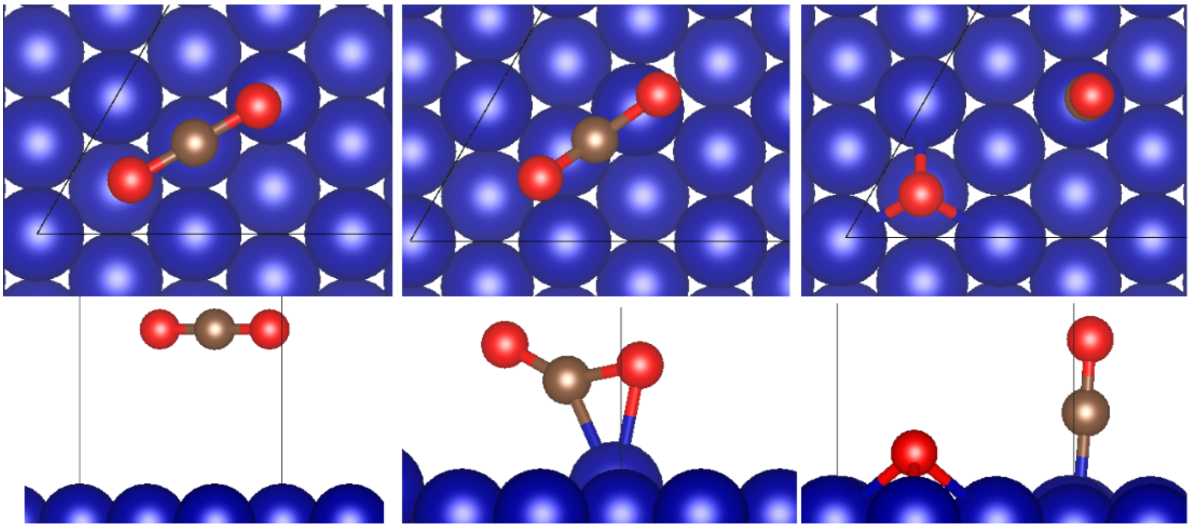

(a) $CO_2 + 2^* \longrightarrow CO^* + O^*$

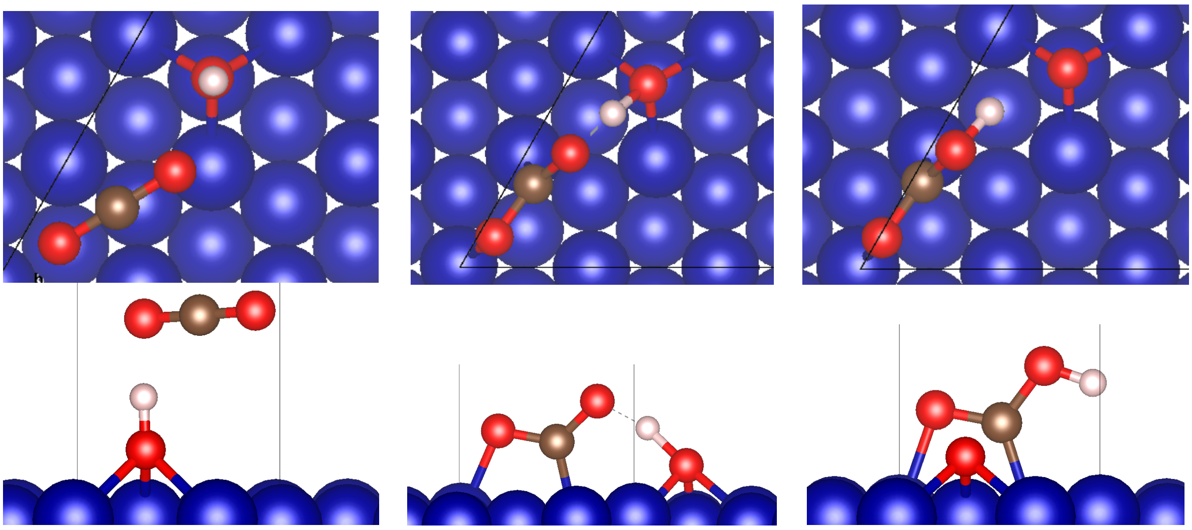

(b) $CO_2 +^* +OH^* \longrightarrow COOH^* + O^*$

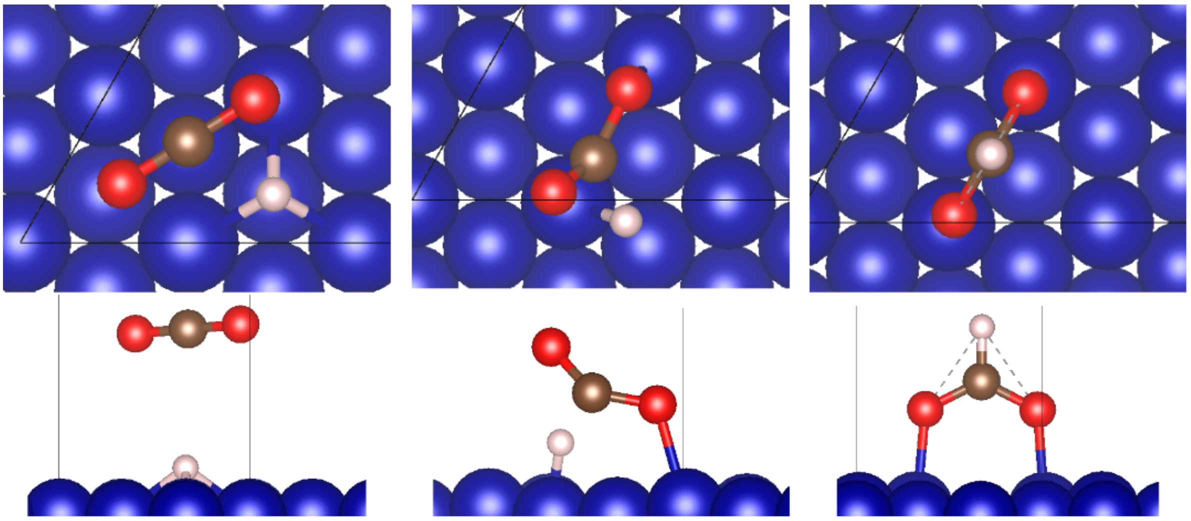

(c) $CO_2 + H^* \longrightarrow HCOO^*$

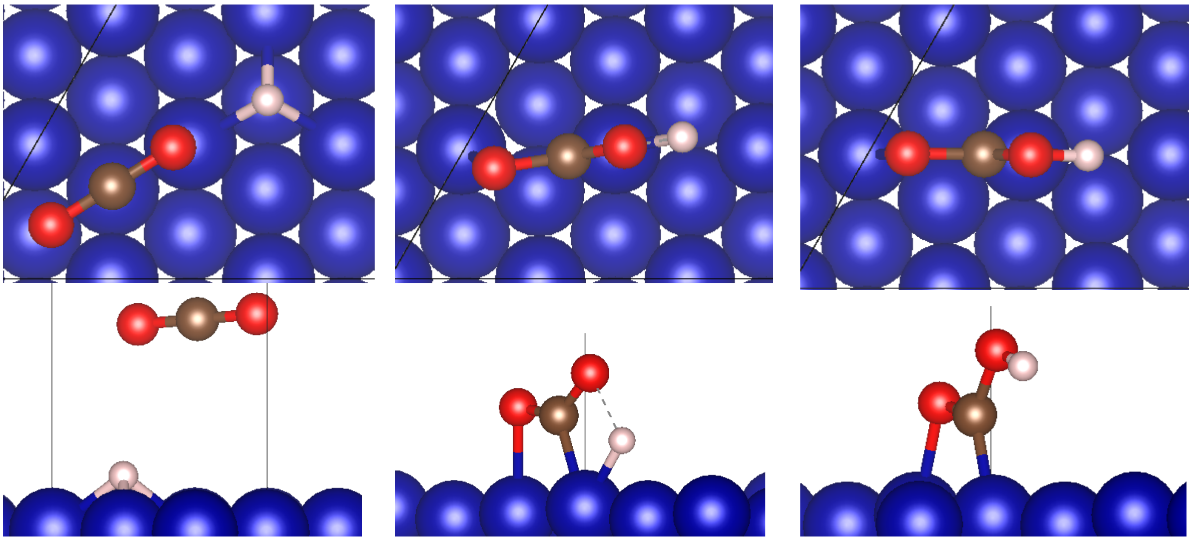

(d) $CO_2 + H^* \longrightarrow COOH^*$

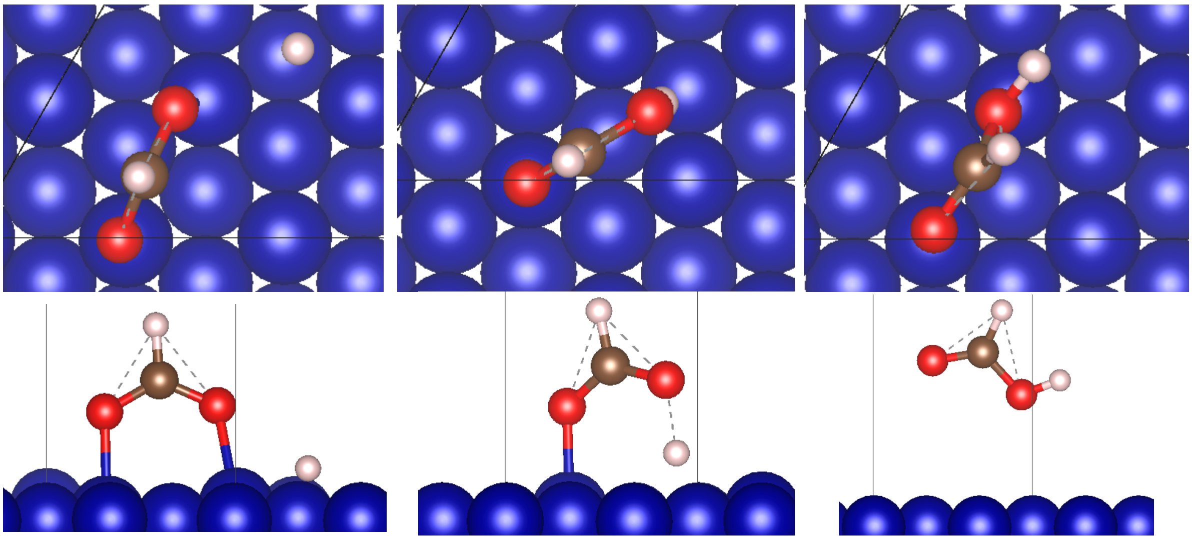

(e) $HCOO^* + H^* \longrightarrow HCOOH + 2^*$

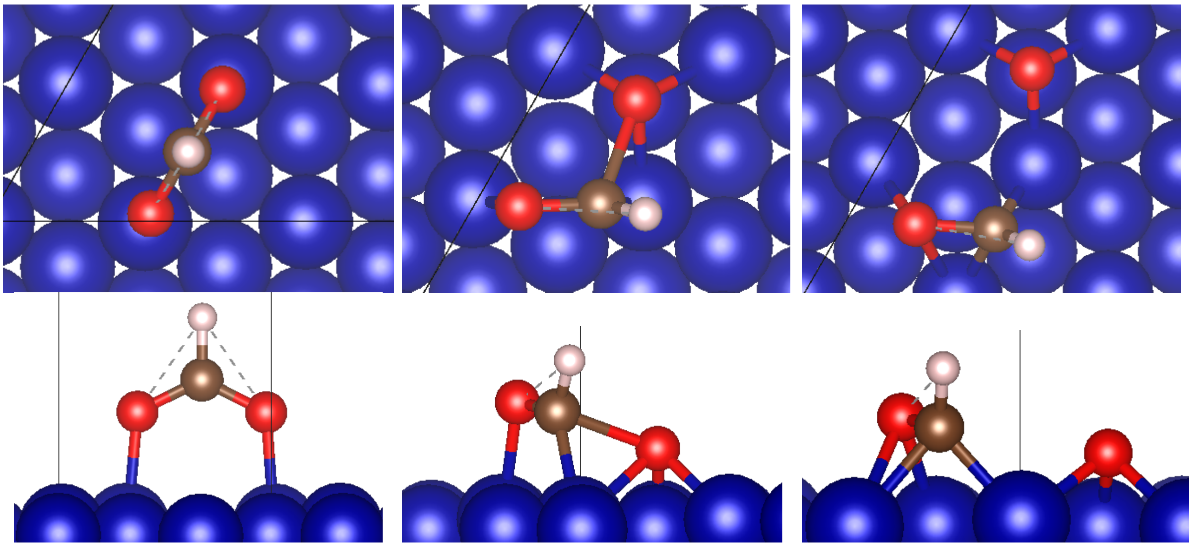

(f) $HCOO^* +^* \longrightarrow O^* + HCO^*$

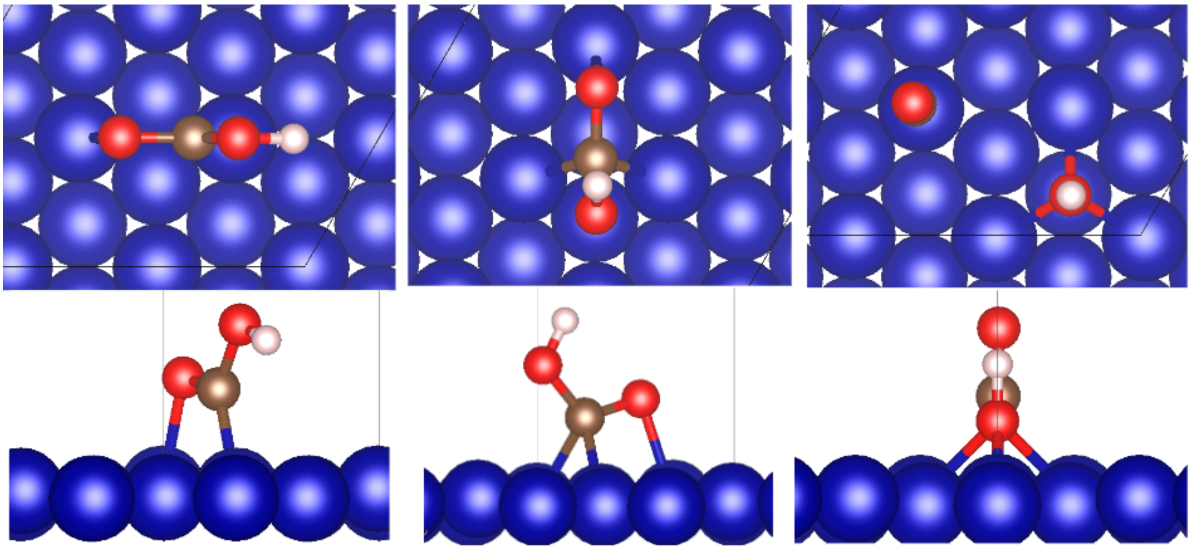

(g) $COOH^{*}+^{*} \longrightarrow CO^{*} + OH^{*}$

Iron Carbide Results

Table B.2: Cohesive energies calculated for all iron carbides studied with PBE, VdW-DF and SCAN-rVV10 functionals.

	Coehesive Energy (eV/atom)			
Functional	$\epsilon - Fe_3C$	$\eta - Fe_2C$	$\chi - Fe_5C_2$	$\theta - Fe_3C$
PBE	-5.69	-5.93	-5.79	-5.69
VdW-DF	-4.97	-5.22	-5.05	-4.95
SCAN	-5.54	-5.77	-5.65	-5.54

Table B.3: Formation energies (μ_C=-6.65 eV) calculated for all iron carbides studied with PBE, VdW-DF and SCAN-rVV10 functionals.

	Formation Energy (eV/atom)			
Functional	$\epsilon - Fe_3C$	$\eta - Fe_2C$	$\chi - Fe_5C_2$	$\theta - Fe_3C$
PBE	-0.60	-0.82	-0.70	-0.60
VdW-DF	-0.14	-0.20	-0.15	-0.12
SCAN	-0.77	-1.00	-0.88	-0.77

Table B.4: Surface energies of $\epsilon - Fe_3C$ surfaces for PBE, VdW-DF and SCAN-rVV10 functionals and atoms ratio Fe/C.

	Fe/C	PBE	DFT-PBE [92]	VdW-DF	SCAN-rVV10
$(001)_{0.0}{}^{*}$	3.00	2.93	1.58	2.65	3.35
$(011)_{0.0}{}^{*}$	3.00	3.06	2.05	2.73	3.35
$(101)_{0.0}{}^{*}$	3.00	2.32	1.95	2.10	2.54
$(001)_{0.0}{}^{\dagger}$	4.50	3.59		2.45	4.32
$(011)_{0.0}{}^{\dagger}$	3.25	3.00		2.49	3.32
$(101)_{0.0}{}^{\dagger}$	3.25	2.69		2.27	3.02

Table B.5: Surface energies of $\eta - Fe_2C$ surfaces for PBE, VdW-DF and SCAN-rVV10 functionals and atoms ratio Fe/C.

	Fe/C	PBE	VdW-DF	SCAN-rVV10	DFT-PBE [88]
$(001)_{0.0}{}^*$	2.00	2.87	2.60	3.07	3.048
$(011)_{0.0}{}^*$	2.00	3.22	2.84	3.74	2.404
$(101)_{0.0}{}^*$	2.00	2.81	2.53	3.03	3.084
$(110)_{0.0}{}^*$	2.00	3.07	2.76	3.07	2.439
$(100)_{0.0}{}^\ddagger$	2.00	2.53	2.27	2.65	2.925
$(001)_{0.0}{}^\dagger$	1.33	2.28	3.17	2.13	
$(011)_{0.0}{}^\dagger$	1.00	2.07	3.38	2.37	
$(101)_{0.0}{}^\dagger$	1.33	2.14	3.06	2.07	
$(110)_{0.0}{}^\dagger$	1.33	2.50	3.33	2.43	

Table B.6: Surface energies of $\chi - Fe_5C_2$ surfaces for PBE, VdW-DF and SCAN-rVV10 functionals and atoms ratio Fe/C.

	Fe/C	PBE	PBE [67][79]	VdW-DF	SCAN-rVV10
$(100)_{0.0}{}^*$	2.50	2.24	2.19	2.00	2.48
$(100)_{0.287}{}^*$	2.50	2.44	2.42	2.19	2.66
$(100)_{0.0}{}^\dagger$	3.00	2.95		2.18	
$(100)_{0.287}{}^\dagger$	3.50	3.66		2.30	
$(010)_{0.25}{}^\ddagger$	2.50	2.22	2.24	2.00	2.54
$(11\text{-}1)_{0.0}{}^\ddagger$	2.50	2.18	2.24	1.94	2.42
$(11\text{-}1)_{0.5}{}^\ddagger$	2.50	2.45	2.45	2.19	2.75
$(510)_{0.0}{}^\ddagger$	2.50	2.07	1.75	1.86	2.30

Table B.7: Surface energies of $\theta - Fe_3C$ symmetric and stoichiometric surfaces for PBE, VdW-DF and SCAN-rVV10 functionals and atoms ratio Fe/C.

	Fe/C	PBE	PBE [92]	VdW-DF	SCAN-rVV10	USPP GGA[95]
$(010)_{0.0}$	3.00	2.73	2.46	2.39	2.99	2.26
$(101)_{0.0}$	3.00	2.59	2.39	2.28	2.73	2.25
$(110)_{0.0}$	3.00	2.41	2.34	2.11	2.53	2.19
$(111)_{0.0}$	3.00	2.37	2.39	2.08	2.51	2.22
$(0\text{-}11)_{0.0}$	3.00	2.40	2.00	2.12	2.61	

---

[*] Surface asymmetric and stoichiometric to the bulk structure.

[†] Surface symmetric and non-stoichiometric to the bulk structure, calculated with μ_C= -7.56 eV.

[‡] Surface symmetric and stoichiometric to the bulk structure.